DEVELOPMENT OF SERS NANOPROBES FOR MULTIPLEXED AND MULTI-MODALITY MOLECULAR DIAGNOSIS OF CANCER

by

JAMES OTIENO NYAGILO

Presented to the Faculty of the Graduate School of
The University of Texas at Arlington in Partial Fulfillment
of the Requirements
for the Degree of

DOCTOR OF PHILOSOPHY IN BIOMEDICAL ENGINEERING

THE UNIVERSITY OF TEXAS AT ARLINGTON
DECEMBER 2012

Acknowledgements

A recently popularized African proverb says “It takes a whole village to raise a child”. I have learnt a lot as a graduate student and I am certain the time spent at UTA will be very valuable in shaping the rest of my career. I have only been able to make it this far because of the support and guidance of so many people. I will not be able to mention everyone here but to every single person who helped even in what they may have considered the smallest way, I am deeply grateful.

First and foremost, I acknowledge and thank my advisor Dr. Davè. Dr. Davè’s love for science particularly how science can practically change a person’s life drives the way he interacts and invests in his students. I thank him for taking a chance on me and giving me the opportunity to learn science in his lab. His work and life has been an inspiration to me. I would also like to thank my committee for their guidance during my graduate studies. I want to particularly thank Dr. Xiankai Sun without whose collaboration a lot of the work that is presented in this dissertation would not have been possible. Dr. Sun not only opened his laboratory but opened a whole resource network of post docs and graduate students who were specialized in areas I had little experience in. I am grateful to Dr. Khosrow Behbehani, Dr. Hanli Liu and Dr. George Alexandrakis whose doors have always been open. As lecturers and as committee members their advice was has been invaluable. I remember, for instance, during my first week in UTA I visited Dr. Behbahani with questions on how to plan my lectures and he took the time to help me devise a plan on how to succeed through the first semester. I also want to deeply thank Dr. Jean Gao and her student Shuo Li who were kind enough to share their expertise with us.

I am grateful for my fellow graduate students. I have to credit Nguyenvu Chu for introducing me to Raman spectroscopy. Nguyenvu’s most memorable advice to me was

“wear gloves!” I also have to mention Ming Xiao who is responsible for all the chemistry I learnt during the beginning of the project. Ming is the very personification of stubborn consistency. Her work ethic showed what it means to progressively work at an idea until you get a result. I am grateful to Sajal Chirvi, Kevin Huang for the numerous brain storming sessions we had. These and so many others: Keshav, Daniel, Miriam, Abhijit, Salim, Greg and Sukanya were not just colleagues but have become close friends. I am truly grateful for having met and interacted with them and all the friends that I have made at UTSW and at UTA. I hope to we continue to stay in touch.

My family has been a very strong support for me during this time. I want to thank my dad, my mum and sister Carol for first alerting me to the opportunity for Biomedical engineering at UTA. Without them and the unwavering support from Fred, Beatrice and Christine I would not have applied. They got me started and have been there throughout. Thank you.

July 30, 2012

Abstract

DEVELOPMENT OF SERS NANOPROBES FOR

MULTIPLEXED AND MULTI-MODALITY

MOLECULAR DIAGNOSIS

OF CANCER

James Otieno Nyagilo, PhD

The University of Texas at Arlington, 2012

Supervising Professor: Digant P. Davè

Importance of cancer diagnosis and staging through molecular biomarker detection is evident in the increasing number of molecular biomarkers being discovered that are associated with specific cancers types with their role in disease severity and progression being elucidated. Molecular imaging modalities capable of simultaneously detecting multiple molecular biomarkers combined with high resolution anatomical imaging techniques can potentially deliver a cancer diagnostic imaging platform with superior resolution and sensitivity. Nanotechnology, specifically in the form of functionalized metal nanoparticles exhibit unique chemical and electromagnetic properties that may be exploited to develop targeted multimodality contrast agents for combined molecular detection and structural imaging platforms.

The main objective this research was the development of nanoprobes that would enable sensitive and targeted multiplexed molecular detection of cancer biomarkers coupled with whole body anatomical imaging of tumors. The nanoprobes were composed of gold nanoparticle cores which enhanced Raman active molecules (Raman reporter) adsorbed on them by upto seven orders of magnitude through the process called surface

enhanced Raman scattering (SERS). Multiple Raman reporters are distinguishable in mixture due to the molecular specificity the Raman spectrum allowing for multiplex detection. SERS nanoprobes enabled multi-modality imaging by combining contrast for optical imaging and computed tomography (CT) in one probe. Targeted detection was achieved by conjugating high affinity ligands (antibody and peptides) to the nanoprobes.

A modular Raman instrument was designed and fabricated that could be integrated with a microscope or used as a stand-alone instrument for detection of SERS nanoprobes *in vitro* or in small animals respectively. Eleven colors of SERS nanoprobes with distinct Raman spectral signature were developed using a quasi-spherical gold nanoparticles (diameter 65.6±6.4 nm) which yielded the highest SERS signal from a size range of 16.7 – 114nm synthesized gold nanoparticles. A subset of these nanoprobes was selected for target molecular imaging (*in vitro* and *in vivo*). *In vitro* studies were conducted using glioblastoma astocytic (U87-MG) cells and prostate cancer cell lines (C4-2 and PC-3). SERS nanoprobes evaluated for target specific detection of cancer biomarkers displayed specificity. Cells labeled with targeted SERS nanoprobes recorded signal intensities up to one order of magnitude more than cells labeled with non-targeted SERS nanoprobes. Quantitative evaluation of four simultaneous detected SERS nanoprobes was demonstrated in U87-MG cells. *Longitudinal in vivo* studies were conducted in xenograft tumor model and an orthotropic tumor model to evaluate SERS nanoprobes for multimodality SERS/CT imaging. SERS nanoprobes displayed significant X-ray attenuation and were detectable subcutaneously and in excised tissue using SERS spectroscopy. Taken together, the results obtained suggest that SERS nanoprobes are versatile and robust contrast agents usable for multiplexed, multimodality molecular imaging of tumor.

Table of Contents

List of Illustrations

List of Tables

Chapter 1

Introduction

Motivation

In cancer research, molecular substances that indicate the presence of cancer in the body are referred to as cancer biomarkers[1]. Numerous biomarkers have been elucidated for diagnosis and prognosis of cancer including prostate specific antigen (PSA) for prostate cancer[2, 3], alpha-fetoprotein (AFP) for Hepatocellular cancer[4, 5], cancer antigen 125 (CA 125) for ovarian cancer[6] and cancer antigen 19-9 (CA 19 – 9) for pancreatic cancer [7]. Over 1261 proteins have different expression levels in human cancer tissue compared to normal tissue [8] and there is potential for increasing the number of cancer biomarkers significantly given the large number of proteins in the body that may act as indicators of biological state (over 10 000 in blood alone)[9]. A limitation of cancer biomarkers is that they do not detect all individuals with cancer because of the complex, progressive and heterogenic nature of cancer cells. In addition, presence of cancer is sometimes indicated when none is present because biomarkers are not unique to tumors[1]. Identification of an ensemble of biomarkers to enable clinical sensitivity and specificity in cancer diagnosis and therefore a modality with potential for simultaneous detection of multiple biomarkers is required. Combining such a modality with high resolution anatomical imaging techniques can have the added advantage of localization of tumors.

Compared to other imaging modalities, optical techniques have the potential to probe tissue morphology with higher resolution and functional status with higher sensitivity. In the past decade a number of optical modalities have been developed for cancer imaging, particularly for cancer screening and margin detection. Thus far, implementation of optical imaging for *in vivo* cancer imaging has so far met with mixed results. Optical techniques probe cancer related abnormalities that affect tissue morphology, molecular composition or functional status by implementing some form of spectroscopy, interferometry or microscopy. Modalities

such as light scattering spectroscopy [2-3], confocal microscopy [4-6], and OCT [7-11] provide information about changes in tissue microstructure. OCT and confocal microscopy generate depth resolved images whereas light scattering spectroscopy techniques measures the average morphology of cell nuclei but do not provide an image. Fluorescence [12-13] and Raman [14-17] spectroscopies can potentially detect changes in molecular composition of tissue due to tumor genesis. A drawback of using light for tissue imaging is the limited penetration of photons in tissue due to scattering and absorption. Despite higher resolution and sensitivity, optical techniques thus so far have not gained wide clinically acceptance for cancer imaging. Improvement of optical contrast and combining them with other imaging modality will significantly improve utility of optical techniques for diagnostic cancer imaging.

CT is a widely used imaging modality for various clinical diagnostic applications. Hard tissues have higher X-ray attenuations than various soft tissues whereas the contrast between soft tissues is inherently poor, which limits the sensitivity with which diagnosis of pathologies such as cancer can be made. Currently, iodine based compounds are used to enhance contrast of CT which have the limitations of short imaging window due to rapid clearance by kidneys and renal toxicity. Recognizing the weak endogenous optical contrast in cells and tissues, a major research focus area in the past decade has been the development of targeted exogenous agents to dramatically improve molecular and morphological contrast for cancer imaging. In this regard metal nanoparticles are very promising not only for optical imaging but also for established imaging such as ultrasound, CT and MR. Nanoparticle based CT contrast agents have been demonstrated for vascular imaging, which include, bare gold nanoparticles, polymer-coated gold nanoparticles, gadolinium-coated gold nanoparticles and polymer-coated Bi_2S_3.[28-35]. Molecular CT imaging of cancer using targeted AuNPs in cell culture has been demonstrated by Popovtzer *et. al.* [30]. X-ray absorption of gold nanoparticles is higher than iodinated compounds used as CT contrast agents. In addition, metal nanoparticles exhibit unique optical properties due to their size that is not exhibited by their bulk counterpart. For

example, Raman scattering of certain dyes in contact with nanoparticles can be enhanced by a factor 10^{14} to enable single molecule detection [18-21]. Toxicity is a critical issue that needs to taken into consideration for *in vivo* use of any type of nanoparticles. Gold nanoparticles are considered less cytotoxic compared to fluorescent dyes, quantum dots and carbon nanotubes. Gold provides a facile surface for bioconjugation using the well-established thiol chemistry. These advantages make gold nanoparticles a robust platform for developing functionalized contrast agent to be used for diagnostic molecular imaging applications.

SERS nanoprobes are comprised of metallic core nanoparticle encoded using Raman active molecules (Raman reporters) whose Raman spectrum provides the signal for the SERS nanoprobes. Specificity of the SERS nanoprobes to a target is achieved by conjugating a ligand onto the gold surface of the encoded nanoparticle. The gold nanoparticle core imparts the SERS nanoprobes with X-ray attenuation resulting in a dual SERS/CT contrast agent. Simultaneous detection of multiple analytes (multiplexing) results from the high spectral resolution the Raman signal typically composed of peaks with bandwidths as low as 1 nm [10] at full width and half maximum compared to bandwidths of 30 – 50 nm for quantum dots and ~ 150 nm for molecular fluorophores [11]. These narrow bandwidths minimize peak overlap in multiplex spectra allowing identification of individual SERS nanoprobes colors [12-17]. In literature, simultaneous detection of up to 6 DNA molecules in a micro-array format coated with silver film [13], identification of 5-10 SERS nanoprobes mixed together in solution [18-20] have been demonstrated. It is estimated that as many as 100 SERS nanoprobes may be theoretically detected in solution compared to 1-3 fluorophores and 3 – 10 quantum dots[21]. Thus the potential of multiplexing offered by the nanoprobes promises the capacity to simultaneously detect numerous pathological conditions with just one sample.

Objective of the Project

The main objective of the proposed research was the development of multiple-color SERS nanoprobes for cancer diagnosis. A SERS nanoprobe consist of a gold nanoparticle

core encoded with a Raman reporter and encapsulated using poly(ethylene) glycol. Targeted SERS nanoprobes were those nanoprobes to which high affinity targeting ligands were conjugated. The SERS nanoprobes were designed to serve as contrast agents for differentiating between cancerous lesions and normal tissue at a molecular level. The overall objective of the project was accomplished by following specific aims.

Aim 1: Construct and calibrate multiple wavelength modular Raman spectroscopy systems.

Aim 2: Synthesis and evaluation of nanoprobes

Aim 3: Validation of targeted nanoprobes in biological systems

Scope and Organization

This dissertation describes the development of multi color SERS nanoprobes with dual SERS and CT contrast and proof-of-principle demonstrations of their *in vitro* and *in vivo* cancer detection capacity. The dissertation includes descriptions of tools developed for measurement and analysis of SERS signal namely a modular Raman instrument and quantitative analysis algorithm respectively. A short description of each chapter appears *infra* (table 1.1).

Table 1-1 Scope and organization of the dissertation described chapter by chapter

Chapter	*Description*
Chapter 1	Cancer diagnosis is defined as the medical area of interest. The promise of earlier and more specific cancer diagnosis through multiplex multimodality platforms in explained and SERS nanoprobes are introduced as contrast agents that offer dual multiplex SERS and CT detection capacity
Chapter 2	SERS based nanoprobes are described beginning with a literature review of the current progress in development of SERS nanoprobes for imaging. A theoretical mechanism of SERS is explained and the modular Raman instrument designed for SERS detection is described
Chapter 3	The design and synthesis of the SERS nanoprobes is described. The description includes synthesis of the gold nanoparticle which acts as the SERS substrate, encoding and functionalization of the gold nanoparticle to prepare SERS nanoprobes and finally characterization of SERS nanoprobes.
Chapter 4	An algorithm (eigenspectra algorithm) designed identify and quantify of different colors of SERS nanoprobes in a multiplex signal is described.

Table 1-1—*Continued*

Chapter	*Description*
Chapter 5	Two *in vitro* demonstrations of targeted SERS nanoprobes detection in cancer cells are described. First prostate cancer cell lines are used to determine specific targeting by SERS nanoprobes. Quantitative attachment of SERS nanoprobes is then described in glioblastoma multiforme cell lines.
Chapter 6	*In vivo* studies are described that separately evaluate SERS nanoprobes for dual SERS/CT detection and for transdermal delivery. Evaluation of dual SERS/CT detection is described subcutaneously and using an orthotropic tumor model. Transdermal delivery of SERS nanoprobes is described in two studies using xenograft mouse models. In the first study uptake of SERS nanoprobes at tumors site is confirmed and in the second study accumulation and clearance of SERS nanoprobes is investigated.

Chapter 2

SERS Nanoprobes Applications, Theory And Instrumentation

SERS Nanoprobes in Biomedical Applications

Raman scattering is an inelastic process of light scattering by a molecule yielding a vibrational spectroscopic signal called Raman scattering signals [22]. Raman spectroscopy which involves measurement and analysis of Raman scattering signals is one of the most sensitive techniques for chemical analysis given the unique spectral fingerprint of every chemical compound. It is widely used as an analytical tool in pharmaceutical and chemical research. A major weakness of Raman spectroscopy is the poor efficiency of Raman scattering which has limited its use in bioimaging and biosensing. Raman cross-section (10^{-15} to 10^{-31} cm^2) are significantly smaller that fluorescence cross-sections (~10^{-16} cm^2) which have emerged as the dominant optical contrast agents for molecular imaging for a wide variety of *in vitro* applications.[23]. Efficiency of Raman scattering can however dramatically increase (enhancement factor - 10^6 to 10^{14}) when a molecule of interest is in close proximity to a nanosurface [22-28]. This enhancement is possible due to a phenomenon known as Surface Enhanced Raman Scattering (SERS)[23]. With such large enhancement of Raman scattering the use of SERS for biomolecular sensing is an attractive alternative to fluorescence. SERS provides three additional advantages. (i) The full width at half maximum (FWHM) of Raman peaks are about 2-3 nm making them 10-100 less that the FWHM peaks of quantum dots and fluorescent dyes. This property increases the multiplex capacity of Raman spectroscopy [17, 21, 23]. (ii) A single excitation source can be used for multiple analytes since the condition for enhancement requires the excitation source to be matched to the local surface Plasmon resonance condition of the nanoparticle and not the excitation wavelength of the analyte. (iii) No noticeable photobleaching has been observed with SERS nanoprobes increasing the potential for quantification with SERS nanoprobes [23].

Metal nanoparticles specifically gold nanoparticles have been the subject of research seeking to develop targeted exogenous agents that dramatically improve molecular and morphological contrast for cancer imaging. The use of nanobioconjugates in biomedical applications began with description of immunogold labeling by Faulk and Taylor[24, 25]. Electron rich metal nanoparticles have excellent reflective and scattering properties, plasmonic, magnetic, absorption and electromagnetic properties and therefore form contrast agents for multiple modalities. In addition nanoparticles, because of their amenability to immunosensing techniques have featured prominenty in cancer diagnosis/detection. Toxicity is a critical issue that needs to taken into consideration for *in vivo* use of any type of nanoparticles. Gold nanoparticles are considered less cytotoxic compared to fluorescent dyes, quantum dots and carbon nanotubes. These advantages make gold nanoparticles a robust platform for developing functionalized contrast agent to be used for diagnostic molecular imaging applications. In the past few years (2008) groups at Georgia Tech-Emory [26] and Stanford [27] have independently demonstrated the potential of *in vivo* cancer biomarker detection using SERS. These results along with work done by others [27] including results presented in this dissertation demonstrate the potential and promise of SERS for *in vivo* cancer imaging. To realize the potential of SERS for in vivo imaging will require a systematic study which involves synthesizing and testing multi-color SERS nanoprobes that not only give a large SERS signal but also have desirable biodistribution properties.

Mechanisms of Raman Scattering and SERS

Raman scattering

Energy of photons incident on small particles may be converted to some other form of energy (absorbed) or it may be radiated in directions different to the incident direction of the light (scattered). A vast majority of the scattered photons retain the same energy as the incident photons (Elastic or Rayleigh scattering) however, about 1 in 10^8 photons are scattered such that the energy of scattered photons are either gain or lose energy to the vibrational or

rotational modes of the molecule[23] (inelastic or Raman scattering). The wavelength of the Raman scattered light is therefore either blue shifted (anti-Stokes Raman scattering) or red shifted (Stokes Raman scattering) compared to the incident light wavelength (Fig. 2.1).

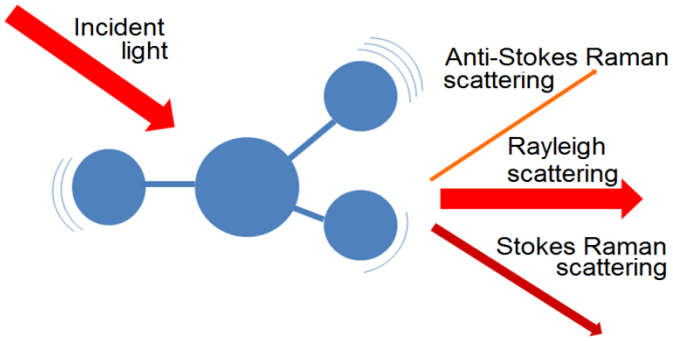

Figure 2-1 Illustration of light scattering by a molecule. Incident light with wavelength longer than the size of a molecule is either elastically or in-elastically scattered by the molecule. Elastically scattered light will have the same energy as the incident light and is called Rayleigh scattering. However the energy of in-elastically scattered light also called Raman scattered light is either more than energy of the incident light (anti-Stokes Raman scattering) or less (Stokes Raman scattering)

The energy of the Raman scattered light is usually represented using wavenumber [cm^{-1}] units called Raman shifts representing the shift in energy of the scattered light compared to the incident light. The positions of numerous sharp peaks of that compose a Raman spectrum provide molecular structural information while the intensity of the peaks depend on temperature, abundance of molecule and pH making Raman spectroscopy a versatile tool for probing molecular properties. A typical Raman scattering spectrum consists of narrow peaks shifted with respect to the incident excitation wavelength (Fig. 2.2).

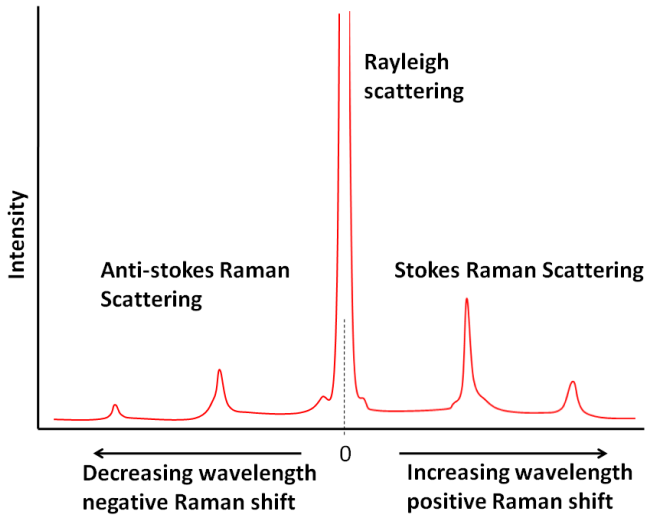

Figure 2-2 Typical Raman scattering spectrum. The x-axis designates the energy of scattered photons relative to the energy of the incident wavelength. Most of the scattered photons are scattered at the same wavenumber as the incident photon (Rayleigh scattering). Stokes and anti-Stokes Raman scattering are red and blue shifted respectively with respect to Rayleigh scattering. At room temperature, Stokes Raman scattering is more likely to occur than anti-Stokes Raman scattering and therefore has greater intensity than anti-Stokes Raman scattering.

The Raman scattering effect was first reported by C.V. Raman in 1928 [26] and independently confirmed in the same year by G. Landsberg and L. Mandelstam of Russia [27]. Raman focused sunlight using two lenses, an 18 cm diameter, 230 cm focal length telescope lens and a 5 cm focal length lens on to a scattering material usually a liquid purified several times through distillation in a vacuum. Two complementary optical filters were used in the set up. First a filter was used to block all incident light except blue–purple light. After excitation, the scattered blue-purple light was blocked by a filter that only allowed yellow-green light through. Green light observed after excitation [26] [27] meant that when a light beam interacts with a chemical compound a small fraction of that beam emerges from the compound at right angles to and different in wavelength from the incident beam. The potential for Raman scattering

spectroscopy in chemical analysis led to a rapid early development however this development fell into a silent period chiefly because of limitations in equipment that would allow for convenient measurement of the Raman spectrum. The invention of the laser, holographic filters and sensitive detectors has in the recent times led to a resurgence of Raman spectroscopy for a variety of biological applications.

When photons having energy $E_L = h\nu_L$ interact with a molecule, the molecule is excited from vibrational ground state υ_o to virtual state (Fig 2.3a). Most of the time the molecule relaxes and back to the same vibrational ground state emitting a photon with energy $E_s = E_L$. Raman scattering occurs when the molecule does not relax to the same vibrational ground state it was before excitation. Stokes Raman scattering describes the event when the molecule relaxes to a vibrational mode of higher energy than the vibrational ground state (Fig 2.3b). In this case energy of the scattered photon is less than the incident photon energy $E_s < E_L$ and has a red shifted wavelength and hence wavenumber. Alternatively, the molecule may already be in an excited vibrational mode when it interacts with the incident photon. This excitation is typically the result of thermal energy which can be related to temperature using Boltszman's constant (k_B) i.e. $E_T \approx k_B T$. If such a molecule relaxes to the vibrational ground state the scattered photon will have more energy than the incident photon $E_s > E_L$ resulting in anti-Stokes Raman scattering. Rayleigh and Raman scattering are quantum phenomena as illustrated using Jablonski diagrams (Fig. 2.3). However the quantum explanation of these phenomena does easily yield to generalization of Raman scattering to the SERS phenomenon. Therefore, classical mechanics is generally used to model the Raman effect.

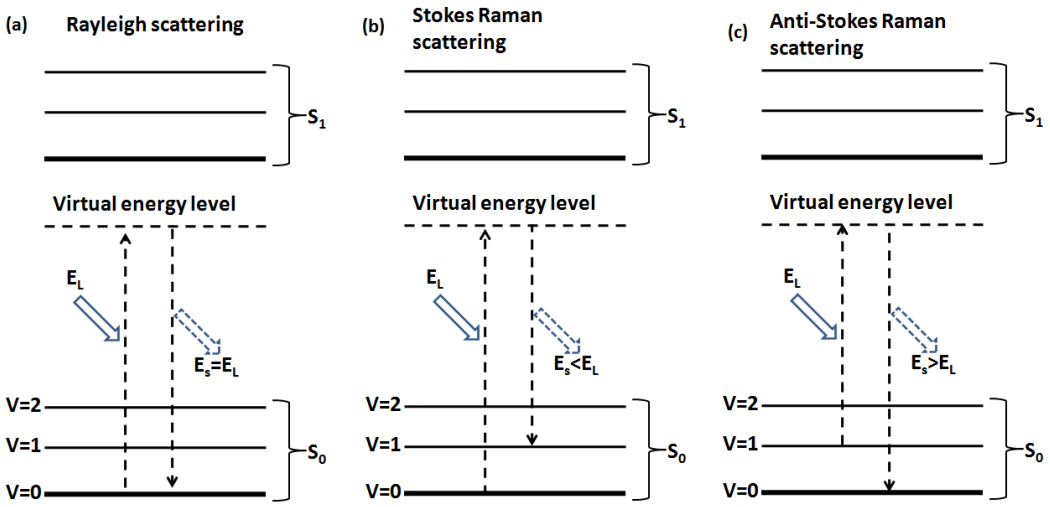

Figure 2-3 Simplified Jablonski diagrams (a)Rayleigh scattering, (b)Stokes Raman scattering and (c)anti-Stokes Raman scattering. Scattering is viewed as an instantaneous process in which molecules are excited to a virtual energy state by an incident photon. Upon relaxing the molecule radiates a photon of energy equal to incident photon (Rayleigh scattering), greater than incident photon (anti-Stokes Raman scattering) or less than incident photon (Stokes Raman scattering).

From the classical view point, light is an electromagnetic (EM) wave with an electric field $\vec{E}(\omega_L)$, oscillating with angular frequency ω_L in a direction perpendicular to the propagation of the wave. If monochromatic light is incident on a molecule, the incident electric field $\vec{E}(\omega_L)$ causes charge redistribution in the molecule inducing a dipole that oscillates with same angular frequency ω_L as the incident electric field. The dipole moment is given by

$$\vec{P}(\omega_L) = \alpha(\omega_L) \cdot \vec{E}(\omega_L) \quad \text{.....2.1}$$

Where linear polarizability $\alpha(\omega_L)$ of the molecule is a measure of how responsive the electrons in the molecule are to external pertubation. Polarizability may be considered linear since perturbations are small relative to the equilibrium of the molecule. The oscillating induced dipole in turn causes a pertubation in the electric field associated with it resulting in the emission

of radiation with the same energy as the incident EM wave. The differential power of the radiated wave is given by

$$\frac{dP_{rad}}{d\Omega}[W \cdot sr^{-1}] = \frac{{\omega_L}^4}{32\pi^2\epsilon_o c^3}\left|\vec{P}(\omega_L)\right|^2 sin^2\theta \quad \text{.....2.2}$$

Where $\epsilon_o = 8.854\ x\ 10^{-12} F \cdot m^{-1}$ is permittivity of a vacuum and c is the speed of light. The differential power is a function of direction $\Omega = (\theta, \phi)$ where $0 \leq \theta \leq \pi$ is the colatitude and $0 \leq \phi \leq 2\pi$ is the longitude using spherical co-ordinates. It also has a $sin^2\theta$ dependence which implies that the radiated wave has a two lobed pattern. Thus, Rayleigh scattering may be described as the process where an incident oscillating electric field induces dipole whose moment oscillates at the same frequency as the oscillating electric field. The oscillating dipole in turn radiates an EM wave at the frequency of its moment which is the frequency of the incident oscillating electric field[22].

However since incident electric field is modulated by vibrations of the molecule, polarizability for a single vibrational mode is also dependent on the physical vibrational co-ordinate. This implies that the induced dipole moment oscillates both at the frequency ω_L of the incident electric field and also at frequencies slightly greater than or less than ω_L [16]. Thus for a particular molecular vibrational mode of energy $\hbar\omega_v$ the dipolar frequency of the Stokes Raman scattering process is given by $\omega_R = \omega_L - \omega_v$. The Stokes Raman dipole moment for this particular mode is then given by

$$\vec{P}(\omega_R) = \alpha(\omega_L, \omega_v) \cdot \vec{E}(\omega_L) \quad \text{.....2.3}$$

The differential power of the radiated wave is given by

$$\frac{dP_{rad}}{d\Omega}[W \cdot sr^{-1}] = \frac{{\omega_L}^4}{32\pi^2\epsilon_o c^3}\left|\vec{P}(\omega_R)\right|^2 sin^2\theta \quad \text{.....2.4}$$

In the case of a molecule with multiple vibrational modes on which monochromatic light is incident, each of those modes emits radiation at a different wavelengths based on their particular vibrational mode energy and in the case of Stokes Raman scattering, the wavelengths are right shifted with respect to the Rayleigh scattering of the molecule. Hence

unlike Rayleigh scattering, Raman scattering reveals the chemical structure of the molecules being probed. For example the Raman scattering spectrum of acetaminophen (Fig. 2.4), a chemical commonly used in the manufacture of pain killers, reveals the chemical groups in acetaminophen can be deduced from the positions of their vibrational and rotational modes. The energies of these vibrational and rotational modes are represented using Raman shifts $[cm^{-1}]$ given by

$$\Delta k = \left(\frac{1}{\lambda_o} - \frac{1}{\lambda_v}\right) x10^{-7} \quad \text{.....2.5}$$

Where $\lambda_o[nm]$ is the wavelength of the incident radiation, and $\lambda_v[nm]$ is the wavelength of the Stokes Raman scattered vibrational mode

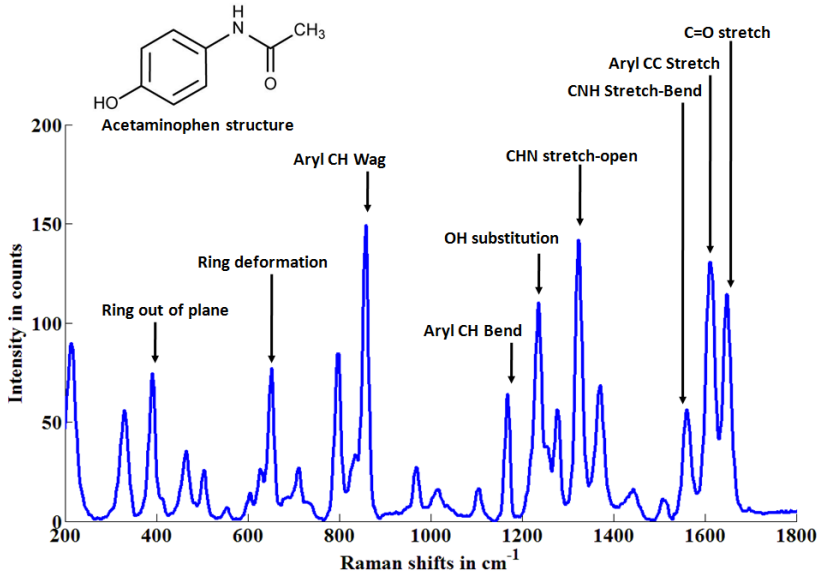

Figure 2-4 Molecular structure of Acetaminophen and the Raman spectrum of Acetaminophen measured using 785 nm incident laser light. Since each vibrational mode is Raman scattered at a slightly different position (Raman shift). The positions correspond to known vibrational modes that can be used to deduce the chemical structure of a compound.

Localized Surface Plasmon Resonance

Optical responses in metals such as gold and silver originate from the presence of free electrons (plasma) in the conduction bands of these metals. When EM radiation is incident on such a metal, the photons interact with these free-electron plasma forming photon-plasma modes called plasma-polaritons. For nanoparticles, these interaction occurs at the metal dielectric interface and are therefore referred to as surface plasma-polaritons (SPP), however since the SPP do not propagate they are refered to as localized surface plasma-polaritons (LSPP or simply LSP).

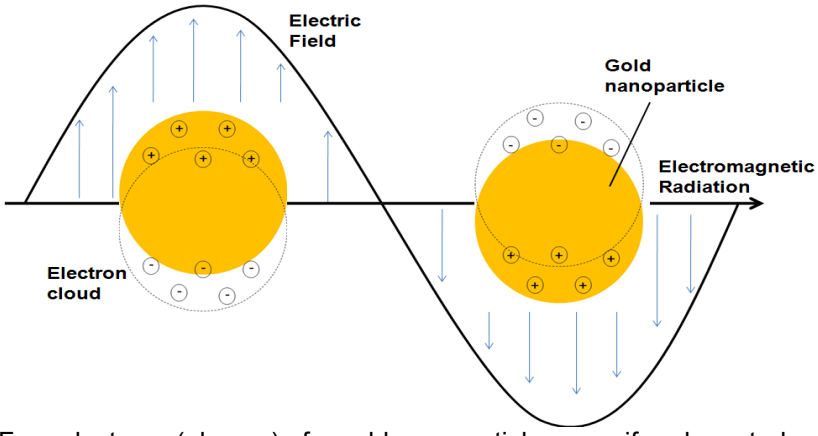

Figure 2-5 Free electrons (plasma) of a gold nanoparticle are uniformly perturbed by incident electromagnetic radiation whose wavelength is much greater than the diameter of the nanoparticles. The quasi-quantum particle formed from this interaction is called a localized surface Plasmon. When the incident radiation frequency the natural frequency of the free electrons a resonance condition called localized surface Plasmon resonance is fulfilled. Light at this frequency is scattered most efficiently

The optical response of the metals can be described using the relative dielectric function $\epsilon(\omega)$ which can be derived from Drude model and is given as

$$\epsilon(\omega) = \epsilon_b(\omega) - \epsilon_\infty \frac{{\omega_p}^2}{\omega^2 + i\gamma_o\omega^2} \quad \text{.....2.6}$$

Where ω is the angular frequency of the incident radiation,

$\epsilon_b(\omega)$ are inter-band transitions that co-exist with the electrons in the electron bands (i.e. bound electrons that are excited to higher energy levels),

ϵ_∞ is the constant background dielectric function of the positive ions in the crystal,

$\omega_p = \sqrt{\frac{ne^2}{m\epsilon_o\epsilon_\infty}}$ is natural oscillation frequency of the free-electron plasma also called the plasma frequency and corresponds to $\lambda_p = 2\pi c/\omega_p$.

m is mass of the electron in kilograms,

$n\ [m^{-3}]$ is the number of free electrons per unit volume and

e is the charge of the electron.

The dielectric function $\epsilon(\omega)$is a complex function and may be written in terms of its real and imaginary parts (for simplicity the contribution of the inter-band transitions is ignored).

$$Re(\epsilon(\omega)) = \epsilon_\infty \left(1 - \frac{{\omega_p}^2}{{\omega^2+\gamma_o}^2}\right) \quad \text{.....2.7}$$

And

$$Im(\epsilon(\omega)) = \frac{\epsilon_\infty {\omega_p}^2 \gamma_o}{\omega(\omega^2+\gamma_o)} \quad \text{.....2.8}$$

Since $\gamma_o \ll \omega$ the plasma frequency can be found by equating the real part of the dielectic function to zero. $\epsilon(\omega)$ may also be written in terms of the real and imaginary parts

$$\epsilon(\omega) = \epsilon_b(\omega) - \left\{Re\big(\epsilon(\omega)\big) + iIm(\epsilon(\omega))\right\} \quad \text{.....2.9}$$

Or

$$\epsilon(\omega) = \epsilon_b(\omega) - \left\{\epsilon_\infty \left(1 - \frac{{\omega_p}^2}{{\omega^2+\gamma_o}^2}\right) + i\frac{\epsilon_\infty {\omega_p}^2 \gamma_o}{\omega(\omega^2+\gamma_o)}\right\} \quad \text{.....2.10}$$

Considering a nanosphere in a dielectric medium of dielectic constant, ϵ_M, on which a electromagnetic wave with an electric field is incident. Since it is much smaller than the wavelength of light, the nanosphere can be considered to be in a uniform electric field , E_L .

The electric field inside the nanosphere is therefore constant and proportional to the incident field and can be given by

$$E_{in} = \frac{3\epsilon_M}{\epsilon(\omega)+2\epsilon_M} E_L \quad \text{.....2.11}$$

From this equation, if $\epsilon(\omega) \approx -2\epsilon_M$ then the intensity of E_{in} would be very large. This condition is met at the ω where $e\big(\epsilon(\omega)\big) \approx -2\epsilon_M$. Absorption which is characterized by the imaginary part of $\epsilon(\omega)$ is small (i.e $Im(\epsilon(\omega)) \approx 0$) and the inter-band transitions occur at higher energies than the plasma frequency. This is the resonance condition for a nanosphere also referred to as localized surface Plasmon resonance (LSPR).

For gold nanoparticles, however, presence of inter-band transitions at energies near the region where Plasmon resonances are expected increases $Re\big(\epsilon(\omega)\big)$ in that region and shifts the resonances to longer wavelength positions (fig 2.3a). In addition, optical absorption in region $\lambda < 600$nm is very high. In Figure 2.6 the optical response of 60 nm gold nanospheres characterized by extinction, scattering and absorption coefficients is plotted against wavelength. These optical characteristics are modeled based on Mie scattering for gold nanoparticles in air (A) and water (B). The extinction coefficient which is typically used to determine the position of the LSPR is derived from the absorbance and scattering characteristics of the nanoparticle. Scattering and absorbance characteristics are both wavelength dependent however they do not follow the exact same plot. In gold nanosphere the scattering coefficient peaks at a longer wavelength than the absorbance coefficient. Scattering is related to Ein and therefore while absorbance dampens the energy in the Plasmon. In addition, the effect of dielectric constant of the environment is seen in the increase and red-shifting of the peaks for all the plots for nanospheres in water compared to to nanospheres in air.

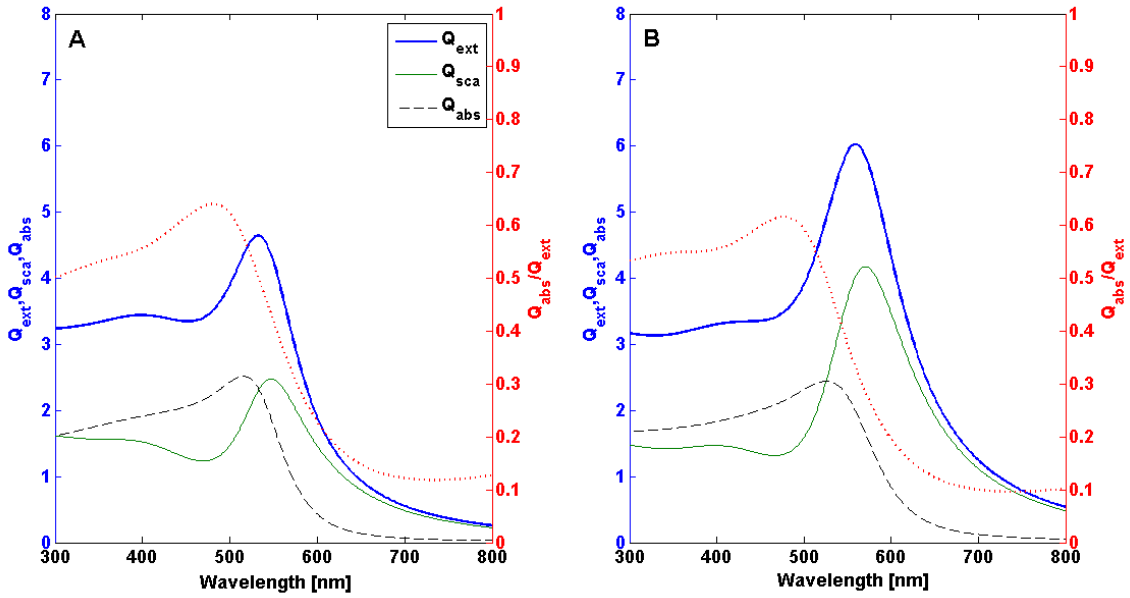

Figure 2-6 Optical properties of 60 nm gold nanoparticle in (A) air and (B) water. The extinction coefficient Q_{ext} (blue line) combines the scattering properties of the gold nanoparticles represented by the scattering coefficient Q_{sca} (green line) and the absorption coefficient Q_{abs}. The resonance condition can be seen to be wavelength dependent. In addition a change in dielectric constant results in a change in the LSPR position

Surface Enhanced Raman Scattering

SERS effect results from two mechanisms: an electromagnetic mechanism and a chemical mechanism[28, 29]. Chemical enhancement (CE) mechanism is thought to occur through charge transfer mechanism that occurs when the electrons of the nanoparticle interact with the adsorbed molecule resulting in an increase in the Raman cross-sectional area of the molecule[21, 22, 30]. Although CE mechanism it thought to account of enhancement of 2 orders of magnitude, the enhancement may actually vary from substrate to substrate[31]. The electromagnetic (EM) enhancement has been more thoroughly studied and more clearly explained. In this mechanism, enhancement is attributed to dual interactions of the LSPR field with the incident EM field and Raman scattering field resulting in four orders of magnitude

enhancement [22]. In this dissertation, the EM enhancement was used as a tool to intuitively understand SERS and to design the nanoparticle cores of the nanoprobes.

SERS enhancement occurs as a result of two simultaneously occurring interactions of whose actors include the incident electric field E_L, the electric field induced in the nanosphere E_{PM}, and the electric field induced around the molecular analyte through the Raman scattering process E_v. When an EM wave is incident on a nanosphere, the incident electric field E_L induces polarization in the nanosphere. The polarization is equivalent to the surface charge and can be considered as a point dipole about the centre of the sphere with dipole moment P_M given by $P_M = \propto_s E_L$. The induced dipole moment of the nanosphere in turn creates an electric field around the sphere named E_{PM}.

The expression of $\propto_s$ may be found using the equation for E_{in} and from Maxwells equations and takes into the account geometric values of the nanosphere. E_{PM} is added to the incident electric field E_L so that the total electric field around the nanosphere is given as

$$E_{out} = E_L + E_{PM} \quad \text{.....2.12}$$

E_{out} , which is much larger than E_L especially at the resonance, interacts with a molecular analyte adsorbed on the nanosphere inducing a Raman dipole moment $P_R = \propto_R E_L$ (refer eq. 2.1). The magnitude of this dipole moment is therefore enhanced by a factor equal to $\frac{|E_{out}(\omega_L)|}{|E_L|}$. The resulting energy from this process is proportional to $|P_R|^2$ and therefore is enhanced by $\frac{|E_{out}(\omega_L)|^2}{|E_L|^2}$. This process is the *local field intensity enhancement*. The energy produced in the local field intensity enhancement is not radiated to free space but instead simultaneously couples with the LSPR field of the nanosphere. This interaction is called *radiation enhancement* and results in the energy being enhanced by a factor $\frac{|E_{out}(\omega_R)|^2}{|E_L|^2}$. Assuming shift is small, $\omega_L \approx \omega_R$, the $|E|^4$ enhancement for EM mechanism commonly quoted in literature is obtained.

$$SERS\ EF \approx \frac{|E_{out}(\omega_L)|^2}{|E_L|^2} \cdot \frac{|E_{out}(\omega_R)|^2}{|E_L|^2} \approx \frac{|E_{out}(\omega_L)|^4}{|E_L|^4} \quad \text{.....2.13}$$

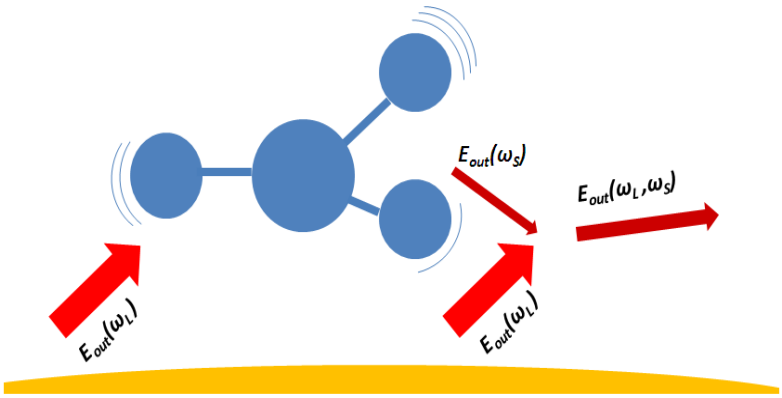

Figure 2-7 Electromagnetic mechanism of SERS of a molecule adsorbed on the surface of a gold nanoparticle. Enhancement occurs through two processes. The incident electric field is couple with and is enhanced by the local field that is due to the oscillating Plasmon. Therefore the molecule experiences an enhanced electric field. The Raman scattered light is therefore also enhanced. The electric field component of this light interacts again with the local field and is further enhanced

Instrumentation

Introduction

Raman spectroscopy instrumentation may be used to measure the SERS signal. The basic components of the Raman system include the excitation laser, optics to direct laser to the sample and collect scattering from the SERS signal and a spectrometer/detector to measure record the spectrum. Specific considerations to be made in the design of a Raman system to be used for SERS measurement for biological application include the choice of excitation laser wavelength as well as the focusing optic. The laser wavelength is important because (1) the dielectric function of the nanoparticle, which is a function of excitation wavelength, affects the resonance of the nanoparticle and therefore the intensity of the SERS signal. It is important to match the laser wavelength to the wavelength peak of scattering while avoiding absorption. (2) Light-tissue interaction is also wavelength dependent and therefore merits consideration. Specifically, tissue will heavily auto fluoresce at visible light wavelengths therefore near infra-red

wavelength are preferred for biological applications. A Raman modular instrument was designed and fabricated that would probe both in vitro and in vivo samples. Modular construction could be used as a standalone instrument for measurements involving small animals or integrated into a microscope for interrogating in vitro samples. Integration with a microscope would also allow for fluorescence microscopy confirmatory measurements.

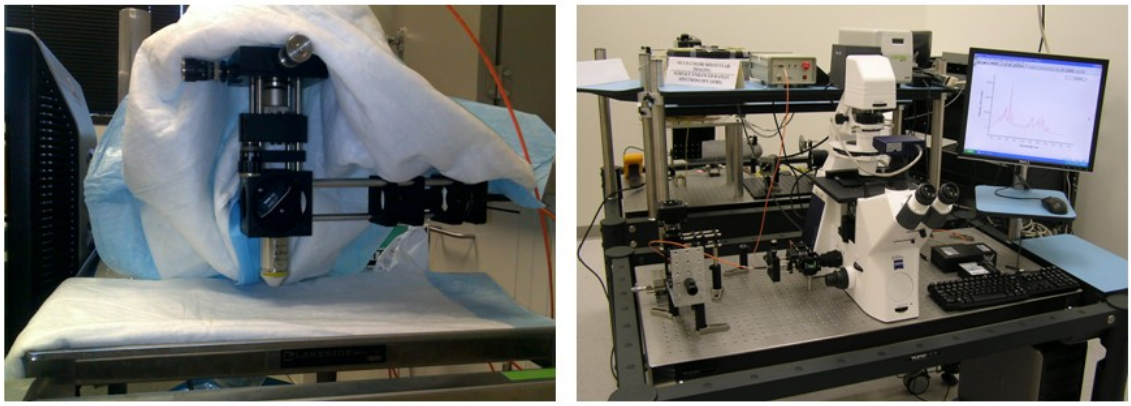

Figure 2-8 Modular Raman instrument used as a stand along instrument (left) or incorporated into a microscope (right). Mounting the cells on a microscope allows for dual DIC or Fluorescence imaging with Raman spectroscopy which is useful for in vitro studies. For *in vivo* studies the module can be mounted as a stand alone instrument allowing for direct measurement of Raman spectrum from a small animal placed underneath the module

Optical Setup of Raman Modular Instrument

Modular Raman construction was accomplished using a cage system. The optical setup (Fig 2.9) allows the instrument to operate in reflectance geometry. Laser light from the source is transmitted to the module using a multimode fiber (step index multimode fiber of core diameter 600 µm, 0.39 NA, transmittance >99% in the visible region). The light exiting the multimode fiber is transmitted through a neutral density filter (Thorlabs, 0.5) and a collimating lens before it is reflected by a dichroic onto an objective lens. The objective lens plays the dual role of focusing the laser excitation on to the sample as well as collecting the back scattered light. The back scattered light comprises of Rayleigh scattered light as well as Stokes and anti-Stokes Raman scattered light. The dichroic and an edge filter are used to filter out most of the

Rayleigh scattered light and the anti-Stokes Raman scattered light while they transmit Stokes Raman scattering which is coupled in to a second multimode fiber. The multimode fiber transmits the light to a high resolution spectrometer for analysis.

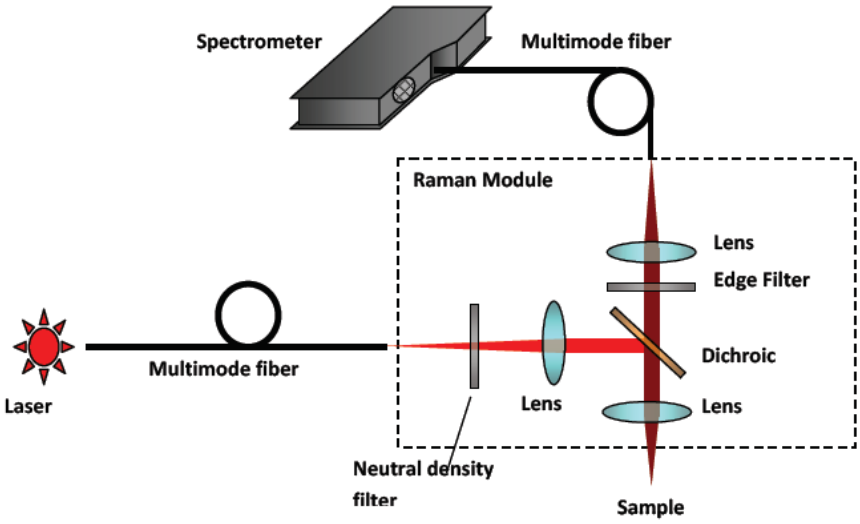

Figure 2-9 Optical setup Raman modular instrument

Throughput

Throughput of the system was determined as a measure of the transmittance of the collected light to the detector. A tungsten-halogen light source (200 nm – 1100 nm) was placed at the sample position and its light was collected by the modular system and using a broad band spectrometer (USB4000, Ocean optics) with spectral range from 200 nm to 900 nm. The obtained spectra are then compared to spectrum obtained the source is connected directly to the spectrometer.

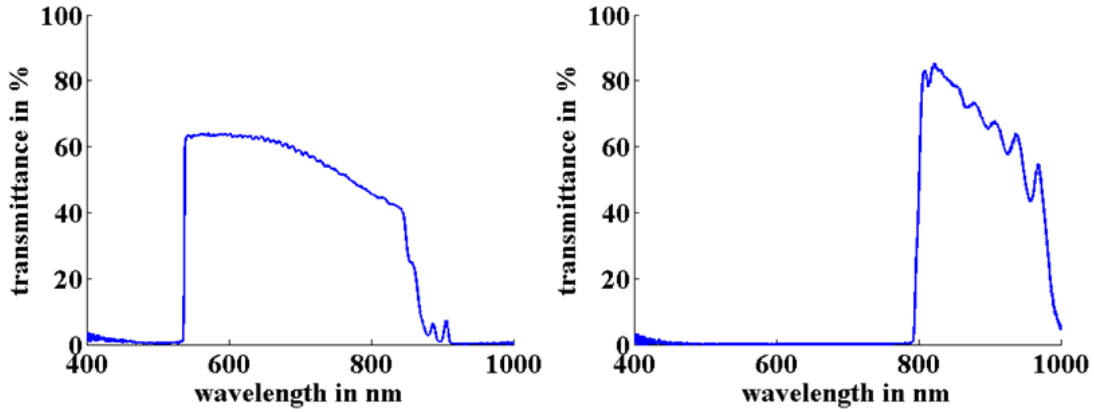

Figure 2-10 Throughput as a percentage of the source light measured for each wavelength for the (A) 532 nm system and (B) 785 nm system. The modules were designed to measure Stokes Raman shift. Therefore the spectrum of light measured needs to be of longer wavelength than the incident laser. Using the dichroic and edge filters the light from Rayleigh scattering is minimized and antistokes Raman is cut off

Spectral Callibration

The system was calibrated by measuring the Raman spectrum of Acetaminophen, a commonly used ingredient in pain relieving/fever reducing medicine whose spectrum has been completely analyzed in literature. The measured spectrum 785 nm and 70 mW is compared with Stokes Raman spectrum of acetaminophen obtained from RRUFF™ Project database. The obtained spectrum of acetaminophen spectra from the database is quoted to be measured at 780 nm using Thermo Almega XR at 600mW (Fig. 2.11). Similarly spectral accuracy of the 532 nm system is determined by comparing the Acetaminophen spectrum downloaded from the RRUFF™ Project database measured at 532 nm excitation using Thermo Almega XR 532nm at 150mW with the acetaminophen spectrum obtained using the 532 nm module (Fig. 2.12).

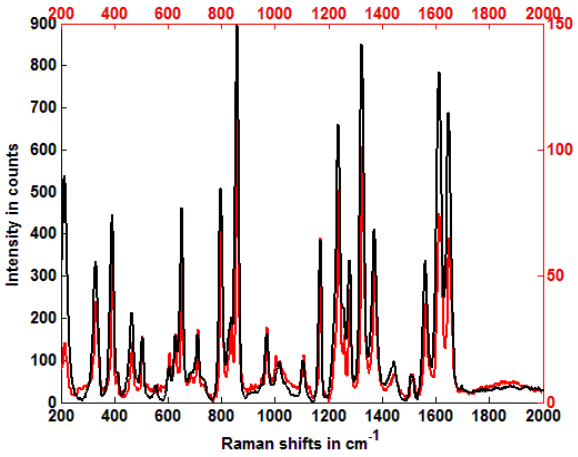

Figure 2-11 Comparison of Raman spectra of Acetaminophen measured using the 785 nm modular system and data obtained from RRUFF™ project database. The RRUFF™ project database is a database created at the University of Arizona Geology department to provide data for identification of mineral samples. The peaks of the measured sample compared with the peaks of the sample obtained from the RRUFF™ project database indicating that the spectrometer is well calibrated

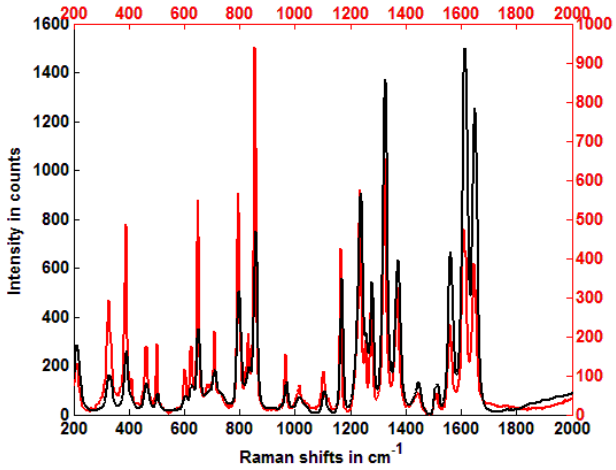

Figure 2-12 Comparison of Raman spectra of Acetaminophen measured using the 532 nm modular system and data obtained from RRUFF™ project database. The peaks of the measured sample compared with the peaks of the sample obtained from the RRUFF™ project database indicating that the spectrometer is well calibrated.

Signal to Noise Ratio (SNR)

SNR of the system was evaluated for the 1002.02 cm^{-1} vibrational mode of a polystyrene standard (40 x 40 x 2 mm) for different output power and integration time. The signal intensity was measured as the intensity value of the specified peak as shown in figure 2.8. Noise was obtained by determination of the deviations of the raw spectrum values relative to the mean intensity values obtained from the smooth spectrum at each point. The signal to noise ratio was then determined using the formula

$$SNR = \frac{Signal}{Noise_{RMS}} \quad \text{.....2.14}$$

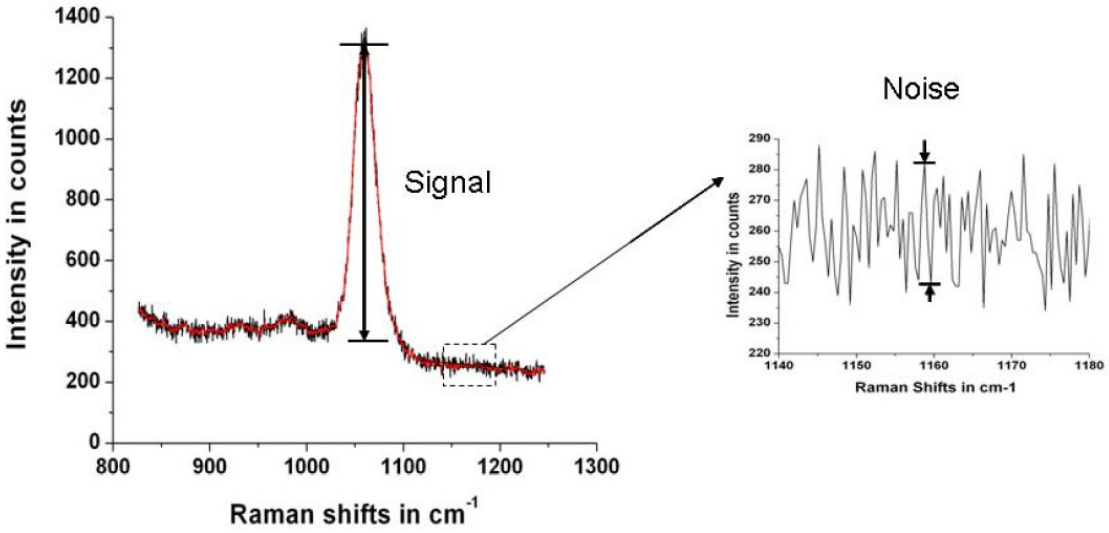

Figure 2-13 Raman spectrum of the 1030 cm^{-1} transitional mode of methanol illustrating signal and noise measurements. The noise level is limited by the inherent noise in the detector. Signal to noise ratio was measured to minimize as much as possible the noise is the system to that limiting value.

Table 2-1 Signal to noise ratio of the Raman modular system

Experiment Value	
Signal (counts)	1090.07±6.1
$Noise_{RMS}$ (counts)	9.11±0.8
S/N	120.1±10
Calculated Value	
Signal (e^-) using ADC conversion	1473.77±8.3
$Noise_{RMS}$ (e^-)	12.77
S/N	115.42±0.6

Summary

SERS nanoprobes are described as contrast agents for biomedical applications. SERS nanoprobes combine Raman spectroscopy and nanotechnology to produce a contrast agent that can be used for both Raman spectroscopy and CT. The narrow and distinct spectra of Raman scattering signals of molecules act as molecular fingerprints that are detectable in a mixture. Simulateneous detection of multiple SERS nanoprobes is therefore possible in solution and is one of the chief advantages for SERs nanoprobes. A Raman modular instrument for interrogation of in vitro samples and small animal measurements was designed and constructed. The instrument was found to be spectrally accurate and have signal to noise ratio comparable to commercial instruments.

Chapter 3

Synthesis and Characterization Of SERS Nanoprobes

Design of SERS based nanoprobes

Designs of SERS based nanoprobes may be categorized into two distinct groups: nanoprobes designed for label free or direct detection of analytes and encoded nanoprobes [21, 32]. Direct detection is the most common application of SERS and is typically carried out by mixing plasmonic nanoparticle, usually gold or silver, colloidal solutions with small volumes of analyte [12, 21, 33, 34]. The spectrum of the analyte is detected as it absorbs onto the metal nanoparticle. This method has been used in numerous applications including detection and characterization of RNA and DNA molecules[13], small proteins[35, 36], kinetic studies of single enzymes[37] and drug interactions with specific receptors[38]. However, because of the inherent complexity biological fluids, a separation step is usually required in direct sensing applications making it difficult to probe living systems or to obtain real time results[33]. In addition either aggregated or large amounts of single plasmonic nanoparticles are required within a probe area for high quality measurement[12]. SERS nanoprobes comprising plasmonic nanoparticles cores coded with organic Raman active molecules address this limitation[12, 17, 21, 33, 34, 39-42]. The Raman active molecules called Raman reporters lend the SERS nanoprobes characteristic signatures that are detectable in solution. This basic design of SERS nanoprobes was introduced by Rohr et al [41, 43-46]. The design employed here combined traditional design of encoded nanoprobes with directional conjugation of targeting ligand[47] (Fig 3.1). The large size of SERS nanoprobes (20 to 100nm) owing to the plasmonic core compared to other labeling agents including enzymes, molecular fluorophores and quantum dots[21] was advantageous in providing a large surface area for conjugation of both reporter and ligand and allowed greater accessibility to the ligand by target molecules[12, 33].

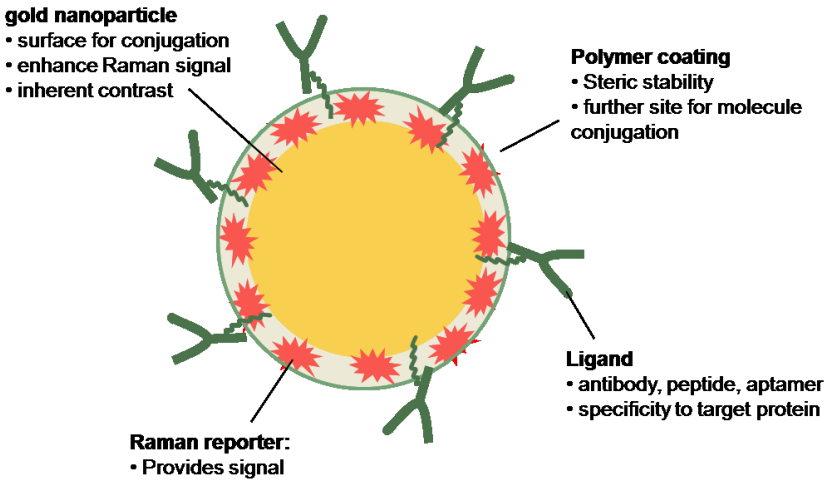

Figure 3-1 Schematic design diagram of a single SERS nanoprobe showing its layered compositional makeup. Single solid core gold nanoparticles are layered with Raman reporter, polyethylene glycol, and target specific ligands. Adsorbed Raman reporter on the gold nanoparticle surface provides a unique SERS signal that is dye specific. Using different Raman reporters yields nanoprobes of different spectral signatures (colors) that are used for multiplexing. PEG encapsulation of the gold nanoparticle provides steric stabilization and biocompatibility for *in-vivo* applications. SERS probes are decorated with target specific ligands that either are attached to the PEG layer or linked directly to the gold nanoparticle surface.

Synthesis of SERS nanoprobes involved three stages (Fig 3.2). First different sizes of quasi-spherical gold nanoparticles ranging from 16 – 120 nm were synthesized and evaluated for size and monodispersity using transmission electron microscopy (TEM) and dynamic light scattering (DLS). Evaluation of the relation of nanoparticle size with SERS enhancement factor identified 60nm gold nanoparticles as optimal for largest enhancement factors. Using 60 nm gold colloid solutions, 14 different SERS nanoprobes each coded with a different Raman reporter and referred to as colors of SERS nanoprobes were synthesized. 11 colors of SERS nanoprobes gave distinct signals and 5 of the SERS nanoprobe colors were found to have high enough intensity to be used in biomedical setting.

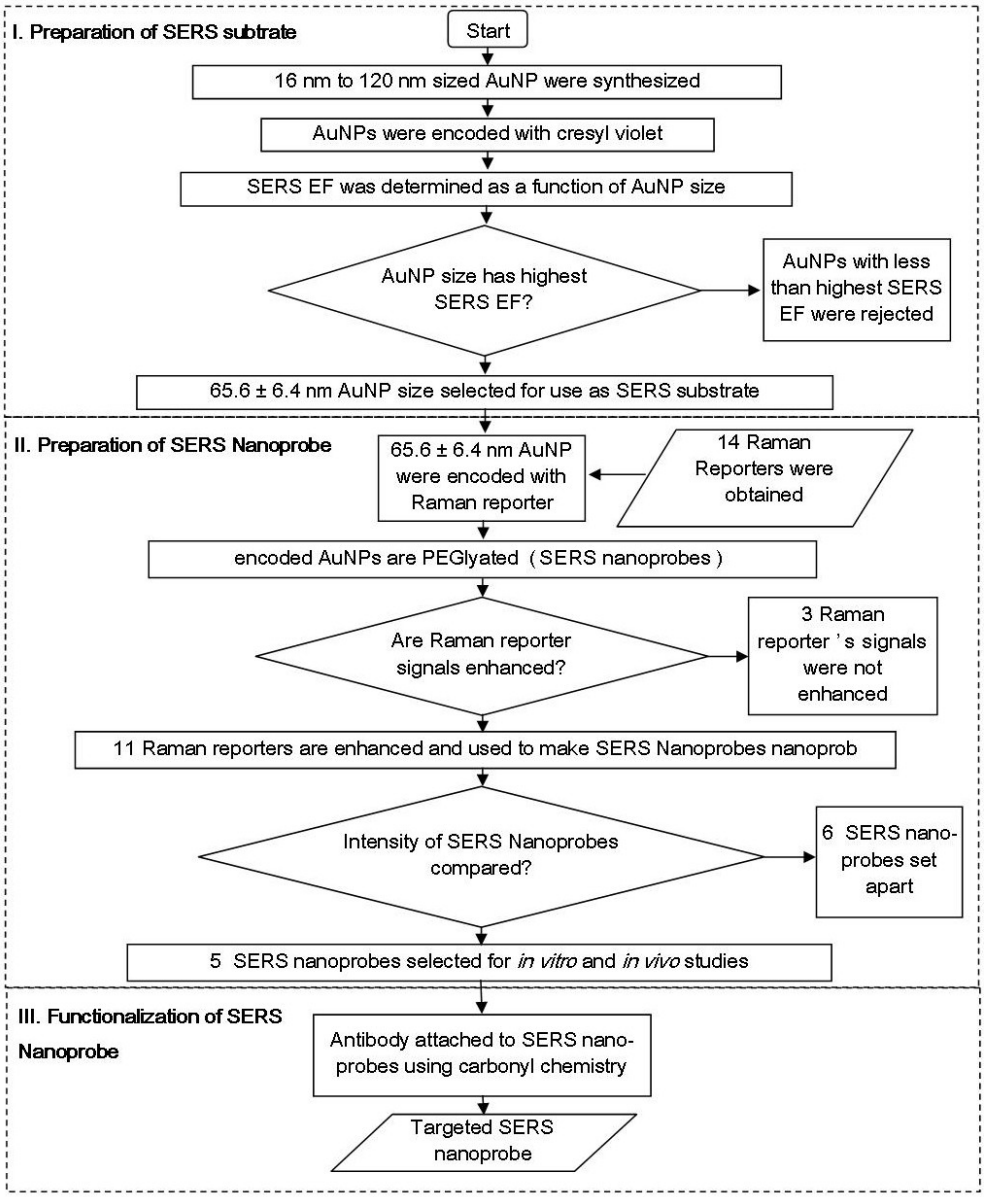

Figure 3-2 Flow chart summarizing the process of SERS nanoparticle synthesis

Preparation of SERS substrate

Selection of the size of gold nanoparticle to use as a SERS substrates provided a unique challenge. Whereas the size of gold nanoparticles that "supports the strongest Plasmon resonances and therefore the largest enhancement" is the ideal size for SERS substrate [22] the size of the gold nanoparticles is equally an important factor to consider in *in vitro* and *in vivo*

applications. Generally, smaller sizes of gold nanoparticles are considered to approach the size of various protein complexes allowing for more sensitive detection of protein expressions *in vitro*. *In vivo*, pharmacokinetic studies show that smaller nanoparticles, with certain constrains such as surface coating and charge, generally have longer half-lives in the blood stream which increases the probability of active targeting. However smaller sized of gold nanoparticles usually have smaller SERS EF. The goal for this section was to (1) determine the effect of nanoparticle size on the SERS enhancement and (2) identify the size of gold nanoparticle that resulted in the best SERS substrate.

Gold nanoparticles were prepared using two methods. Smaller gold nanoparticles (16 – 65 nm) were prepared by citrate reduction of gold ions[48, 49] and found to be monodispersed. However, above 65 nm the nanoparticles formed vary widely in size and shape. A seed growth method was therefore employed to synthesize larger (80 – 120 nm) gold nanoparticles[50]. Using these two method 6 sizes of gold nanoparticles ranging from 16 – 120 nm were synthesized.

Evaluation of the gold nanoparticles as SERS substrates was accomplished by determining SERS enhancement factor (SERS EF) for each size of gold nanoparticle. SERS EFs were determined for gold nanoparticle encoded with cresyl violet and coated with methyl capped thiolated polyethylene glycol (mPEG-SH) (Fig 3.3). The choice of this encoding and encapsulation allowed for generalization of the SERS EFs to SERS nanoprobes preparation. SERS EFs were determined to range from 5 – 7 orders of magnitude with 65.6 nm gold nanoparticles giving the largest SERS EFs.

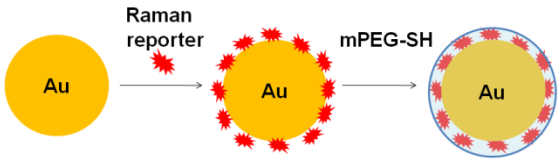

Figure 3-3 Schematic diagram showing stepwise preparation of SERS nanoprobes. Raman reporter is first encoded on single gold nanoparticles followed by PEGlyation

Method

To synthesize gold nanoparticles with size of about 65 nm, 500µl of 25 mM chloroauric acid ($HAuCl_{4(aq)}$) was added to 50 ml of boiling and stirring pure water in a redux setup. 500 µl of 1% (w/v) of sodium tricitrate ($Na_3C_6H_5O_7.2H_2O_{(aq)}$) was then immediately added. Within the first minute the color of the solution changed from pale yellow to blue black. After about 1.5 min the color gradually changed again from the blue black to a wine red color. The reaction was allowed to continue for 15 min before the nanoparticles were cooled at room temperature for at least 20 min. Different sizes of gold nanoparticles were synthesized by controlling the amount of sodium citrate solution added. Preparation gold nanoparticles with sizes of about 16nm, 40 nm and 65 nm was accomplished by adding 1.75ml, 700µl and 500µl sodium citrate solutions respectively while the concentration of chloroauric solution was maintained. Purification was done by centrifugation at 4000g for 10 min. Larger gold nanoparticles were synthesized by adding 16 nm gold nanoparticles (seed) synthesized by citrate reduction to a solution containing 2-mercatosuccinic acid (MSA) and chloroauric acid at fixed molar ration and under stirring. The size of gold nanoparticle was controlled by the amount of seed nanoparticles was added. A color change from pink to purple was observed and reflected the growth of gold nanoparticles.

Gold nanoparticles prepared were then encoded and peglyated before evaluation for SERS EF. Encoding of the gold nanoparticles required two processes. First the optimal concentration of the Raman reporter was determined then the determined optimal concentration was used to encode the SERs nanoprobes. The optimal concentration of Raman reporter was the concentration at which the maximum amount of Raman reporter was adsorbed onto the gold nanoparticle without causing aggregation and was determined through an iterative process (Fig 3.4). Gold nanoparticles (1ml) were placed in a clean culture tube under stirring at 700 rpm using a magnetic stir bar. Freshly prepared cresyl violet (10 µl and 5 µM) was added at 1 min intervals to the gold nanoparticle solution until a color change is observed. The color change was indicative of the onset of aggregation. The value of the cumulative volume *V* at which the

color change was observed was noted. New batch of cresyl violet (concentration C = 0.05*V* μM) would then be prepared and used to encode SERS nanoprobes. Encoding was done by adding 100 μl of the cresyl violet dropwise under rapid mixing followed by a 15 min period to allow for the reaction to occur. After this 200 μl of 10μM mPEG-SH (5KDa) was added and the solution left to stir for 30 min.

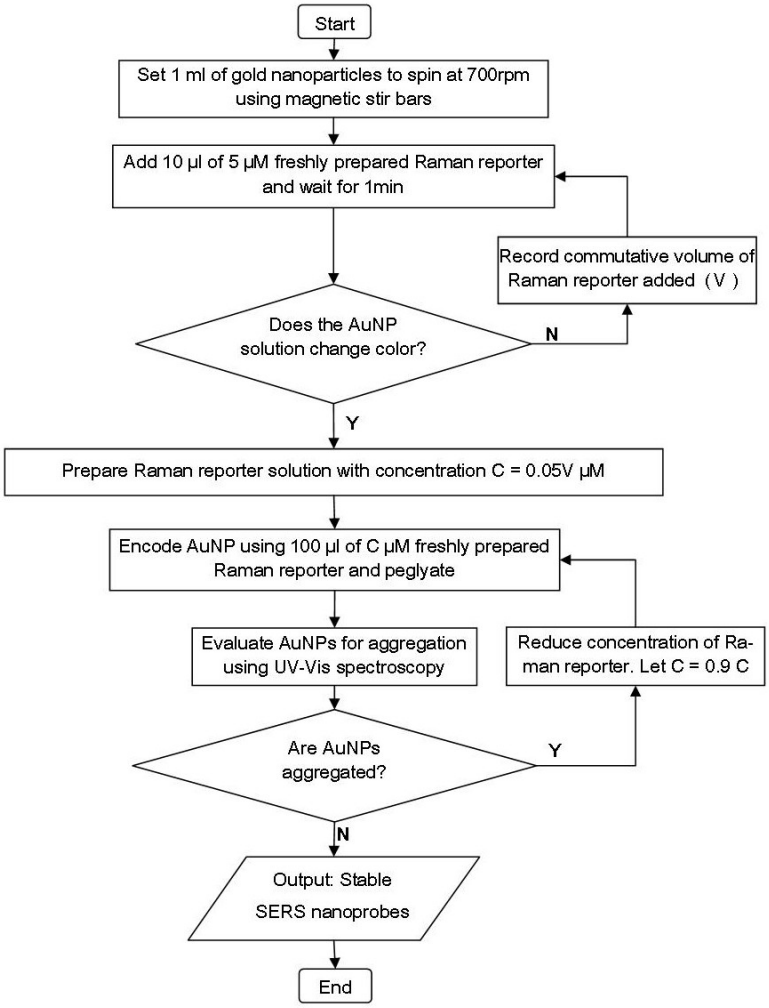

Figure 3-4 Flow chart summarizing optimization of the encoding proc ess

The encoded and peglyated gold nanoparticles (refered to as SERS nanoprobes) were then evaluated using UV-Vis spectroscopy to determine if aggregation had occurred. Presence of aggregation, indicated by appearance of a broad peak in the 700 nm region, prompted a

repeat of the encoding process with cresyl violet concentration at 90% earlier concentration. The process was repeated until a monodispersed SERs nanoprobes solution was obtained.

Results and discussion

Size different sizes (16.7 ± 1.7 nm, 43.9 ± 3.8 nm, 51 ± 3.1 nm, 65.6 ± 6.4 nm, 83 ± 5.1 nm and 114 ± 7.9 nm) of gold nanoparticles as determined by TEM were synthesized using citrate reduction(Fig 3.5 A-D) and seed growth method (Fig. 3.5 E-F). The sizes of the synthesized gold nanoparticles determined using transmission electron microscopy (TEM) were in close agreement to sizes determined using dynamic light scattering (DLS) (15.8 ± 0.6 nm, 35.1 ± 2.2 nm, 50.6 ± 4.7 nm, 62.9 ± 4.5 nm, 81.9 ± 3.96 nm and 116.7 ± 14.47 nm) shown in Figure 3.6. The gold nanoparticles were largely monodispersed and stable when stored in mild citrate solution (0.1%) for at least two months. The reduction of gold ions is described in equation 3.1.

$$2HAuCl_4(chloroauric\ acid) + 3C_6H_8O_7\ (citric\ acid) \rightarrow 2Au + 3C_5H_6O_5 + 8HCl + 3CO_2 \quad \text{.....3.1}$$

Gold atoms formed from the reduction process increase in concentration and eventually reach a critical concentrate where the gold atoms spontaneously combine, or nucleate, forming tiny particles of gold called nucleation sites. As the process continues, newly formed gold atoms combine with the nucleation sites resulting in growth of these particles into nanoparticles. As citrate ions are used up the rate of growth of the gold nanoparticles decreases (Fig 3.7). The resulting gold nanoparticles are coated with negatively charged citrate ions providing them with electrostatic stability. The observed colorimic changes mark the stages gold nanoparticle formation. The change of pale yellow color of chloroauric acid to blue black indicated the formation of nucleation sites while the gradual change of color from blue black to wine red is derived from the changes in optical properties of the gold nanoparticles as they grow.

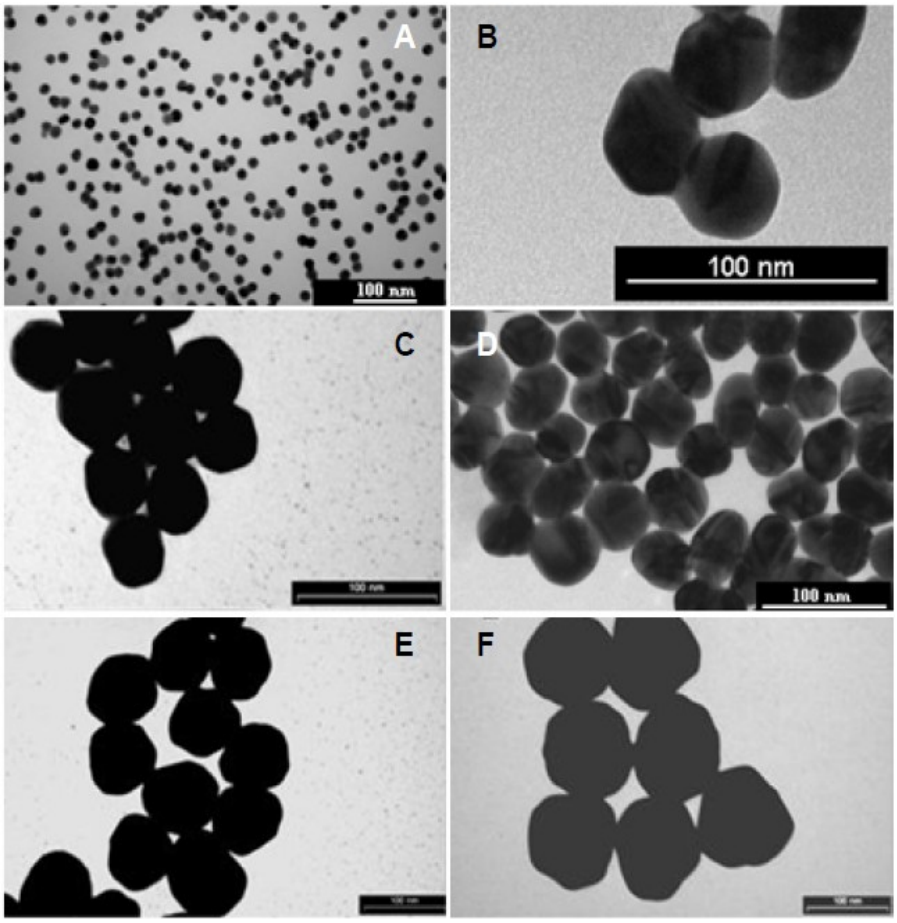

Figure 3-5 Solid gold nanoparticles of various sizes synthesized using citrate reduction method. Transmission electrom microscopy (TEM) images of gold nanoparticles: (A) 16.7 ± 1.7 nm, (B) 43.9 ± 3.8 nm, (C) 51 ± 3.1 nm, (D) 65.6 ± 6.4 nm, (E) 83 ± 5.1 nm and (F) 114 ± 7.9 nm

Encoded gold nanoparticles were analysed using UV-Vis spectroscopy, TEM (Fig. 3.8) and Raman spectroscopy (Fig. 3.9). A 3 nm red shift was observed when the encoded and peglyated gold nanoparticles' UV-Vis spectrum was compared to the UV-Vis spectrum of plain gold nanoparticles (Fig. 3.8 A). The red shift was not observed when gold nanoparticles that were only encoded with Raman reporter but not peglyated were interrogated. Therefore, it was attributed to the polyethylene glycol layer providing a reliable indicator of pegylation[41]. It may be explained by the change in dielectric constant expected in the environment immediately surrounding the gold nanoparticle[22]. Such a change would in turn affect the real dielectric

function of the gold nanoparticle resulting in a change in the local surface Plasmon resonance peak. Additional evidence of PEGlyation was observed in the form of a 5 nm coating visually discernible in TEM images (Fig. 3.8 B) of PEGlyated gold nanoparticles. The border of this coating was not at all times consistent with the geometry of the nanoparticles thereby discounting the possibility that the observed coating was an imaging artifact.

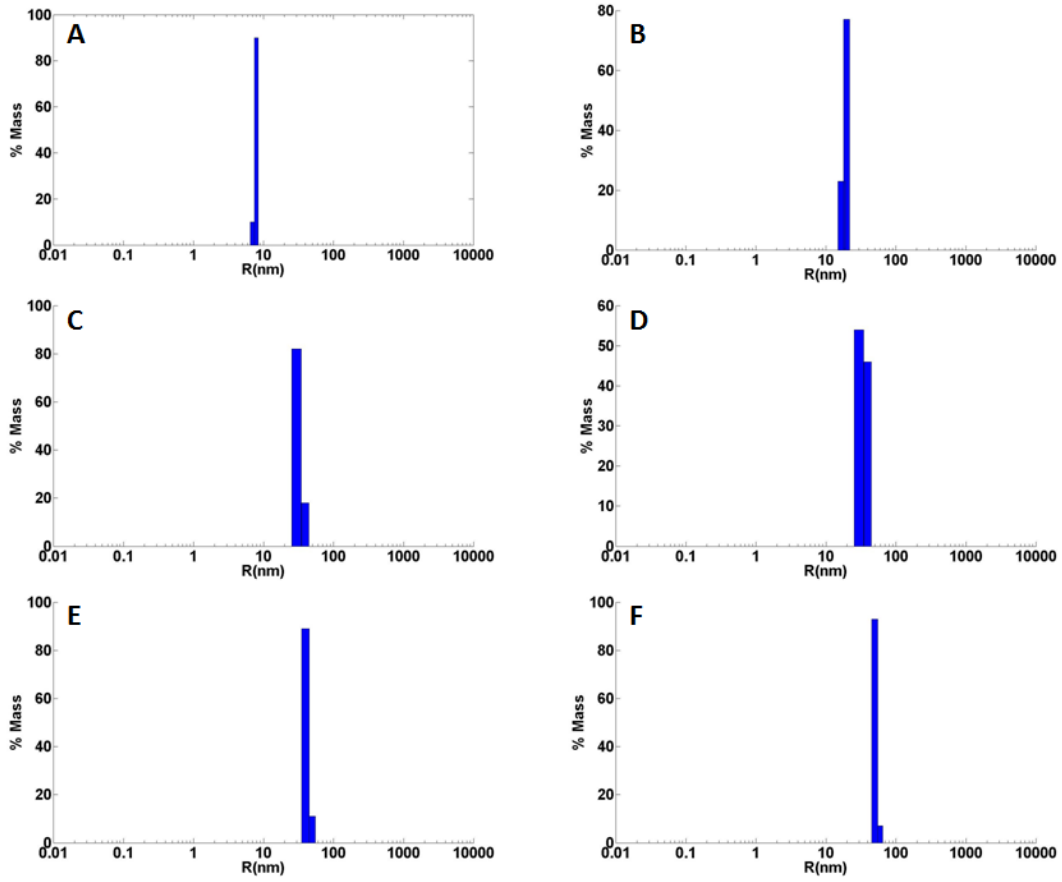

Figure 3-6 Size distribution of synthesized gold nanoparticles of various sizes. Dynamic light scattering (DLS) plots of synthesized gold nanoparticles: (A) 15.8 ± 0.6 nm, (B) 35.1 ± 2.2 nm, (C) 50.6 ± 4.7 nm, (D) 62.9 ± 4.5 nm, (E) 81.9 ± 3.96 nm and (F) 116.7 ± 14.47 nm. The size distribution shows that the synthesis process yields highly monodispersed nanoparticles which is critical for achieving highly reproducible SERS signal.

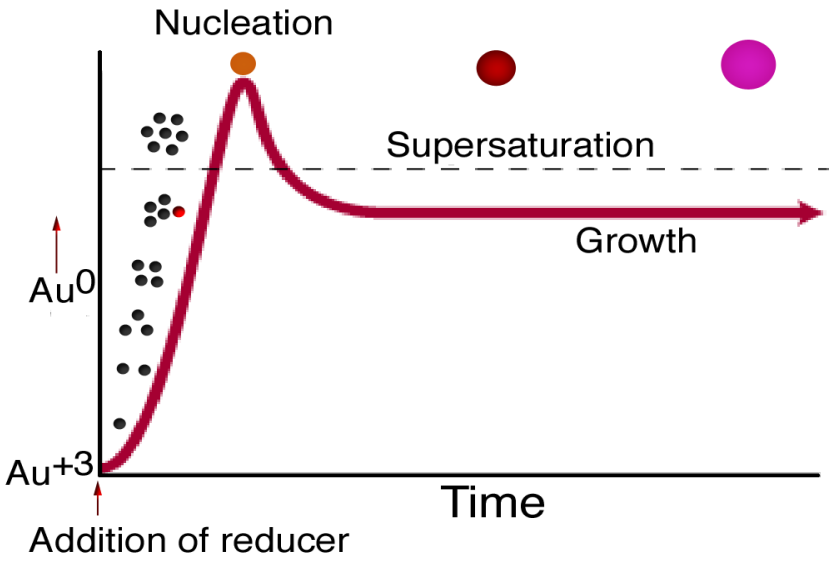

Figure 3-7 Schematic description of gold nanoparticle formation using the citrate reduction method. Gold atoms are formed from the reducing action of the trisodium citrate on chloroauric acid. The atoms increase in concentration until they exceed the saturation concentration. When they are supersaturated, the gold atoms spontaneously bind together to form nucleation sites. The remaining dissolved gold atoms bind to these nucleation sites resulting in the growth of the nanoparticles. The size of nanoparticle is controlled by controlling amount of trisodium citrate relative to chloroauric acid. (image source is http://mrsec.wisc.edu/Edetc/nanolab/gold/index.html)

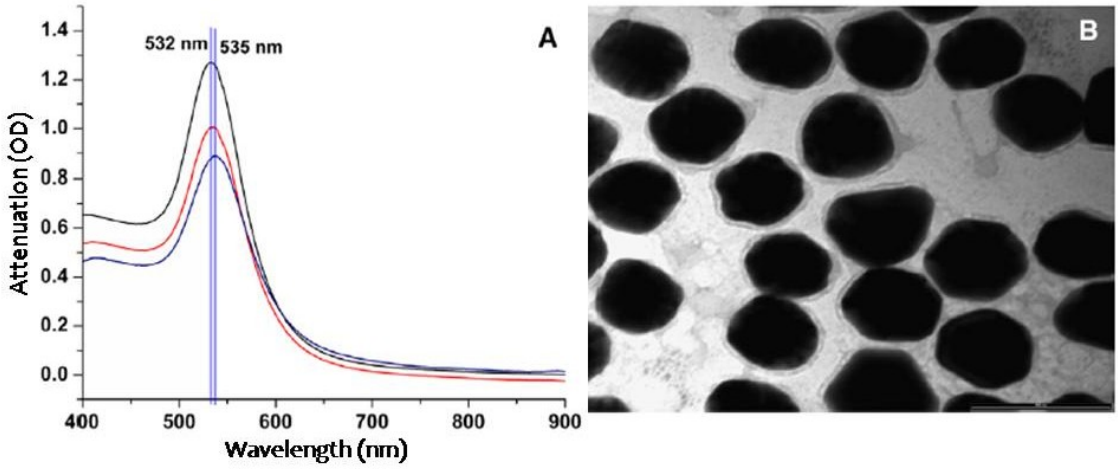

Figure 3-8 Extinction plots and TEM images of SERS nanoprobe. A 3 nm red shift in the extinction peak for both the PEGlyated gold nanoparticles (red line) and the SERS nanoprobes (blue line) compared to plain gold nanoparticles (black line) was indicative of the localized surface Plasmon . The film observed around the gold nanoparticles in the TEM image was indentified as polyethylene glycol layer.

Encoding of the gold nanoparticle by the Raman reporter was confirmed by Raman spectroscopy (Fig 3.9). Raman signals enhanced by 65.7 nm gold nanoparticles synthesized in the laboratory and 60 nm gold nanoparticles obtained commercially. The concentration of cresyl violet – the Raman reporter added to encode the gold nanoparticles - was 15 μM. Native Raman signal of the cresyl violet at this concentration was not detectable using Raman spectroscopy. However detection of SERS signal indicated adsorption of the Raman reporter on the gold nanoparticle. SERS effect is not observed to occur for Raman reporters at distances over 10 nm from the surface of the nanoprobes [30]. The enhanced Raman signal was present even after purification of the nanoprobes by three times centrifugation. Spectral differences were observed in the cresyl violet spectra from the two different types of nanoparticles were used. The differences observed were in the relative intensities of the vibrational modes while their positions remained identical. These differences were attributable to the shape of the gold nanoparticles and the orientation at which most of the nanoprobes were

adsorbed on the different nanoparticles. The gold nanoparticles synthesized in the laboratory were largely quasi-spherical (Fig. 3.8) while the commercially obtained gold nanoparticles were found to be spherical from TEM images.

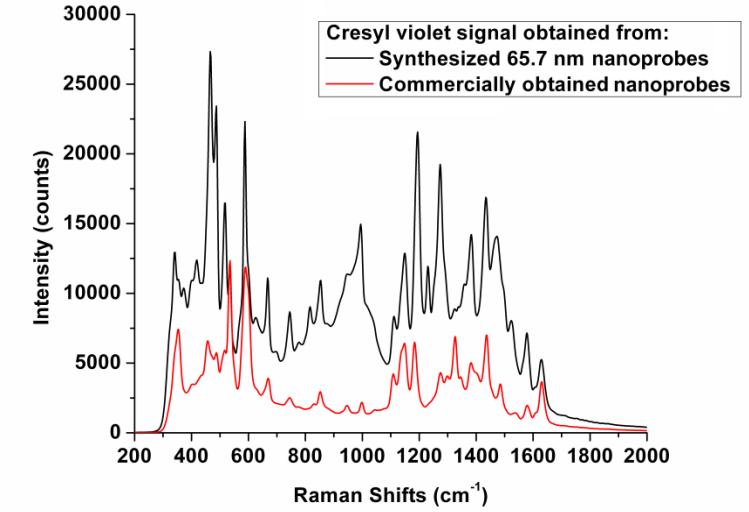

Figure 3-9 Raman spectra obtained from SERS nanoprobes synthesized using a commercially available ~60 nm spherical gold nanoparticle (red) and the laboratory synthesized ~65 nm quasi-spherical gold nanoparticle (black). The SERS nanoprobes are encoded with cresyl violet Raman reporter. The SERS nanoprobes prepared with the laboratory synthesized quasi-spherical gold nanoparticles have twice the SERS enhancement of spherical gold nanoparticles measured at the 590.09 cm^{-1} vibrational mode. The larger enhancement in quasi-spherical gold nanoparicles is attributable to the asymmetrical shape.

Evaluation of Gold nanoparticle Size effect on SERS Enhancement Factor (EF)

The most widely used definition of SERS EF is

$$SERS\ EF = \frac{I_{SERS}\ /N_{surf}}{I_{RS}\ /N_{vol}} \quad \text{.....3.2}$$

Where I_{SERS} is the intensity of the SERS signal for coded gold nanoparticles,

I_{RS} is the intensity of the native Raman reporter used to encode the nanoparticles

N_{surf} is the average number of Raman reporter molecules adsorbed on the nanoparticles in the scattering volume being measured and

N_{vol} is the average number of Raman reporter molecules in the scattering volume of the native Raman reporter solution.

Equation 3.2 presents a number of limitations for the experiment determination of SERS EF. Measurement of N_{surf}, the number of Raman reporter molecules adsorbed on the surface of the gold nanoparticles is not a trivial. Additionally, the nature and orientation in which these molecules are adsorbed whether, they form a monolayer or a multilayer would affect the value of the SERS EF because SERS mechanism is distance dependent. Raman scattering signals of the molecules near the surface of the gold nanoparticles would be enhanced at a different rate than the molecules that are further away. Therefore, a simpler but more intuitive definition for SERS EF called SERS analytical enhancement factor or SERS AEF [22, 51] was used.

$$SERS\ AEF = \frac{I_{SERS}/C_{SERS}}{I_{RS}/C_{RS}} \quad \text{.....3.3}$$

Where C_{SERS} and C_{RS} are defined as the Raman reporter concentration used in encoding the nanoparticle and concentration of native Raman reporter solution respectively.

For equation 3.3, I_{SERS} and I_{RS} have to be measured using the exact same parameters, specifically the incident laser power, scattering volume and the collection efficiency have to be fixed. This definition assumes that I_{RS} and I_{SERS} scale linearly with C_{RS} and C_{SERS} respectively. Both assumptions hold true in most experimental investigations [52-54]. To experimentally determine SERS AEF of the gold nanoparticles first a native Raman reporter solution is prepared by adding 10 mg of cresyl violet to 3 ml of water and mixing gently but thoroughly resulting in 9 mM solution of cresyl violet. Gold nanoparticles (1ml and 2.0 x 10^{10}ml^{-1}) were then coded by adding 100 µl of ~15 µM cresyl violet followed by PEGlyation as described in section 2.2.2. The concentration of the cresyl violet varied depending on the size of the gold nanoparticle. Evaluation of SERS EF was determined using equation 3.2 by comparing the intensities of Raman peak at 590.09 cm^{-1} vibrational mode of cresyl violet (table 3.1). SERS EF is shown to increase with reduction in nanoparticle size up till ~65 nm gold nanoparticles then the SERS EF reduces with reduction in nanoparticle size. This observation of an ~65 nm gold

nanoparticle as the optimal size for enhancement of Raman reporters using 785 nm laser excitation concurred with literature[41].

Table 3-1 Table comparing the sizes of the gold nanoparticle and the SERS analytical enhancement factors (AEF) associated with them. The greatest SERS AEF was recorded for ~65.6nm gold nanoparticle

Nanoparticle size (nm)	**SERS AEF**
16.7 ± 1.7	$1.85x10^5$
43.9 ± 3.8	$7.36x10^6$
65.6 ± 6.4	$2.83x10^7$
83 ± 5.1	$2.94x10^6$
114 ± 7.9	$1.13x10^6$

Conclusion

Size and shape of nanoparticles affect the optical properties of the nanoparticles[22, 55] and thereby affect the enhancement that is expected from the nanoparticles during SERS. Six sizes of gold nanoparticles (16.7 ± 1.7 nm, 43.9 ± 3.8 nm, 51 ± 3.1 nm, 65.6 ± 6.4 nm, 83 ± 5.1 nm and 114 ± 7.9 nm) were synthesized and evaluated as SERS substrates. The process of evaluation involved encoding of the gold nanoparticles to form SERS nanoprobes using an optimal concentration of cresyl violet for each size. An iterative process was used for determination of the optimal Raman reporter concentration. SERS EF of the gold nanoparticles range from 1.85×10^5 to $2.83x10^7$. The largest enhancement was found using 65.6 nm size gold nanoparticle.

Preparation of SERS Nanoprobe

Synthesis of multiple color of SERS nanoprobes required choice of Raman reporters that would make “good” SERS probes[22]. Parameters considered when selecting Raman probes included intrinsic parameters such as the Raman cross-section, Raman scattering spectrum and fluorescence excitation wavelength of the Raman reporter. Raman cross-section,

which provides a measure of the intensity of Raman scattering, is known to vary from molecule to molecule. For instance whereas as some Raman reporters such as cresyl violet and 2 thiouracil were found to have easily detectable native Raman signals, others such as nile blue were harder to detect. Raman cross-section is also particularly high for Raman reporters whose electronic energy is near the energy of the excitation laser. The phenomenon that occurs in this case is called resonant Raman scattering (RRS). Unique peaks in the Raman spectra of particular reporters allow for identification of Raman reporters in mixture and therefore SERS nanoprobes in a mixture. In addition to these intrinsic properties, the Raman reporter – gold nanoparticle interaction determines if enhancement will occur. SERS is a distance dependent phenomenon and therefore Raman reporters have to adsorb efficiently on the surface of the gold nanoparticle. Surface of gold nanoparticles prepared by citrate reduction are known to be negatively charged and have strong chemical affinity for the thiol functional group. Therefore Raman reporters were chosen that had either thiol groups or were electostatically positive.

Method

A literature search based on these parameters resulted in a list of 14 potential Raman reporters usable for preparation of SERS nanoprobes (Table 3.2). SERS nanoprobes with ~65 nm core and encoded with each of these 14 Raman reporters were prepared. Evaluation of the SERS nanoprobes was done using Raman spectroscopy at 785 nm incident laser wavelength and integration time of 10s.

Results and discussion

Optimal concentration for SERS nanoprobes encoding was determined for 11 of the 14 Raman reporters selected (Table 3.2). Three of the Raman reporters (4,4'-dipyridyl, 4-Azobis and Rhodamine 6G perchlorate) did not yield a Raman spectrum despite continuous addition to gold nanoparticle.

Table 3-2 List of potential Raman reporters

Name of Dye	Fluoresence Excitation Wavelength	Optimal concentration for encoding (μM)
2 Thiouracil	-	
5-(4-pyridyl)-1,3,4-oxadiazole-2-thiol	-	
4-tert-BulylBenzyl mercaptan	-	
4,4'-dipyridyl	-	Not found
4-Azobis(pyridine)	-	Not found
Rhodamine 6G perchlorate	560 nm	Not found
Rhodamine 6G tetrafluoroborate	560 nm	15
Crystal Violet	595 nm	15
Cresyl Violet	630 nm	15
Nile Blue	660 nm	15
DOTC Iodide	725 nm	5
HITC iodide	790 nm	5
DTTC iodide	815 nm	5
IR 140	882 nm	5

SERS nanoprobes with 11 of the Raman nanoprobes produced discernable Raman signatures and therefore constituted 11 Color SERS nanoprobes (Figure 3.10 and Figure 3.11). SERS nanprobes signals shown were processed post acquisition to remove the background using polynomial fit of n = 13 repeated over the data 11 times[56]. Raman reporters used varied in excitation wavelengths. Three of the Raman reporters: 2 Thiouracil, (5-(4-pyridyl)-1,3,4-oxadiazole-2-thiol and 4-tert-BulylBenzyl mercaptan were non-fluorescent dyes i.e. their peak absorbance is in the UV region. These Raman reporters showed strong native Raman scattering signal and are thiolated implying that adsorption onto the gold nanoparticle surface would be by gold-thiol chemistry. However, the Raman signal obtained from these Raman reporters was less in magnitude compared to the rest of the Raman reporters. Resonance Raman effect was considered responsible for the highest SERS signals are observed from SERS nanoprobes. Raman reporters for 2 color SERS nanoprobes (DTTC iodide and HITC iodide) with highest signal had excitation wavelength in the NIR. Additionally the intensities signals of the Raman reporters with excitation wavelength in the visible region: crystal violet, cresyl violet, nile blue and rhodamine 6G tetrafluoroborate were comparable to the intensities of

the non-fluorescent Raman reporters. The non-thiolated dyes used were all positively charged and were therefore were thought to attach to nanoparticles via electrostatic attraction. Selection of just any positively charged Raman reporter did not necessary result in enhancement. Specifically, while SERS intensity was observed when the gold nanoparticles were coated with rhodamine 6G tetrafluoroborate, no SERS signal was observed when the gold nanoparticles were coated with rhodamine 6G percholate. SERS nanoprobes colors with the highest signal intensities DTTC iodide (~2.4 $x10^4$ counts), HITC iodide (~3.9 x 10^4 counts), DOTC iodide (~6000 counts), IR140 (~1800 counts) and cresyl violet (~3150 counts) at their highest peaks were selected for *in vivo* and *in vitro* evaluations. Intensity counts for HITC iodide has been corrected to reflect 8s intergration time.

Table 3-3 Raman reporter used for synthesis of SERS nanoprobes. The vibrational modes of the Raman reporters are listed with Raman cross-sections for specific dominate vibrational modes

Name of Dye	Vibrational modes (cm^{-1})
2 Thiouracil	214.79, 349.63, 511.54, 573.56, 678.64, 713.04, 923.98, 1002.99, 1065.83, 1168.15, 1222.2, 1379.42, 1441.43, 1569.23, 1640.05,1699.02
5-(4-pyridyl)-1,3,4-oxadiazole-2-thiol	1032.45, 1220.21, 1348.94, 1398.34, 1491.32, 1544.07, 1578.17, 1611.91
4-tert-BulylBenzyl mercaptan	428.94, 511.54, 559.33, 641.6, 699.32, 744.88, 814.43, 847.64, 926.13, 1028.26, 1109.16, 1192.27, 1255.8, 1447.02, 1613.68, 2068.77
Rhodamine 6G tetrafluoroborate	301.8, 359.66, 608.9, 771.95, 998.77, 1182.24, 1307.24, 1358.49, 1504.79
Crystal Violet	206.57, 332.07, 419.11, 522.7, 722.17, 797.61, 1170.17, 1385.34, 1530, 1581.25, 1615.44
Cresyl Violet	276.4, 354.63, 455.85, 535.51, 545.95, 590.09, 599.51, 669.41, 735.81, 852.04, 949.79, 998.77, 1109.11, 1149.95, 1184.25, 1275.25, 1325.89, 1385.11, 1437.71, 1485.82, 1579.96, 1631.28
Nile Blue	196.84, 362.12, 436.3, 480.16, 545.05, 615.93, 664.79, 890.83, 945.5, 1074.12, 1111.21, 1178.22, 1196.28, 1275.63, 1432.11, 1483.98, 1581.74, 1636.54
DOTC Iodide	334.58, 377.07, 441.2, 504.32, 525.93, 592.45, 678.64, 749.4, 801.07, 880.54, 928.29, 964.77, 1005.11, 1080.33,

Table 3-3—*Continued*

Name of Dye	Vibrational modes (cm^{-1})
	1092.72, 1123.49, 1267.58, 1285.18, 1396.45, 1450.73, 1478.46, 1576.39
HITC iodide	299.26, 401.85, 501.91, 525.93, 554.58, 573.56, 634.62, 706.19, 747.14, 796.61, 930.45, 1017.75, 1038.73, 1084.46, 1121.45, 1234.09, 1271.5, 1294.91, 1364.2, 1403.99, 1465.55, 1579.96
DTTC iodide	379.55, 431.4, 489.84, 530.72, 622.95, 778.69, 843.23, 990.3, 1015.65, 1074.12, 1100.95, 1129.61, 1232.11, 1287.13, 1327.81, 1405.87, 1460, 1518.71, 1578.17
IR 140	537.89, 747.14, 863.03, 1036.64, 1086.53, 1135.73, 1174.2, 1238.05, 1308.5, 1432.11

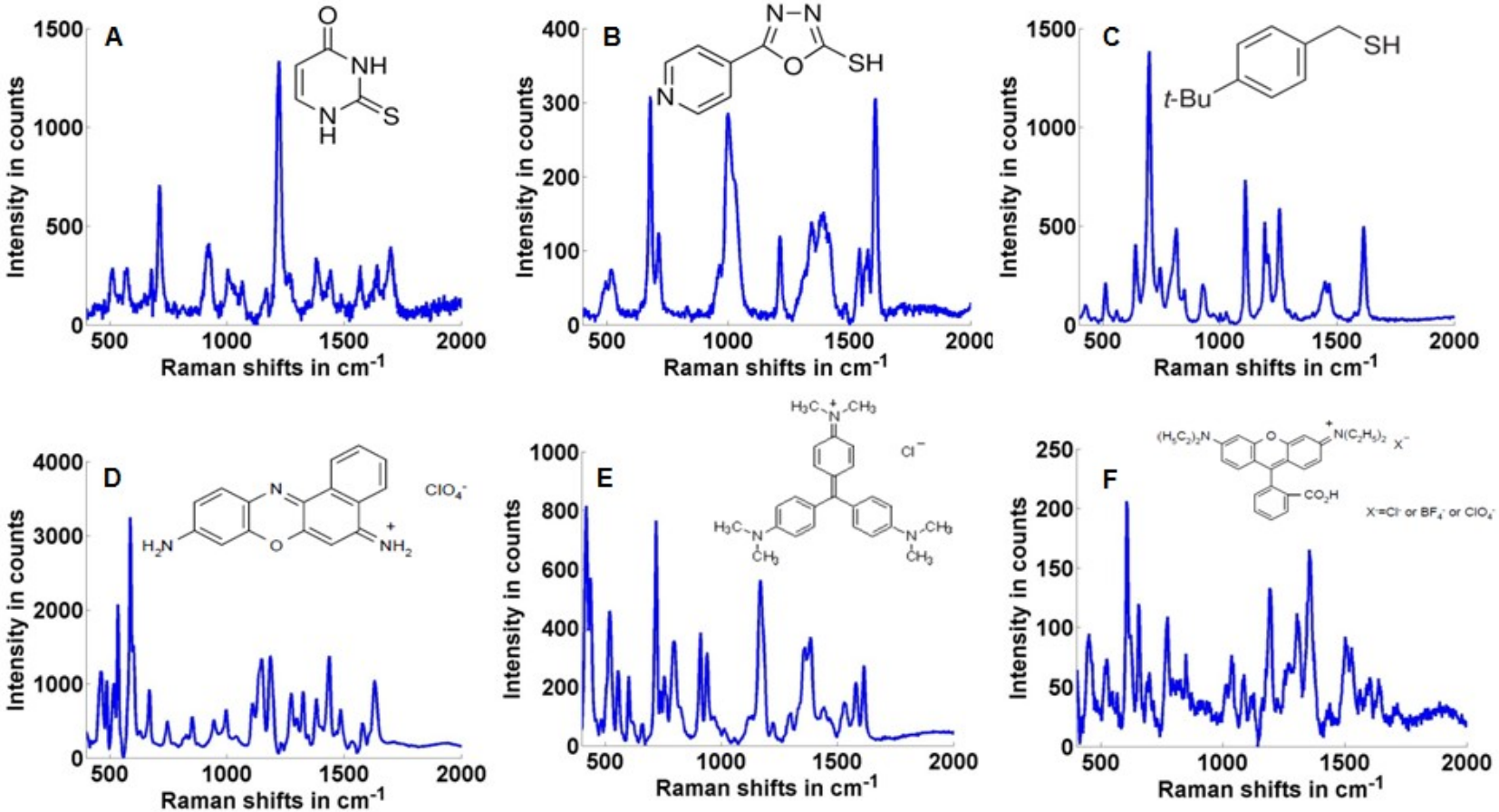

Figure 3-10 Six Raman spectral signatures of SERS nanoprobes synthesized with different Raman reporter encoding. A total of 11 different (colors) SERS nanprobes were synthesized encoded with Raman reporter dyes which include (A) 2 Thiouracil, (B) 5-(4-pyridyl)-1,3,4-oxadiazole-2-thiol, (C) 4-tert-BulylBenzyl mercaptan, (D) Cresyl Violet, (E) Crystal Violet, (F) Rhodamine 6G tetrafluoroborate. The SERS nanoprobes are measured at 785 nm and 8 – 10 s integration time

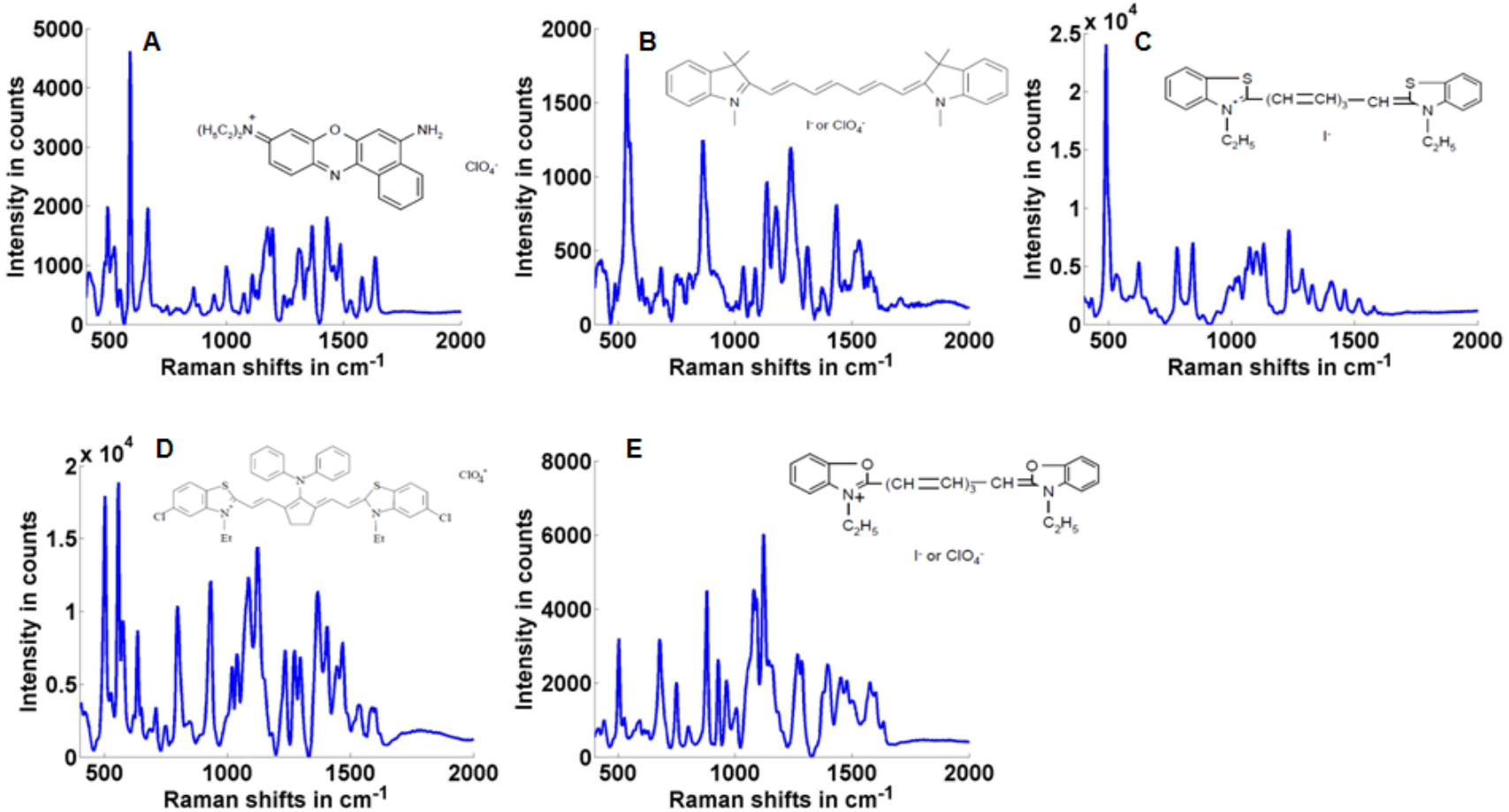

(A) Figure 3-11 Remaining five Raman spectral signatures of SERS nanoprobes. Raman reporter dyes includeNile Blue, (B) IR 140, (C) DTTC iodide, (D) HITC iodide, (E) DOTC Iodide. The SERS nanoprobes are measured at 785 nm and 8 – 10 s integration time except for HITC iodide encoded nanoprobes which was measured at 4s integration time

The linearity of the SERS nanoprobes in pure solution were tested at 1s integration time. The response of the SERS nanoprobes was found to be linear and encompassed a dynamic range of 300 fold. Figure 3.12 shows the dynamic range of DTTC SERS nanoprobes, one of the SERS nanoprobes selected for imaging. Large dynamic ranges allow the SERS nanoprobe to detect analytes over a wide concentration range therefore improving the potential of the SERS nanoprobes to be used for quantification[57, 58].

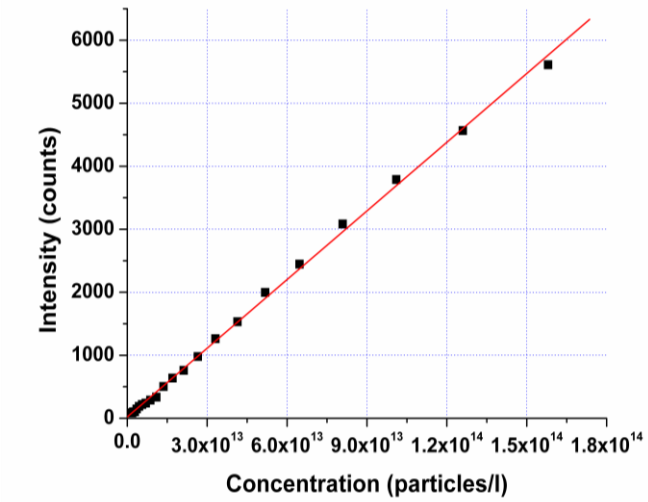

Figure 3-12 Dynamic range and sensitivity of the DTTC SERS nanoprobes. SERS signals of successively diluted SERS nanoprobes were measured in solution and the intensity of the 489.84 cm^{-1} vibrational mode plotted against concentration. SERS nanoprobes have a linear dynamic range of at least 30 db and are discernable upto a concentration of 1.83 pM

Colloidal stability of the SERS nanoprobes was investigated by centrifugation and resuspension of SERS nanoprobes in salt solutions, acidic solutions and in serum. In the absence of PEGlyation, the gold nanoparticles were observed to aggregate when salt solution is added to them. Aggregation of the gold nanoparticles was observed visually as a gradual change in color of the nanoparticles from wine red to dark blue then to colorless. Aggregation was also recorded using UV-Vis spectroscopy (Fig. 3.13 A). However, SERS nanoprobes retain their color even when resuspended in goat serum, PBS and MES solutions. The

extinction spectra of SERS nanoprobes dispersed in these solutions were observed to be similar to the extinction spectra of SERS nanoprobes dispersed in water (Fig. 3.13 B).

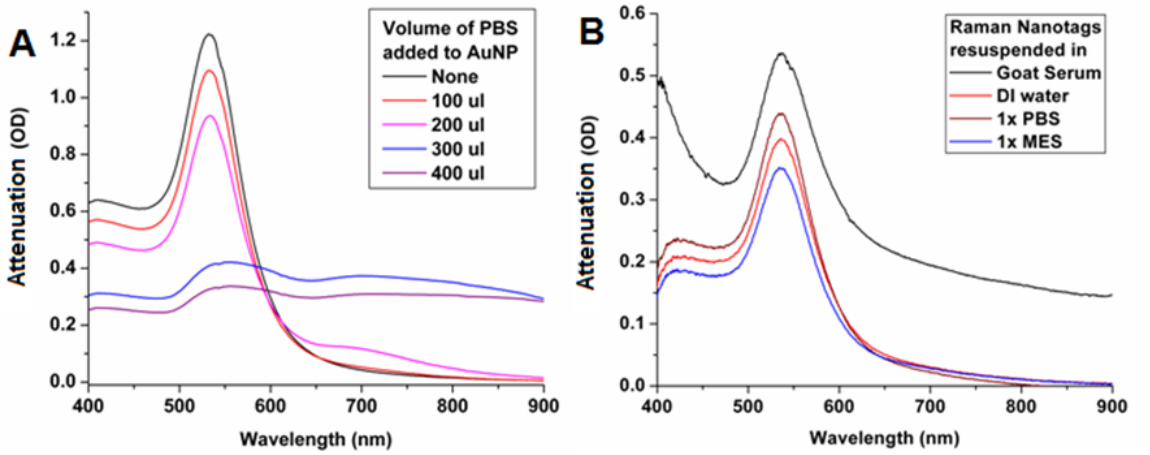

Figure 3-13 Stability of SERS nanoprobes for physiological environments was evaluated in comparison to plain gold nanoparticles using UV-Vis spectroscopy. A. The extinction spectrum of gold nanoparticles changes significantly as PBS solution is added to the nanoparticles. After addition of 400µl PBS solution, the gold nanoparticles have aggregated as evidenced by their extinction spectrum. However, SERS nanoprobes (B) centrifuged and resuspended in different solution do not aggregate. The extinction spectra retain the same shape with variations only in amplitude which is attributed to changes in concentration during centrifugation and resuspension process.

Colloidal stability was attributed to the polyethylene glycol coating which is known to lend nanoparticles steric stability[41]. The gold-sulfur bond formed when gold reacts with thiol groups on the mPEG-SH molecules are strong and are not easily displaced may many acids or bases allowing for the SERS nanoprobes to be stable in biomedical environments.

Conclusion

From a list of 14 Raman reporters, optimal concentration for encoding was determined for 11 which were used to encoded SERS nanoprobes. A total of 11 colors of SERS nanoprobes were prepared. The SERS nanoprobes have varying intensity from color to color ranging from 200 to 39000 intensity counts at 8s integration time. Five colors of SERs

nanoprobes (cresyl violet, DTTC iodide, DOTC iodide, IR140 and HITC iodide) were selected for *in vivo* and *in vitro* evaluation based on their intensities. In addition the SERS nanoprobes displayed linear dynamic range and colloidal stability.

Functionalization of SERS nanoprobes

Conjugation of antibodies to SERS nanoprobes was done using carbonyl reactive chemistry and involved two steps. Carbohydrate groups Fc region of the antibody were first activated and then conjugated to a bifunctional Hydrazide-PEG-SH linker. The antibody-linker complex was then adsorbed onto gold nanoparticles via thiol-gold chemistry. Conjugation of the antibody via the Fc region ensured that the antigen binding sites in the Fab region were directed away from the site where the antibody was adsorbed to the gold nanoparticle. Figure 3.14 illustrates the steps in the activation of the antibody. The adjacent carbon atoms that contain hydroxyl groups (cis-glycol groups) in the carbohydrate were activated by converting them to aldehyde groups through oxidation using sodium periodate ($NaIO_4$). $NaIO_4$ cleaves bonds between cis-glycol groups creating aldehyde groups. The aldehyde groups react readily with the hydrazide groups to form a hydrazone bond which despite being a Schiff base is considered sufficiently stable for protein labeling.

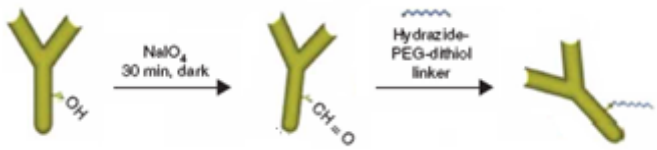

Figure 3-14 Two step carbonyl conjugation process of antibody to linker. First the cis-hydroxyl groups are activated using sodium periodate, then conjugation of linker to antibody through aldehyde-hydarzide bonding

Functionalization of the SERS nanoprobes using the activated antibody presented the possibility of competition for sites. Optimal process for conjugation of ligand was therefore investigated by exposing the nanoparticles to the antibody-linker molecule at different points during the sequence of SERS nanoprobe preparation. The dual goals of the preparation were to

ensure that the SERS nanoprobes remain coded with Raman reporter while also being conjugated to the antibody-linker molecule. To confirm adsorption of antibody on the gold nanoprobes and to determine reactivity of the SERS nanoprobes, the SERS nanoprobes were conjugated with anti-rabbit IgG and used to target rabbit IgG in a direct binding assay. The substrate of the binding assay was prepared using aldehyde commercially available glass cover slips.

Method

Antibody concentrations of 1 mg/ml were used while $NaIO_4$ is used at a concentration of 10mM. Sodium periodate oxidation is also light sensitive therefore the reaction were done in the dark for about 30 min. Control of $NaIO_4$ concentration and reaction time was important in order to limit oxidation the adjacent hydroxyl groups of terminal carbohydrates in the antibody. The linker molecules were added at 10 fold molar excess of the aldehyde groups in order to ensure cross-linking. Four groups of SERS nanoprobes were prepared (Fig 3.15). The control group (group 1) gold nanoparticles were peglyated using mPEG-SH and used as a reference for during evaluation of the SERS nanoprobes. In groups two, three and four the antibody-linker molecule was added after, with and before the Raman reporter respectively.

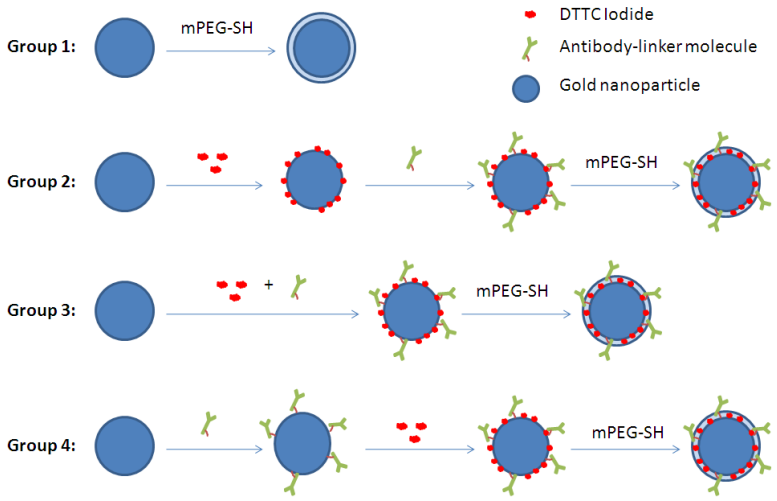

Figure 3-15 Preparation of four groups of nanoprobes for optimization of carbonyl reactive chemistry method for conjugation

Each of the groups was then peglyated. Evaluation of the four groups was done using UV-Vis spectroscopy and SERS spectroscopy. SERS nanoprobes were evaluated using UV-Vis and Raman spectroscopy. Raman spectroscopy was done at 785 nm laser set and 70 mW using a 10x, 0.25 NA collection lens (A-Plan, Zeiss). The spectra are collected at 2s integration time using high resolution Raman spectrometer (QE 65000, Ocean optics) and processed using Spectra Suite software. The signal was allowed to stabilize for about 10s then SERS measurement was recorded for consecutive signals.

Results and discussion

The peaks of the extinction spectra of samples in all four groups were red shifted with respect to the extinction maximum of plain gold nanoparticles (Fig 3.16). For group 1 the shift is consistently 3 nm. This corresponded exactly with previous experiments and was the expected shift resulting from peglyation [20, 41]. In group 2 and 4 red-shifts of 5 nm recorded both before and after peglyation provided evidence of adsorption of the antibody onto the gold nanoparticle. The extinction peaks for group three ranged from 4-5.5 nm indicating a less reproducible process compared to processes in 2 and 4. DTTC iodide SERS spectra was observed group 2 SERS nanoprobes yielded signals that were 1-2 orders of magnitude greater than the groups 3 and 4 SERS signals (Fig 3.17). This implied the DTTC iodide molecules adsorbed on the gold nanoprobe more efficiently when encoding is done before conjugation of antibody-linker solution.

The glass cover slip is incubated with rabbit IgG at 37^{o}C for 2h. Rabbit IgG readily binds to the glass cover slip. After the binding, the glass coverslip was wash and blocked using bovine albumen serum (BSA) before being incubated with the SERS nanoprobes at room temperature for 1h. The cover glass is then incubated with SERS nanoprobes that are not functionalized (control) and group 2 SERS nanoprobes. Each of the SERS nanoprobes is incubated at a concentration of $2.0 \cdot 10^{10} ml^{-1}$. After incubation the coverslips are washed to remove unbound nanoprobes and interrogated using SERS spectroscopy. Figure 3.18 shows

the SERS spectra obtained from the coverslips. SERS spectrum of DTTC iodide is observed in the coverglass incubated with group 2 SERS nanoprobes whereas no signal is observed from the control implying the anti-rabbit IgG remains active.

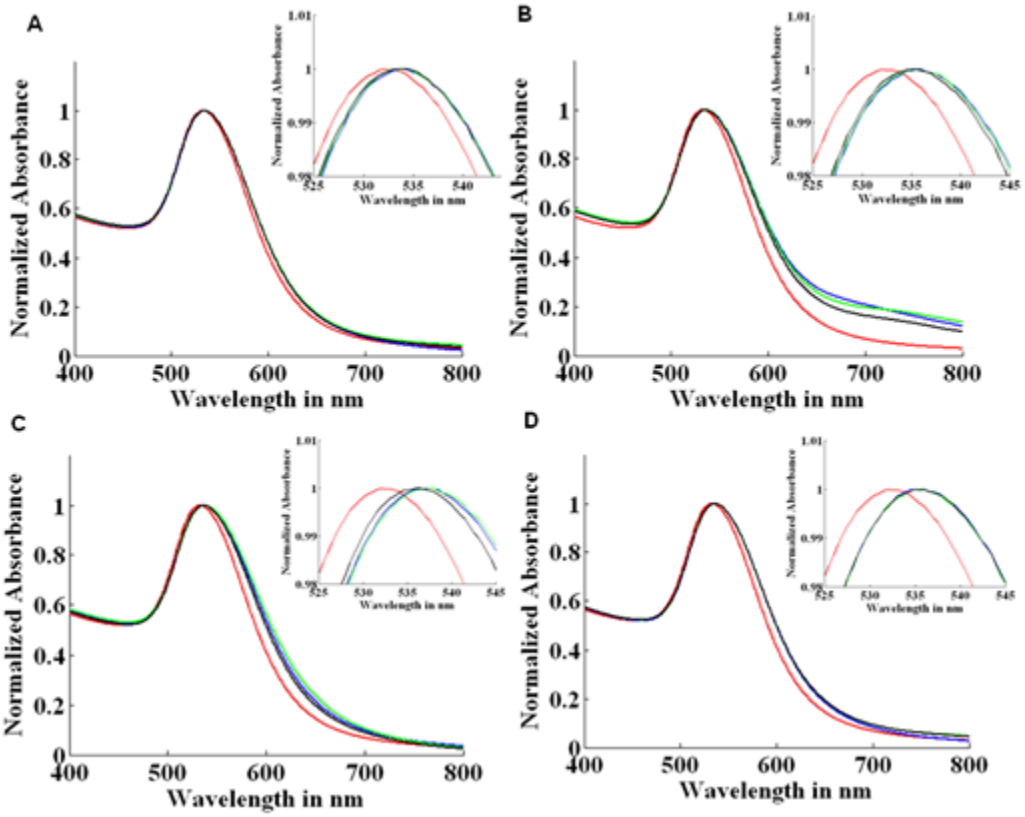

Figure 3-16 Extinction spectra of (A) group 1 samples, (B) group 2 samples, (C) group 3 samples and (D) group 4 samples.

Conclusion

SERS nanoprobes functionalization by conjugating antibody using carbonyl reactive chemistry was demonstrated. Conjugation was accomplished using the carbohydrate group in the Fc region of the antibody making it more likely that the binding sites of the antibody were exposed. Functionalization of SERS nanoprobes just after encoding and prior to PEGlyation was found to allow for retention of the greatest intensity of SERS signal while also ensuring

repeatable conjugation of antibody. Functionalized SERS nanoprobes remain and were able to selectively target anti-IgG antigen in a binding assay.

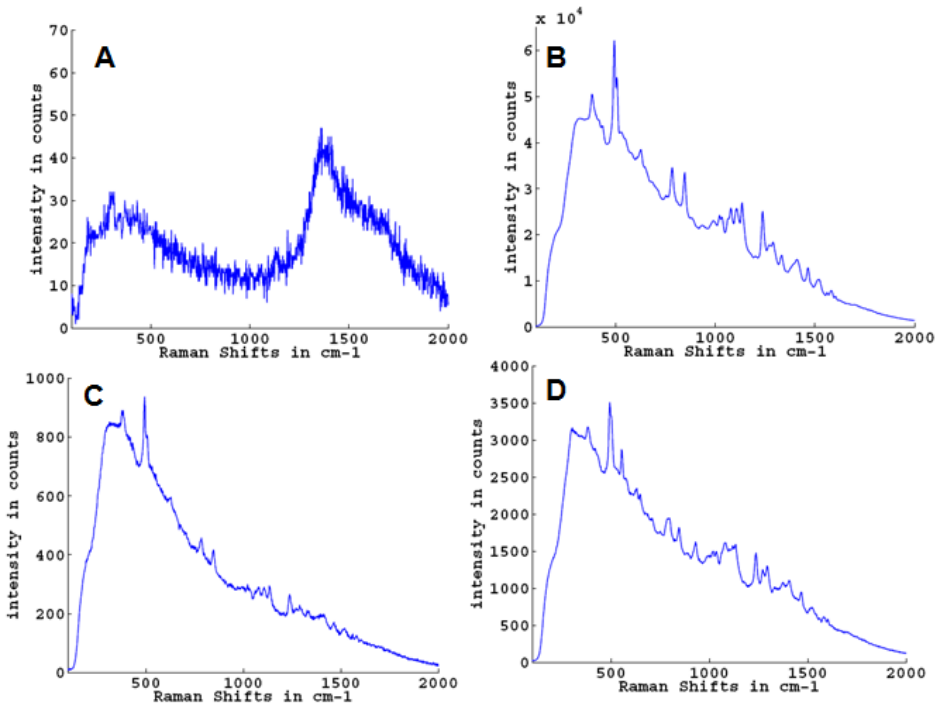

Figure 3-17 SERS spectra of (A) group 1 samples, (B)group 2 samples, (C) group 3 samples and (D) group 4 samples

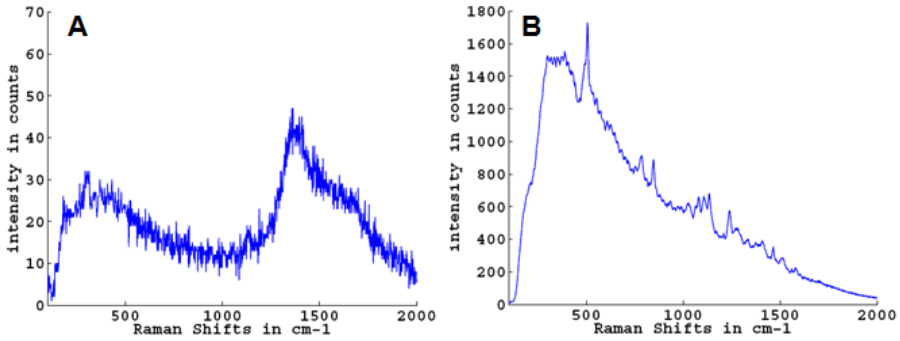

Figure 3-18 SERS spectra of (A) group 1 samples, (B) group 2 samples, obtained from direct binding assay

Summary

SERS nanoprobes were developed for *in vivo* and *in vitro* evaluation. The optimum size of core of the SERS nanoprobes, found by determining the SERS EF, was 65.6 ± 6.4 nm. An iterative process was used for determination of the optimal Raman reporter concentration for 11 out of 14 Raman reporters leading to the synthesis of 11 colors of SERS nanoprobes. Five colors of SERs nanoprobes (cresyl violet, DTTC iodide, DOTC iodide, IR140 and HITC iodide) were selected for *in vivo* and *in vitro* evaluation based on their intensities. SERS nanoprobes functionalization was accomplished by conjugating antibody using carbonyl reactive chemistry. Functionalized SERS nanoprobes remained reactive and retained their SERS signal.

Chapter 4

Quantitative Analysis of Multiplex Signal

Introduction

The five colors of SERS nanoprobes chosen (encoded cresyl violet, DOTC iodide, DTTC iodide, HITC iodide and IR140 respectively) have unique spectra distinguishable by their peak positions (Fig 4.1). A spectral analysis was developed to achieve three goals: (i) identify the SERS nanoprobes colors in a mixture, (ii) determine concentration of each SERS nanoprobes color and (iii) minimize operator bias.

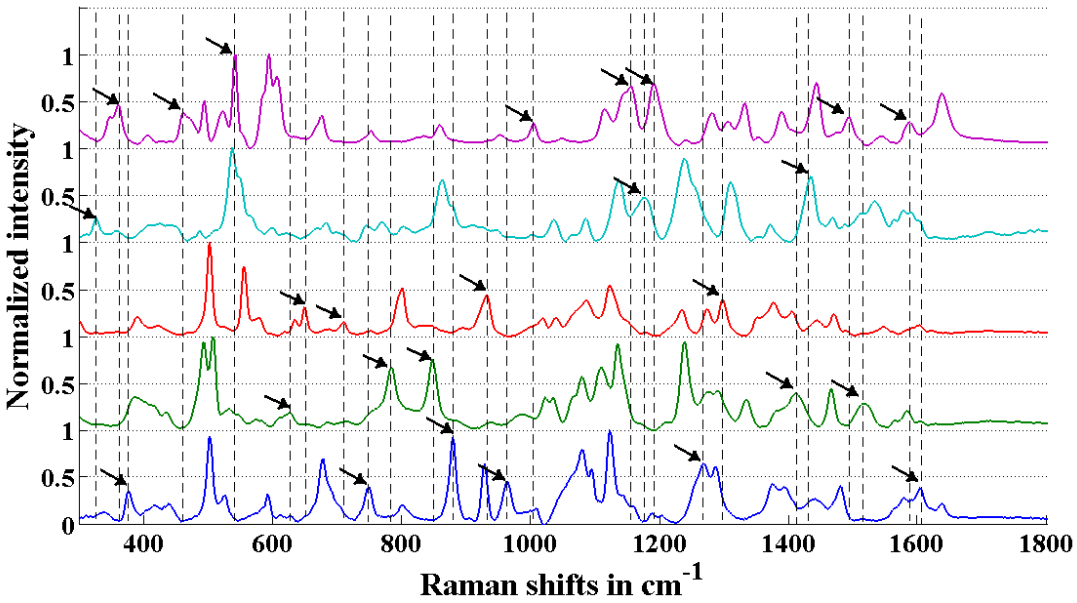

Figure 4-1 Multiplexing potential of four colors of SERS nanoprobes coded with Cresyl Violet (purple), IR140 (cyan), HITC iodide (red), DTTC iodide (green) and DOTC iodide (blue). Arrows identify at least three different peaks for each spectrum that may be monitored in a mixture to identify the SERS nanoprobes present.

Typically least square regression has been reported to accurately extract individual spectra of SERS nanoprobe colors from a mixture spectrum [52, 59, 60]. Least square regression relies on *a priori* knowledge of the individual color SERS spectra and background. However, there is potential for the Raman spectrum of the SERS nanoprobes to undergo

variations in its profile despite the vibrational modes retaining their specific positions in the spectrum. Spectral analysis using eigenspectra regression offered a method of identifying the colors of SERS nanoprobe. In Eigenspectra regression analysis the algorithm was first trained by exposing it to a host of spectra containing different ratio of SERS nanoprobes. The algorithm learns the profile of these mixture spectra storing them in a matrix called the regression coefficient matrix. The ratios SERS nanoprobes and their source spectra are then determined by applying the regression coefficient matrix to the mixture solutions.

Eigenspectra Algorithm

To develop the algorithm for quantitative analysis the Raman scattering spectrum of a mixture of SERS nanoprobes plotted with intensity against Raman shifts was considered. The spectrum was represented by a single row vector x_i with N elements. Where the value of each element was the intensity value of Raman scattering at a specific Raman shift and number *N* equaled the discrete number of Raman shift positions of the spectrum. Assuming *n* different mixtures of SERS nanoprobes were measured the signals obtained were represented by a matrix $X \in \Re^{n \times N}$. The Raman spectrum of each mixture was considered as a combination of *M* the number of different SERS nanoprobe colors mixed at a specific concentration. Since there are *n* samples the matrix representing these concentrations are stored in matrix $Y \in \Re^{n \times N}$ and the matrix containing the source signals was defined as $S \in \Re^{N \times M}$. The first part of the problem was to determine *Y* for an unknown mixed sample. By introducing a new matrix $B \in \Re^{M \times N}$, an equation for Y was written as

$$Y = XB + E_R \quad \text{..... 4.1}$$

Where E_R is the regression error and *B* is the regression coefficient matrix.

E_R in equation 4.1 is minimized to find *B* for known values of *Y* and *X* such that for any mixture x, unknown values of y may be determined by

$$y_i = x_i b \quad \text{.....4.2}$$

To determine the value *B*, an eigenspectra algorithm developed by Shuo et al[61] was used (Table 4.1).

Table 4-1 Pseudocode for Eigenspectra algorithm (obtained from Shuo et al[61])

Input: *X, Y, k*
Output: *B*

$X \leftarrow X - \bar{x}$
$Y \leftarrow Y - \bar{y}$
For $i = 0$ to *k* **do**
    if $\|Y\|$< *threshold* or $\|X\|$ < *threshold* **then**
        break;
    end if
    $A = XY^T YX^T$
    Initialize $\boldsymbol{w}_i$ as one column of X
    Repeat
        $\boldsymbol{w}_i = A\boldsymbol{w}_i$
        normalize $\boldsymbol{w}_i$ to make $\|\boldsymbol{w}_i\|$ = 1
    until convergence of $\boldsymbol{w}_i$
    $\boldsymbol{u}_i = X\boldsymbol{w}_i$
    $\boldsymbol{p}_i = X\boldsymbol{u}_i/(\boldsymbol{u}_i^T\boldsymbol{u}_i)$
    $\boldsymbol{c}_i = Y\boldsymbol{u}_i/(\boldsymbol{u}_i^T\boldsymbol{u}_i)$
    $X = X - \boldsymbol{p}_i\boldsymbol{u}_i^T$
    $Y = Y - \boldsymbol{c}_i\boldsymbol{u}_i^T$
end for
$B = C(P^T P)^{-1}P^T$

In the algorithm *X* and *Y* were first processed to obtain their mean vectors. Since, $N \gg n$ for each set equations where *y* is the subject, there are always more unknown values of b than there are equations. Therefore, *x* is mapped into a *k* dimensional subspace ($k \ll N$).

$$X = \sum_{i=1}^{k} p_i u_i^T + X_{k+1} \quad \text{.....4.3}$$

Where u_i the dimension score and p_i is the dimension loading and X_{k+1} is the residual matrix. Equation 4.3 can be rewritten

$$X = PU^T + X_{k+1} \quad \text{..... 4.4}$$

Where $P = (\boldsymbol{p_1}, \boldsymbol{p_2}, \dots, \boldsymbol{p_k})$ and $U = (\boldsymbol{u_1}, \boldsymbol{u_2}, \dots, \boldsymbol{u_k})$ may then be used to estimate X while minimizing X_{k+1}. *U* is the latent variable.

The latent variable *U* has to retain as close a relationship to *Y* as possible. Assuming that *U* and *Y* have a linear relationship and that *X* and *Y* are both zero-mean matrices,

$$Y = CU^T + Y_{k+1} \quad \text{.....4.5}$$

Where $C = (\boldsymbol{c_1}, \boldsymbol{c_2}, \dots, \boldsymbol{c_k})$ is the coefficient matrix $\boldsymbol{c_i} \in \Re^M$ and and Y_{k+1} is the residual matrix.

To obtain the value of *u*, the direction in *X* space onto which *X* is projected to get *u* can be defined using unit vector ***w*** such that

$$u_i = X_i^T \boldsymbol{w_i} \quad \text{..... 4.6}$$

In steps 7 to 12 an iterative method is used to find the value of $\boldsymbol{w}_i$ for which the largest component of X_i is mapped onto $\boldsymbol{u_i}$.

For the i^{th} iteration,

$$X_i = \boldsymbol{p_i u_i^T} + X_{i+1} \quad \text{..... 4.7}$$

From equation 4.4. By making the residual matrices in equations 4.3 and 4.4 minimal, the dimension loading $\boldsymbol{p}_i$ and regression coefficient $\boldsymbol{c}_i$ are determined as

$$\boldsymbol{p}_i = X\boldsymbol{u}_i/(\boldsymbol{u}_i^T\boldsymbol{u}_i) \quad \text{..... 4.8}$$

and

$$\boldsymbol{c}_i = Y\boldsymbol{u}_i/(\boldsymbol{u}_i^T\boldsymbol{u}_i) \quad \text{..... 4.9}$$

The matrices for the next iteration are then obtained by calculating the residual matrices

$$X_{i+1} = X_i - \boldsymbol{p_i u_i^T} \quad \text{..... 4.10}$$

and

$$Y_{i+1} = Y_i - \boldsymbol{c_i u_i^T} \quad \text{..... 4.11}$$

The process stops when there is no more information in X or Y or after k iteration. Thus equations 4.4 and 4.5 are calculated. From equation 4.4, the U^T may be written as

$$U^T = (P^TP)^{-1}P^TX \quad \text{..... 4.12}$$

Substituting for U^T in equation 4.5

$$Y = C(P^TP)^{-1}P^TX + Y_{k+1} \quad \text{..... 4.13}$$

Therefore the regression coefficient B is given as

$$B = C(P^TP)^{-1}P^T \quad \text{..... 4.14}$$

Validation of Eigenspectra Algorithm

Pure and mixture signals from cresyl violet and DTTC iodide encoded SERS nanoprobes were used in the initial test and development of the eigenspectra analysis method. Eleven different solutions were prepared of having different ratios of the DTTC iodide SERS nanoprobes to cresyl violet SERS nanoprobes ranging from 0:100, 10:90, 20:80… 100:0. The experiment was repeated five different times for each ratio. The raw spectra of the mixture solutions for the five repetitions and the mean signal obtained from the five repetitions were plotted in figure 4.2 A and B respectively. As the ratio of the mixture increased, the amount of DTTC iodide SERS nanoprobes increased while the amount of cresyl violet SERS nanoprobes reduced. The changes in relative concentrations of the two SERS nanoprobes were displayed the relative intensities of the two SERS nanoprobes. The increase in background of the SERS spectra with the increase in ratio can be traced to the fluorescence spectra of DTTC iodide whose fluorescence excitation wavelength is 763 nm which was close to the incident laser wavelength (785 nm).

A highly resolution Raman spectrum (QE65000, resolution ~ 0.48 nm) was used to measure spectral range of -79.65cm^{-1} to 2071.80 cm^{-1} (1044 pixels). To minimize noise and reject the measured Rayleigh scattering spectra between the 90th pixel value and the 990th pixel value were extracted. The data extracted and the ground truth ratios were used to form the mixture matrix $X \in \Re^{55 \times 901}$ and the ground truth ratio $Y \in \Re^{55 \times 2}$.

Validation of the eigenvector algorithm was done using leave-one-out (LOO) method. A single mixture is selected as test data while the 54 remaining signals were used as a training data. Once trained, the algorithm was used to determine and quantify the test data. The validation method was repeated until all mixture signals for each concentration of the SERS nanoprobes was selected once as test data.

The optimum value for k was determined by finding mean squared root of mean square (MSRMS) of error between actual and estimated concentration given by

$$MSRMS = \frac{1}{n}\sum_{j=1}^{n}\sqrt{\frac{1}{m}\sum_{i=1}^{M}(\tilde{y}_{i,j} - y_{i,j})^2} \quad \text{.....4.15}$$

Where $\tilde{y}_{i,j}$ are the estimated concentrations and $y_{i,j}$ are the actual concentrations at the i and j column of matrix Y. A smaller value for MSRMS indicates a more accurate estimation and therefore more optimum value for k.

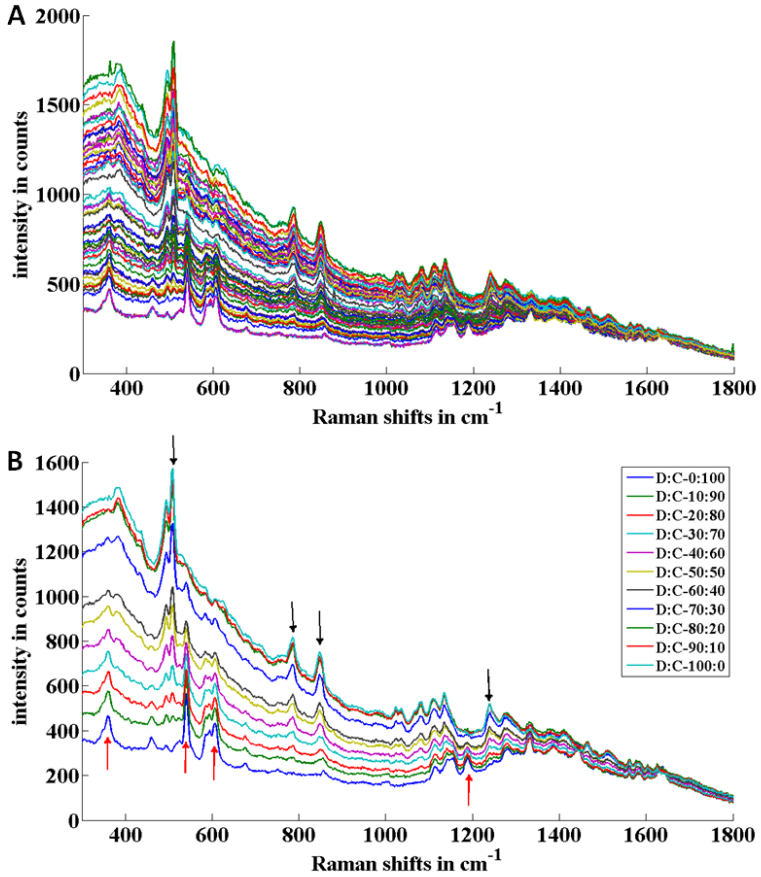

Figure 4-2 Raw Raman spectra (A) and mean Raman spectra (B) for twoplex SERS nanoprobes coded with DTTC iodide and cresyl violet. The ratio of DTTC iodide SERS nanoprobes to cresyl violet SERS nanoprobes ranged from 0:100, 10:90, 20:80 … 100:0. Raman spectra was observed to ride on the fluorescence background of DTTC iodide. Visual observations of the spectra reveals that as the ratio of the dyes increases peaks of cresyl violet (indicated by red arrows) reduce in intensity while those of DTTC iodide (indicated by black arrows) increase in intensity.

Results and discussion

Using algorithm 1, the eigenspectra for $k = 1 \ldots 12$ are calculated. The magnitude of the residual matrices $\|X_{i+1}\|$ and $\|Y_{i+1}\|$ found using equation 4.10 and 4.11 reduce with each iteration as predicted. The least value of MSRMS however was found at $k = 5$.

Table 4-2 Accuracy of the eigenspectra algorithm for different values of *k* measured using mean square ratio of mean square (MSRMS). Lowest MSRMS (*k* = 5) implies minimal error between actual and estimated values

k	$\|X_{i+1}\|$		$MSRMS$
1	0.0321	0.2919	4.6379
2	0.0175	0.1548	4.0753
3	0.0168	0.0743	1.6853
4	0.0155	0.0543	1.6606
5	**0.0104**	**0.0412**	**1.2553**
6	0.0069	0.0225	1.4994
7	0.0063	0.0102	1.4365
8	0.0062	0.0041	1.4103
9	0.0061	0.0016	1.3657
10	0.0060	0.0006	1.3907
11	0.0059	0.0002	1.3826
12	0.0058	0.0001	1.3820

The eigenspectra provided close estimation of the actual concentrations of both SERS nanoprobes colors (Table 4.2 and Fig. 4.3). Average error was calculated at 3.8% and 2.22% for CV and DTTC encoded SERS nanoprobes respectively. It is notable that the error for CV encoded SERS nanoprobes increased with decrease in concentration while the error for DTT encoded SERS nanoprobes was independent of concentration. The signal for CV encoded SERS nanoprobes have notable less intensity than DTTC encoded SERS nanoprobes and may be the cause of this variation in the trend of the errors of the two SERS nanoprobes.

Table 4-3 Actual and estimated concentration of SERS nanoprobes colors encoded with cresyl violet (CV) and DTTC iodide

Actual concentrations (ml^{-1})		Average of estimated concentrations (ml^{-1})		Error (%)	
CV	DTTC	CV	DTTC	CV	DTTC
0	1.1×10^{10}	-1.3×10^{8}	1.11×10^{10}	n/a	1.15
1.1×10^{9}	9.9×10^{9}	1.26×10^{9}	9.74×10^{9}	14.36	1.60
2.2×10^{9}	8.8×10^{9}	2.39×10^{9}	8.61×10^{9}	8.75	2.19
3.3×10^{9}	7.7×10^{9}	3.12×10^{9}	7.88×10^{9}	5.59	2.40
4.4×10^{9}	6.6×10^{9}	4.57×10^{9}	6.43×10^{9}	3.79	2.51
5.5×10^{9}	5.5×10^{9}	5.36×10^{9}	5.64×10^{9}	2.62	2.62
6.6×10^{9}	4.4×10^{9}	6.67×10^{9}	4.33×10^{9}	1.03	1.54
7.7×10^{9}	3.3×10^{9}	7.73×10^{9}	3.27×10^{9}	0.43	1.01
8.8×10^{9}	2.2×10^{9}	8.72×10^{9}	2.28×10^{9}	0.83	3.42
9.9×10^{9}	1.1×10^{9}	9.86×10^{9}	1.14×10^{9}	0.42	3.78
1.1×10^{10}	0	1.1×10^{10}	1.61×10^{7}	0.15	n/a

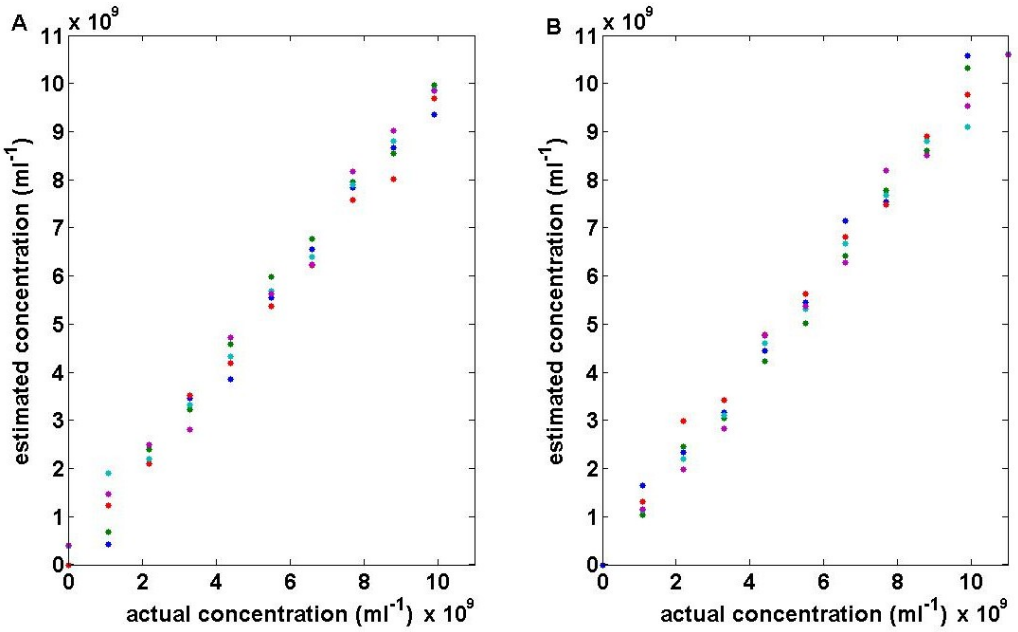

Figure 4-3 Plots comparing actual and estimated concentrations of (A) Cresyl violet SERS nanoprobes and (B)DTTC Iodide SERS nanoprobes. Estimated concentrations were determined using Eigenspectra regression algorithm

Conclusion

Quantitative analysis of SERS nanoprobes colors was demonstrated using eigen spectra algorithm based on principle component analysis. The eigen spectra algorithm does not rely on source spectra but calibration is accomplished using actual mixture signals and therefore in not affected by potential non-linear relationship between intensity and concentration. The potential limitation of the algorithm is in for discerning concentrations for SERS nanoprobes with weak signals.

Chapter 5

Evaluation Of SERS Nanoprobes For *In Vitro* Applications

Introduction

Immunofluorescence assay protocols have been used to elucidate the presence, distribution and localization of proteins in cells and tissue samples and are therefore well established. By adapting this protocol, a method was developed to evaluate SERs nanoprobes for detection of cell surface markers. Cells were cultured and divided into two groups (a control group and a text group) which are treated with targeted and non-targeted SERS nanoparticles respectively (Fig 5.1).

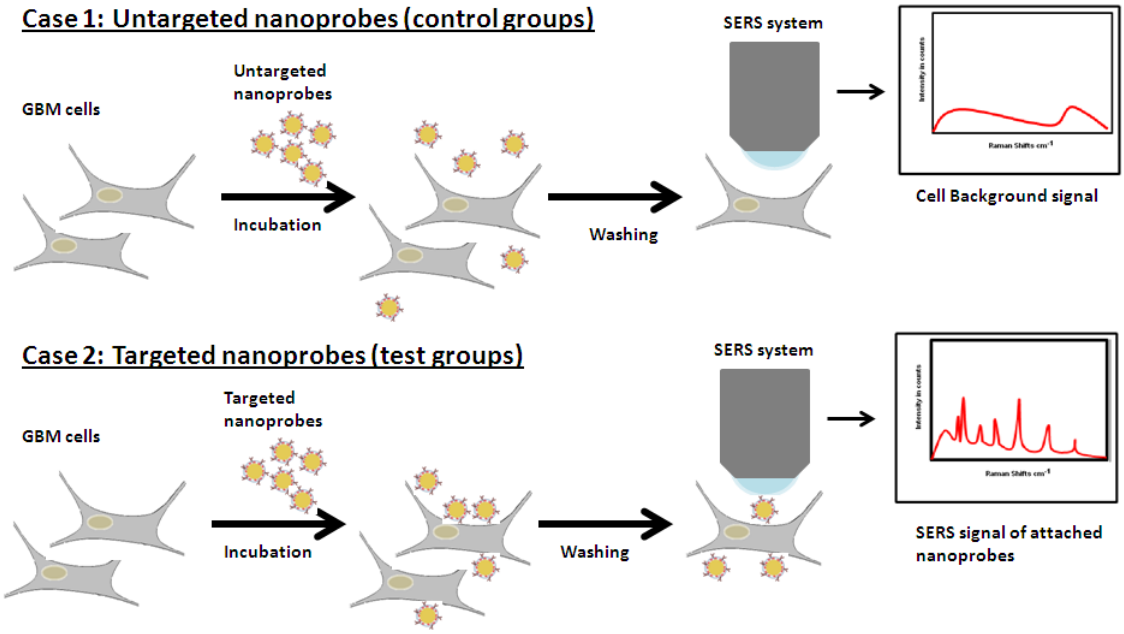

Figure 5-1 Scheme for evaluating SERS nanoprobes for *in vitro* application.Cultured cells are divided into two groups and treated with non-targeted and targeted SERS nanoprobes

Targeted as well as non-targeted SERS nanoprobes may be uptaken by the cells through endocytosis resulting in non-specific detection of SERS nanoprobes. None specific ligands attached to the SERS nanoprobes as wells as limiting the incubation time minimize uptake.

Specific attachment of targeted SERS nanoprobes in cancer cells was demonstrated using prostate cancer cell lines. Targeted SERS nanoprobes were evaluated for specific targeting of prostate specific membrane antigen (PSMA) expressing cell lines. Only cells in the test group tested positive for SERS nanoprobes indicating specific targeting of PSMA. Building on this result, the capacity to detect four colors of targeted SERS nanoprobes was evaluated. A second cell line, glioblastoma multiforme (U87 MG) cells were employed and four colors of targeted SERS nanoprobes in mixture were used to target EGFr on the cell surface. All four colors were identified from the mixed signal and quantified. Each of the colors of SERs nanoprobes was identified and quantified. A summary of the studies is presented in table 5.1.

Table 5-1 Summary of *In vitro* studies

	Objective	Target	Cell line	Result
5.2	Evaluation of SERS nanoprobe for targeted cell surface marker detection	PSMA	Prostate cell lines	Targeted SERs nanoprobes specifically detect PSMA positive cells
5.3	Evaluation of SERS nanoprobe for quantitative multiplex detection of cell surface markers	EGFr	U87-MG	Four-plex SERS nanoprobes were identified and quantified in U87-MG cells

5.2 Evaluation of SERS nanoprobe for targeted cell surface marker detection

Cell model for targeted SERS nanoprobe

Determination whether targeted SERS nanoprobes specifically label molecules of interest in biological environment was investigated by targeting prostate specific membrane antigen (PSMA). PSMA is a type II transmembrene glycoprotein expressed on prostate cancer epithelial cells [62, 63]. In contrast other prostate cancer biomarkers such as prostate specific antigen (PSA), PSMA is not secreted into circulation but is instead internalized when a ligand conjugates to it [64]. PSMA is well established as a prostate cancer biomarker and is expressed at all stages of prostate cancer [65]. PSMA has therefore been used as a prostate

cancer biomarker in several [62, 66, 67]. On the other hand PC-3 prostate cancer cell lines have are reported to be almost devoid of PSMA and are therefore a useful control[68]. SERS nanoprobes where therefore evaluated for targeted labeling by targeting PSMA in C4-2 and PC-3 prostate cancer cell lines. Two different colors of SERS nanoprobes were employed to demonstrate the potential for multiplexing.

Cell culture and labeling

C4-2 and PC-3 cells were cultured in T-media supplemented with 5% fetal bovine serum (FBS) and 1x Penicillin/Streptomycin. C4-2 cells express a prostate tumor specific molecular biomarker known as prostate specific membrane antigen (PSMA) where as the PC-3 cells do not express PSMA and served as a control. Cells were labeled using the classical immunocytochemistry method with the exception that SERS nanoprobes were used in the place of primary antibodies. Specifically, PC-3 and C4-2 cells were cultured in micro volume (100 µl) well plates made using PDMS stamps attached to treated no. 1 glass cover slips. Once confluent, the cells were fixed and blocked before antibody conjugated (functionalized) SERS nanoprobes were incubated in them for 2 h at room temperature and overnight at 4^{o}C. Antibodies conjugated to the SERS nanoprobes were anti-PSMA antibody used for targeting PSMA and anti-IgG antibody used as control. A three times with 1x PBS wash ensured unattached SERS nanoprobes were removed. Fluorescent secondary antibody was then added to the cells and incubated for 1 hour followed by three times PBS wash.

Results and discussion

Figure 5.2 shows the fluorescence microscopic images of SERS nanoprobe labeled C4-2 and PC-3. SERS nanoprobes were used to target PSMA that are expressed by C4-2 cells but not by PC-3 cells. The cells were then further labeled using anti-PSMA secondary antibody (green) and nuclear localized DAPI labeling (blue). PSMA was clearly identified in C4-2 cells (Fig 5.2 B green color) while they were not detectable in anti-IgG functionalized SERS nanoprobe labeled C4-2 cells or in PSMA negative PC-3 cells.

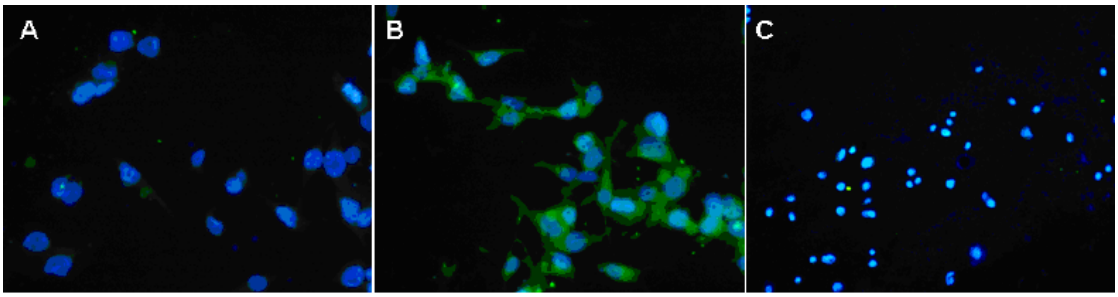

Figure 5-2 Fluorescence images of protate cancer cell lines labeled with targeted and non-targeted SERS nanoprobes. C4-2 cells (A and B) were labeled with non-targeted and targeted SERS nanoprobes respectively and PC-3 cells (C) were labeled with targeted nanoprobes. Targeted SERS nanoprobes were conjugated with anti-PSMA while non-targeted SERS nanoprobes were conjugated with anti-IgG antibody. Cells were further stained with using fluorescent anti-PSMA secondary antibody (green) and DAPI (blue). Green fluorescence was only observed in panel B suggesting that targeted nanoprobes specifically bind to PSMA positive C4-2 cells.

The cells were then visualized using DIC microscopy and using the 785 nm Raman module incorporated into the microscope Raman spectra of regions of interest on cell surface were interrogated. The experiment was repeated to two separate colors of SERS nanoprobes, DTTC iodide and cresyl violet, as shown in Fig. 5.3 A and B respectively. The intensity of the SERS signals detected in Raman spectra obtained from C4-2 cells targeted with anti-PSMA antibody functionalized SERS nanoprobes suggest labeling of PSMA. In contrast the SERS signals from controls where PSMA positive cells were labeled using anti-IgG functionalized SERS nanoprobe were comparable to background and cells where PSMA negative cells are labeled with anti-PSMA antibody were weak. The weak signals were attributed to non specific binding. The results correlate exactly with the fluorescence results in Fig 5.2.

Conclusion

The experiments demonstrated specific targeting of cell surface markers using functionalized SERS nanoprobes. Anti-PSMA antibody functionalized SERS nanoprobes

exhibited specificity to PSMA positive prostate cancer (C4-2) cell lines. This specific attachment occurs irrespective of the Raman reporter used to code the SERS nanoprobe. In a broader picture, the result indicates that the SERS nanoprobes developed when targeted can be used to detect more than one surface marker.

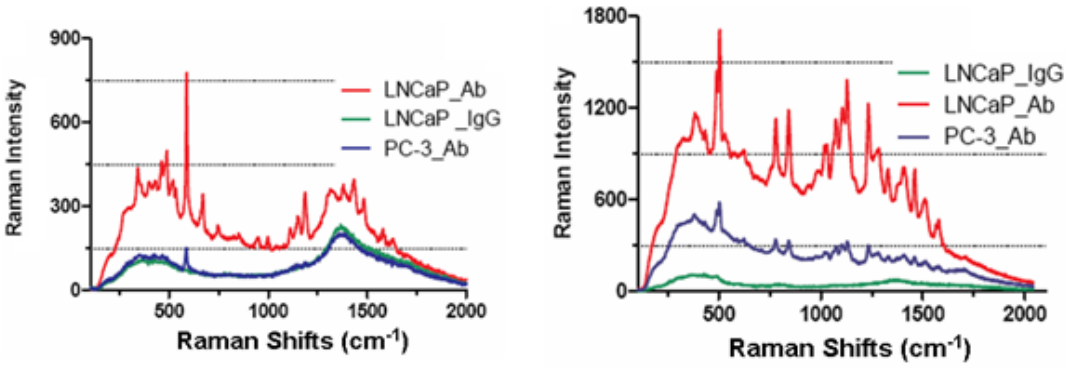

Figure 5-3 Raman spectra recorded from cells labeled with (A) cresyl violet coded SERS nanoprobes and (B) DTTC iodide coded SERS Nanoprobes. In each case the SERS signal was detected in PSMA positive C4-2 cells labeled with anti-PSMA functionalized SERS nanoprobes (red line). No SERS signal was observed in PSMA positive C4-2 cells labeled with anti-IgG antibody functionalized SERS nanoprobes (green line) however slight signal was detected in PSMA negative PC-3 cells labeled with anti-PSMA antibody functionalized SERS nanoprobes. The slight signal was attributed to non-specific binding.

Evaluation of SERS nanoprobe for quantitative multiplex detection of cell surface markers

Cell model for targeted SERS nanoprobes

Glioblastoma astrocytoma cells (U87 MG) cell lines, originally derived from grade three cancer patient, are astocytic glial cells found in the brain. These tumor cells overexpress epidermal growth factor receptors(EGFr). Specifically, EGFR expression which is present in normal tissue (40,000 to 100,000 receptors per cell) is multiple in cancer tissue (up to 2 million EGFRs per cell in breast carcinoma) [69]. In Glioblastoma Multiforme about 40%-60% of the tumor cells show over expression of EGFr [69-73]. Although EGFR has a number of endogenous ligands including EGF, transforming growth factor-α (TGF-α), amphiregulin,

heparin-binding EGF (HB-EGF) and betacellulin[74], several monoclonal antibodies can be used to target it.

Cell culture and labeling

Reactivity of targeted SERS nanoprobes was determined using U87 MG cells seeded in 48 well-plate. The cells were cultured DMEM media supplemented with 10% fetal bovine serum and 10% Penicillin/Streptomycin. 24 h after seeding two groups of 12 wells were labeled with targeted SERS nanoprobes and non-targeted SERS nanoprobes respectively while a third group of 12 wells is left unlabeled. Targeted SERS nanoprobes and non-targeted SERS nanoprobes respectively described nanoprobes to which anti-EGFr antibody or anti-IgG antibody.

Four-plex labeling of cells surface markers was evaluated using four colors of targeted and non-targeted SERS nanoprobes each encoded with a different Raman reporter: HITC iodide, DTTC iodide, DOTC iodide and IR140. Targeted SERS nanoprobes were prepared by conjugation to anti-EGFr antibody while the non-targeted nanoprobes were conjugated to anti-IgG antibody. The SERS spectra of all the nanoprobes are recorded before incubation for calibration. Mixed solutions of SERS nanoprobes were incubated in two groups of 12 wells each in a 48 well-plate each seeded with U87-MG cells. The two group (test group and control group) were seeded with targeted and non-targeted SERS nanoprobes respectively. After incubation for 4 h at 37oC the cells were washed three times using PBS to remove unbound SERS nanoprobes and then detached using trypsin. The detached cells were enriched by centrifugation before Raman spectroscopy was done to measure the SERS spectra.

Results and discussion

Raman spectra of SERS nanoprobes obtained from the test group of U87-MG cells indicate presence of targeted SERS nanoprobes (Fig. 5.4 blue line). The signal from the control has similar intensity to the background signal implying that the non-targeted SERS nanoprobes did not attach to the cell (Fig. 5.4 red and green lines). Concentration of SERS

nanoprobes from each group of cells (Fig. 5.6) was determined using calibration curve (Fig 5.5) which shows a linear dynamic range $(R^2 = 0.96)$. The results indicated that anti-EGFr antibodies on the SERS nanoparticles remained reactive and are able to conjugate to EGF receptors on cells while SERS nanoprobes functionalized with anti-IgG antibodies which are specific to the U87-MG cells did not conjugate to the cells.

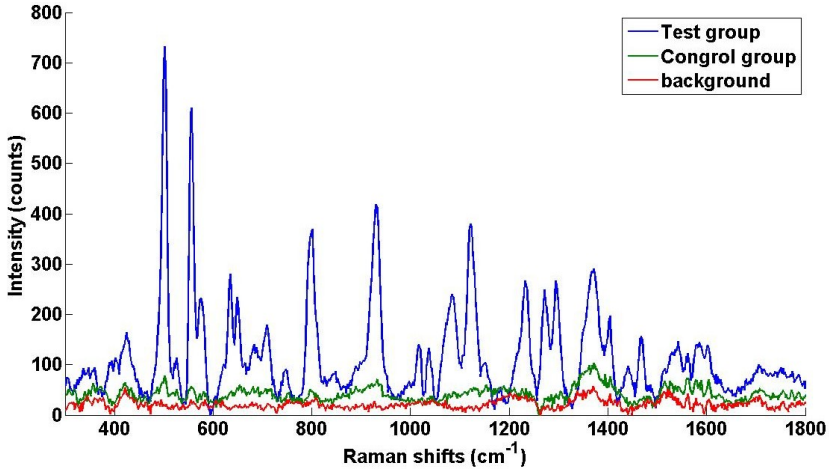

Figure 5-4 SERS spectra of HITC encoded SERS nanoprobes from plain U87 MG cell (background) and cells labeled with targeted SERS nanoprobes (Test group), untargeted SERS nanoprobes (control group) .

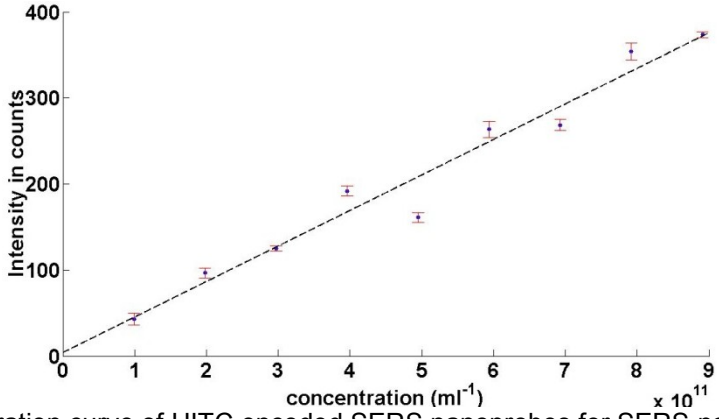

Figure 5-5 Calibration curve of HITC encoded SERS nanoprobes for SERS nanoparticles with the concentration range 1.0x10^{11} to 9.9x10^{11} ml^{-1}. A linear dynamic range was observed (R^2 = 0.96)

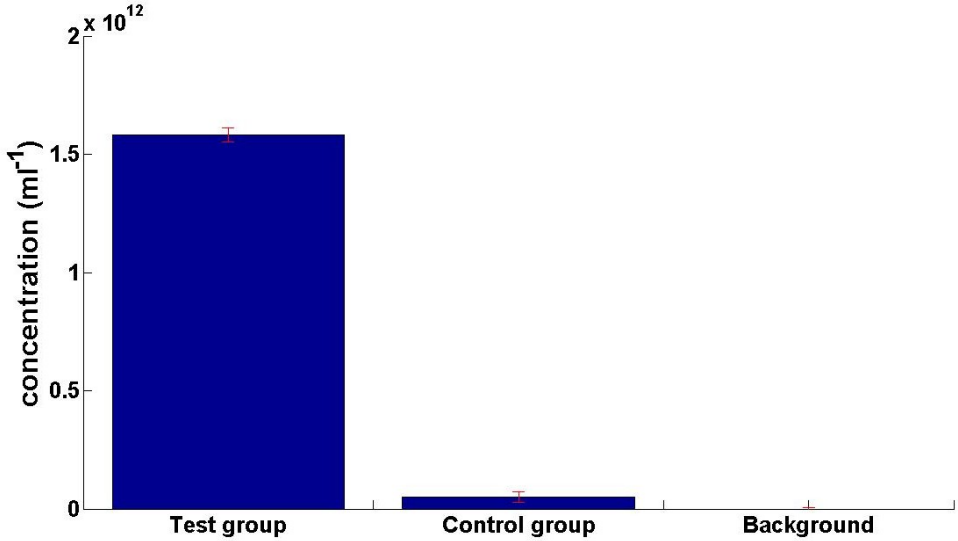

Figure 5-6 The intensity of 501.91 cm^{-1} vibration mode of HITC iodide measured from test, control and background groups of cells (n = 12).

Raman spectrum from U87 MG cells (Fig 5.7 E) to which four colors of targeted SERS nanoprobes, encoded with DOTC iodide, DTTC iodide, HITC iodide and IR140 (Fig. 5.7 A-D) were incubated was positive for all of the four SERS nanoprobes colors. Peaks from each of the four SERS nanoprobes (shown by the arrows) were identified in the Raman spectra collected test group cells. No such peaks were observed in cells labeled with non-targeted SERS nanoprobes (Fig 5.8). Spectral analysis of the Raman spectrum from the test group resulted in a non-uniform concentration for each of the SERS nanoprobes colors (Fig 5.9). This was non-intuitive since each of the SERS nanoprobes was conjugated with the same target ligand. The non-uniformity may be attributed to the replacement of the Raman reporter by the targeting ligand in a non-uniform manner.

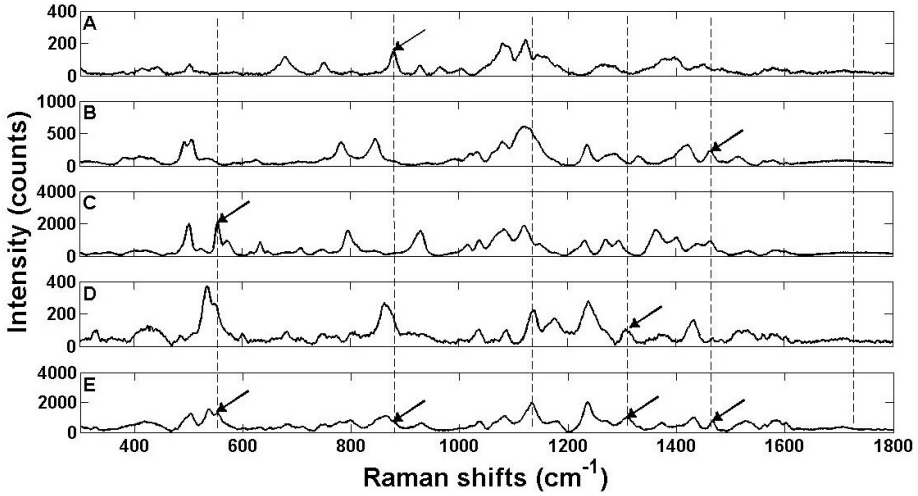

Figure 5-7 Raman Spectra from U87 MG cell lines conjugated with multiple targeted SERS nanoprobes. Raman spectrum of mixed SERS nanoprobes (E) obtained from U87 GM cells labeled with targeted SERS nanoprobes encoded with DOTC iodide (A), DTTC iodide (B), HITC iodide (C) and IR140 (D). Anti-EGFr antibody was used as the targeting ligand.

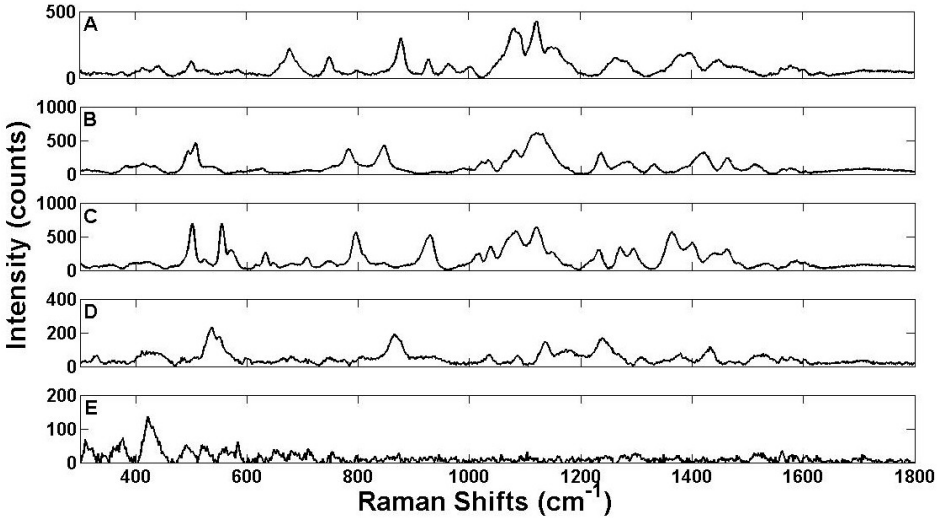

Figure 5-8 Raman Spectra from U87 MG cell lines conjugated with multiple non- targeted SERS nanoprobes. Raman spectrum of mixed SERS nanoprobes (E) obtained from U87 GM cells labeled with non-targeted SERS nanoprobes encoded with DOTC iodide (A), DTTC iodide (B), HITC iodide (C) and IR140 (D). Anti-IgG antibody was used as the targeting ligand

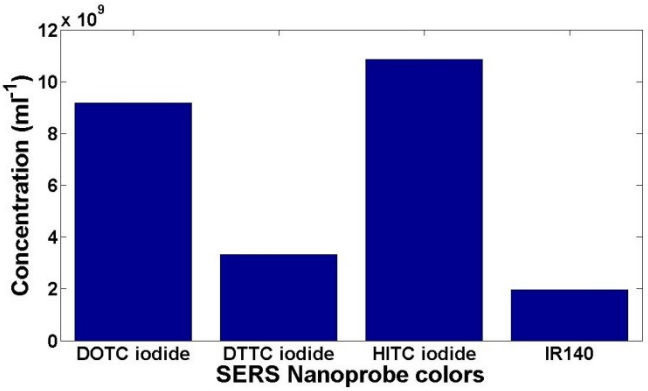

Figure 5-9 Concentration of targeted SERS nanoprobes in the U87 MG cells. SERS nanoprobes colors are identified by the Raman reporter used to encode the nanoprobes

Conclusion

Simultaneous detection of four color of targeted nanoprobes was demonstrated in glioblastoma multiforme (U87 MG) cell lines. First reactivity of the anti-EGFr antibody conjugated to the targeted SERS nanoprobes was determined using single color SERS nanoprobes. Four-plex detection of SERS nanoprobes was then evaluated by labeling U87-MG cells with targeted SERS nanoprobes each conjugated with anti-EGFr antibody. Conjugation with a single antibody allowed for evaluation of the detected concentrations. Intutively, the concentrations were expected to be similar however significant variation was observed in the concentration of the SERS nanoprobes in the detected sample.

Summary

In this chapter, targeted SERS nanoprobes evaluated for in vitro applications were found to specifically detect cell expression of interest. Anti-PSMA antibody functionalized SERS nanoprobes exhibited specificity to PSMA positive prostate cancer (C4-2) cell lines and anti-EGFr targeted SERS nanoprobes exhibited specificity to U87-MG which overexpress EGFr. Simultaneous detection of four colors of SERS nanoprobes was demonstrated in glioblastoma multiforme (U87 MG) cell lines targeted with four-plex mixture SERS nanoprobes. In this proof-of-principle study, SERS nanoprobes were demonstrated to attach were detectable.

Chapter 6

Evaluation of SERS Nanoprobes For *In Vivo* Applications

Introduction

In this chapter, SERS nanoprobes are evaluated for (i) multimodality SERS detection and CT imaging and (ii) transdermal delivery (table 6.1). Selection of modalities for clinical diagnostic imaging face a unique challenge. Modalities with high sensitivity such as optical modalities and PET tend to have poor resolution, while those with high resolution like CT and MRI have poor sensitivity[75]. SERS nanoprobes can be detected both by SERS spectroscopy and by CT since their gold nanoparticle core attenuates X-rays. In addition non-invasive delivery of diagnostic and therapeutic agents the subject of increasing interest in research [76, 77]. Transdermal delivery offers (i) miminal invasiveness including reducing pain during treatment, (ii) improving pharmacokinetics and (iii) targeted delivery[78].

SERS nanoprobes were evaluated for dual SERS/CT contrast. X-ray attenuation of SERS nanoprobes were was measured in comparison to iodine based CT contrast agents. SERS nanoprobes were then evaluated for *in vivo* SERS/CT contrast subcutaneously and using an orthotropic tumor model.

Separately, SERS nanoprobes were also evaluated for transdermal delivery. First, uptake of topically applied targeted SERS nanoprobes into xenograph prostate tumor in nude mouse was investigated. SERS monitoring suggested the SERS nanoprobes do not get trapped at the application site but dynamically accumulate. A second study was then done to confirm accumulation and clearance of SERS nanoprobes.

Table 6-1 Summary of experiments evaluating SERS nanoprobes for in vivo applications. SERS nanoprobes were evaluated for multimodality SERS/CT imaging and Transdermal delivery

	Study	Objective	Mouse model	No of mice
6.2	Dual SERS/CT constrast	Evaluate Combined SERS and CT Contrast of SERS nanoprobe	Nude mice Subcuteneously injected with SERS nanoprobes	3
		Demonstrate dual SERS detection and CT imaging	Prostate cancer orthotropic tumor model	5
6.3	Transdermal Delivery	Transdermal uptake of SERS nanoprobes	Xenograft prostate tumor model (nude mice)	3
		Accumulation and clearance of Transdermally delivered SERS nanoprobes	Xenograft prostate tumor model (nude mice)	6

Dual CT/SERS multimodality

Introduction

Unlike conventional contrast agents, contrast from nanoparticles can be derived from imaging moieties integrated with nanoparticles[79-81] as well as from inherent contrast properties possessed by the nanoparticles themselves. In recent years metal nanoparticles have been exploited to enhance contrast in whole body imaging modalities such as MRI [82-85] and CT [86-89] as well as optical imaging modalities such as fluorescence and surface enhanced Raman spectroscopy [18, 41, 90, 91]. Metal nanoparticles have also displayed additional advantages including prolonged blood circulation half life, better controlled biological clearance pathways and specific molecular targeting capabilities [92, 93].

In this study SERS nanoprobes were demonstrated to possess dual CT and SERS contrast usable for multimodality CT imaging and SERS detection [89]. X-ray contrast is derived from the high electron density and atomic number of the gold nanoparticle core [87, 94, 95] of SERS nanoprobes and can be exploited in CT imaging to provide contrast between soft

tissues. Currently CT contrast between soft tissues is improved using iodine-based compounds. However, iodine-based compounds have a high clearance rate providing a short imaging window[20]. An ideal contrast agent capable of allowing for both global and specific detection of a lesion has to be retained in the lesion long enough for preoperative and post operative imaging. The SERS nanoprobes were characterized first in an *in vitro* for X-ray attenuation and SERS signal. The SERS nanoprobes were then injected *in vivo* subcutaneously in live mice and detected using Raman spectroscopy and CT imaging. Finally an orthotropic model was employed. Results demonstrate that SERS nanoprobes remain stable in vivo and possess dual SERS/CT contrast.

SERS nanoprobes and CT imaging

SERS nanoprobes with gold core size of 65.6±6.4 nm and 43.9±3.8 nm were used for the study. The SERS nanoprobes were coded with DTTC iodide and protected by PEGlyation. Raman spectroscopy is done using the 785 nm Raman module at 10s using 10x 0.25 NA lens. Characterization of X-ray attenuation of the SERS nanoprobes and CT imaging of mice was achieved using a Siemens Inveon PET-CT Multimodality System (Knoxville, TN). CT images were obtained at 80 kV and 500 mA with a focal spot of 58 μm. The total rotation of the gantry was 360◦ with 360 rotation steps obtained at an exposure time of approximately 225 ms/frame. Under low magnification the effective pixel size was 103.03 μm. CT images were reconstructed with a down sample factor of 2 using Cobra reconstruction software. Reconstructed images were analyzed using the Siemens Inveon research workplace (IRW) software.

CT Contrast of SERS nanoprobes

SERS nanoprobes with gold core size of 65.6±6.4 nm and 43.9±3.8 nm were evaluated for CT contrast using a Siemens Inveon PET-CT scanner. 1.5 nm plastic vials filled with serially diluted solutions of SERS nanoprobes and firmly attached on the imaging bed then scanned. X-ray attenuation values measured by the scanner are plotted against molar concentration of the nanoprobes (Fig 6.1). For comparison, x-ray attenuation of serially diluted solutions of Iohexal

(Omnipaque™, GE Healthcare) were similarly obtained. The nanoprobes were found to have CT contrast that is linearly dependent on concentration. This CT contrast is also higher than molar equivalent concentrations of Iohexal reported by Xu et al[96].

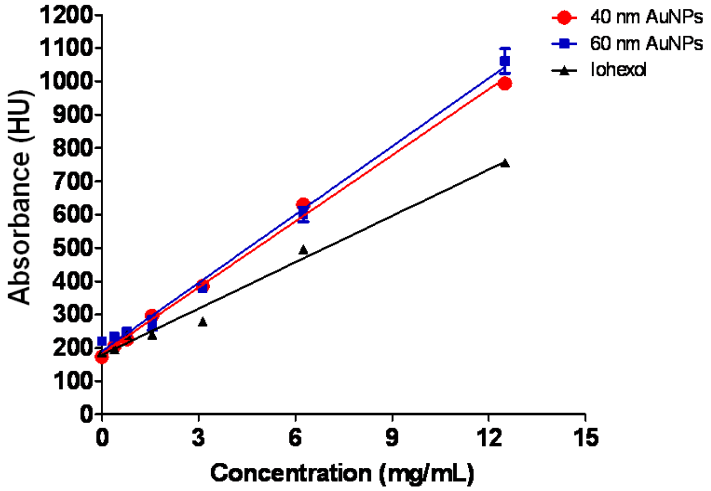

Figure 6-1 Measured x-ray attenuation of gold nanoparticles (40 and 60 nm AuNPs) and Iohexol as a function of their concentration. The three constrast agents display linear dynamic with the gold nanoparticles displaying greater contrast than iohexal. The offset in the plots is due to the x-ray attenuation in the plastic vials used to hold the solution for the measurements.

In vivo CT Contrast of SERS nanoprobes

In vivo CT contrast of the SERS nanoprobes was determined by CT imaging three Balb/c mice injected with 65.6±6.4 nm gold core SERS nanoprobes pre and post injection. The mice were fasted overnight then sedated using 2% isofluorine anesthesia before CT scanning. Each mouse was then injected intravenously with 100ul of 12.5mg/ml of SERS nanoprobes. Post injection scanning is done after 24 h. The spleen was clearly visible in the post injection CT image (Fig. 6.2 B) compared with the pre-injection image (Fig. 6.2 A). Additionally, measured CT attenuation of the spleen in the post-injection image was found to be 432 HU which was significantly higher than the CT attenuation of the surrounding tissue (100 HU). The CT attenuation values were determined by image quantification of the CT images. To further confirm presence of the SERS nanoprobes in the spleen, the spleen is excised and imaged

using TEM (Fig. 6.3). The SERS nanoprobes are clearly identified in the TEM image surrounded by membrenes which suggest that they are uptaken by endosomes[97].

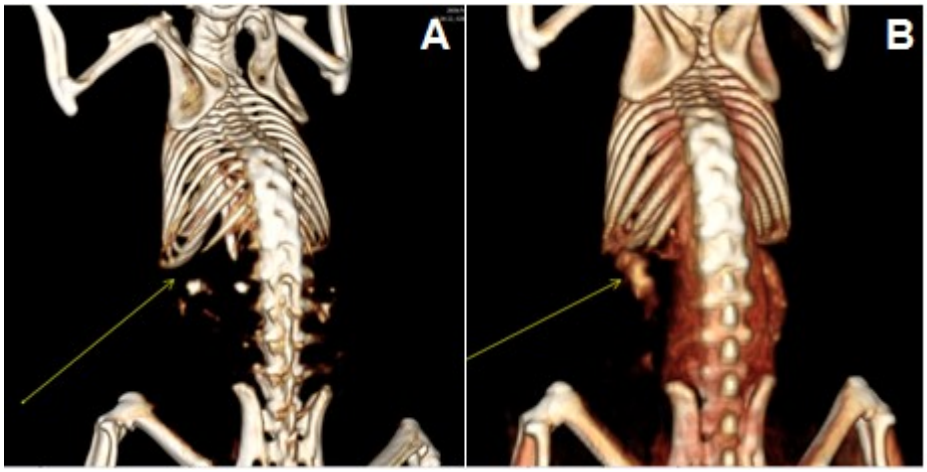

Figure 6-2 Three dimensional Computed tomography (3D-CT) images of a mouse (A) pre injection and (B) post injection with 100µl of 12.5mg/ml of ~65nm nanoprobes. The location of the spleen is indicated by the yellow arrows. In the pre-injection image the spleen is not clearly visible but in the post-injection the spleen is revealed due to the nanoprobes that are uptaken into the spleen.

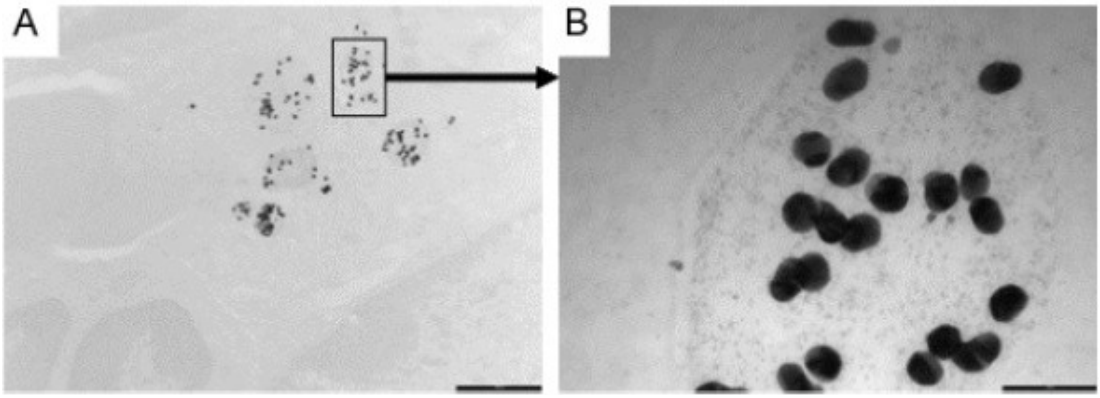

Figure 6-3 Accumulation of SERS nanoprobes in spleen tissue ((A) and (B)). Membrenes are observed around the SERS nanoprobes suggesting that the nanoprobes are uptaken by endosomes in the spleen cells.

Combined SERS and CT Contrast of SERS nanoprobe using Subcutaneous model

Combined *in vivo* SERS and CT contrast was studied in mice injected subcutaneously on the flank with 65.6±6.4 nm gold core size SERS nanoprobes (100ul, 12.5mg/ml) coded with DTTC iodide. Nude mice (N=3) were first fasted overnight and then sedated using 2% isofluorine anesthesia before injection. CT imaging of the mice and Raman spectroscopy detection was carried out pre and post injection. Raman spectroscopy was done using the 785 nm laser at 10mW power and 8s integration time. A large working distance microscope objective lens (10x 0.25NA) was used for focusing the laser and collection of the SERS signal. CT imaging was then carried out for a period of 6 min following Raman spectroscopy. Figure 6.4 are representative CT images and SERS spectra obtained from the mice. The location of the SERS nanoprobes was identifiable in the post injection CT images (Fig. 6.4 D) compared to the pre injection images (Fig. 6.4 C) as shown by the red arrows. The localization of SERS nanoprobes provided evidence of the *in vivo* CT contrast of the nanoprobes. The CT results were also complementary to Raman spectroscopy results (Fig 6.4 A and B). Raman spectrum of DTTC iodide was detected post injection in the region immediately surrounding the injection site and corresponding to the position identified in the CT images (Fig 6.4 B). However, Raman spectrum of DTTC iodide was noticeably absent in the pre-injected mice (Fig 6.4 A) and in the regions far from the injection site. Figure 6.4A was enhanced six times post processing for clearer observation of spectral features. The detection of SERS nanoprobes in the subcutaneous region offered proof the SERS signal is detectable under the nude mouse skin.

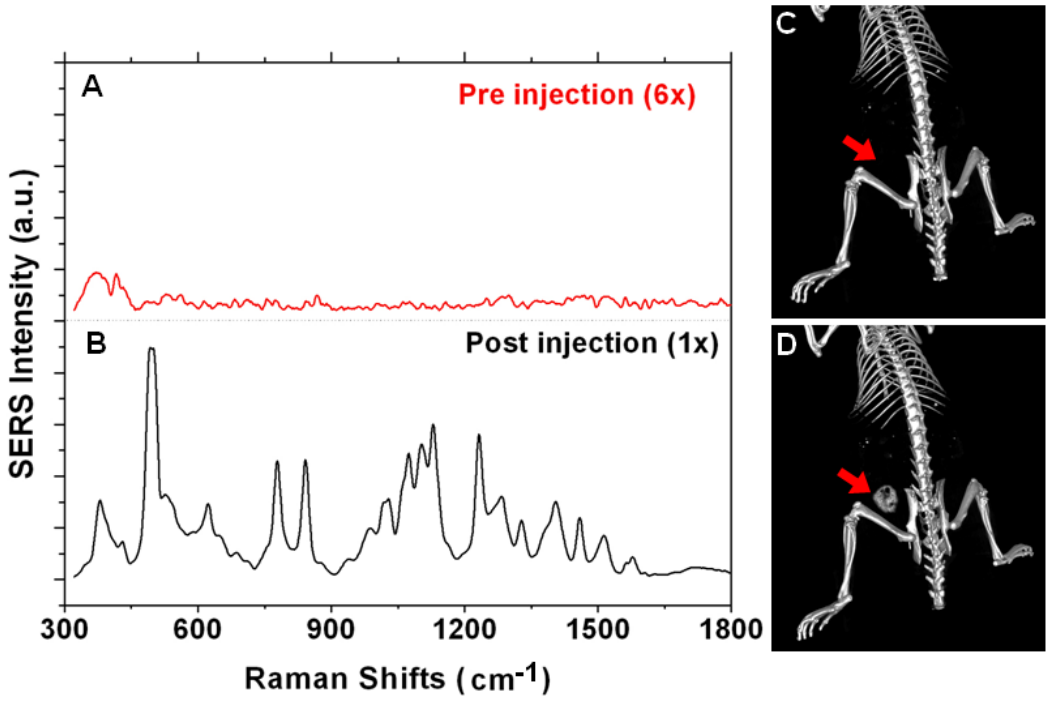

Figure 6-4 Combined Raman detection (A and B) and 3D CT imaging (C and D) of ~65 nm core DTTC encoded SERS nanoprobes subcutaneously injected a nude mouse. (A) and (C) are Raman spectrum and CT image respectively of the pre-injected mouse. (B) and (D) are Raman spectrum and CT image of post-injected mouse. The red arrows in panels C and D indicate the injection site. Raman signal of DTTC is revealed post injection and corresponds to the injection site in D where the CT contrast is generated by the SERS nanoprobes.

Combined SERS/CT imaging in orthotropic tumor model

Five mice were injected with 20k DAB2IP knockout PC-3 cells per injection orthotropically. Injection volume of 100 µl was used. After the injection of cells, the animals were monitored daily for 1 week before *in vivo* imaging studies were carried out. DTTC iodide coded SERS nanoprobes with nanoparticle core of 43.9 ± 3.8 nm were prepared for the study. For PET imaging 100 µL of 100 µCi FDG solution were administered intraveneously after an overnight fast. One hour later imaging was performed using the Siemens Inveon PET-CT Multimodality System. Once the tumor metastasis was clearly denoted using by PEG imaging, SERS nanoprobes (100 µl, 12.5 mg/ml) were injected intravenously via tail vein. CT scans were

carried out for 3 days post injection. After imaging was completed mice were sacrificed and tumor excised for SERS and TEM characterization.

Computed tomography (CT) images and FDG PET images overlaying the CT images in axial, coronal and sagittal planes anatomically identified tumor metastasis and the location at which SERS nanoprobes accumulated in the prostate (Fig. 6.5). The higher concentration of 18FDG in areas delineated by the red arrows as indicates higher metabolism consisted with tumor metastasis in both pre and post SERS nanoprobe injection. In the same region, post injection CT images show greater contrast than the prostate background. This increased contrast is absent in the pre injection images indicating that SERS nanoprobes were uptaken by the tumor. The uptake of non targeted SERS nanoprobes is thought to occur through the enhanced permeability and retention (EPR) effect[98, 99].

The mice were then sacrificed and the prostate was excised for TEM and Raman spectroscopy. Figure 6.6A was a slice of tumor tissue taken from mouse injected with SERS nanoprobes. The magnified image (Fig 6.6B) shows structures that were identified as the gold nanoparticle core of the SERS nanoprobes. The gold nanoparticles were observed to be largely monodispersed suggesting that the SERS nanoprobes remain stable *in vivo*. The scales for figure 5.6A and B are 1000nm and 100nm respectively. Interogation of the *ex vivo* tissue using Raman spectroscopy resulted in detection of the SERS signal (red line in figure 6.7) whose peaks corresponded with the peaks of the SERS nanoprobes in solution (green line) positively identifying the nanoparticles in the tissue to be DTTC iodide coded SERS nanoprobes. No such peaks were identified in the tumor tissue from mice which were not injected SERS nanoprobes (Fig. 6.7).

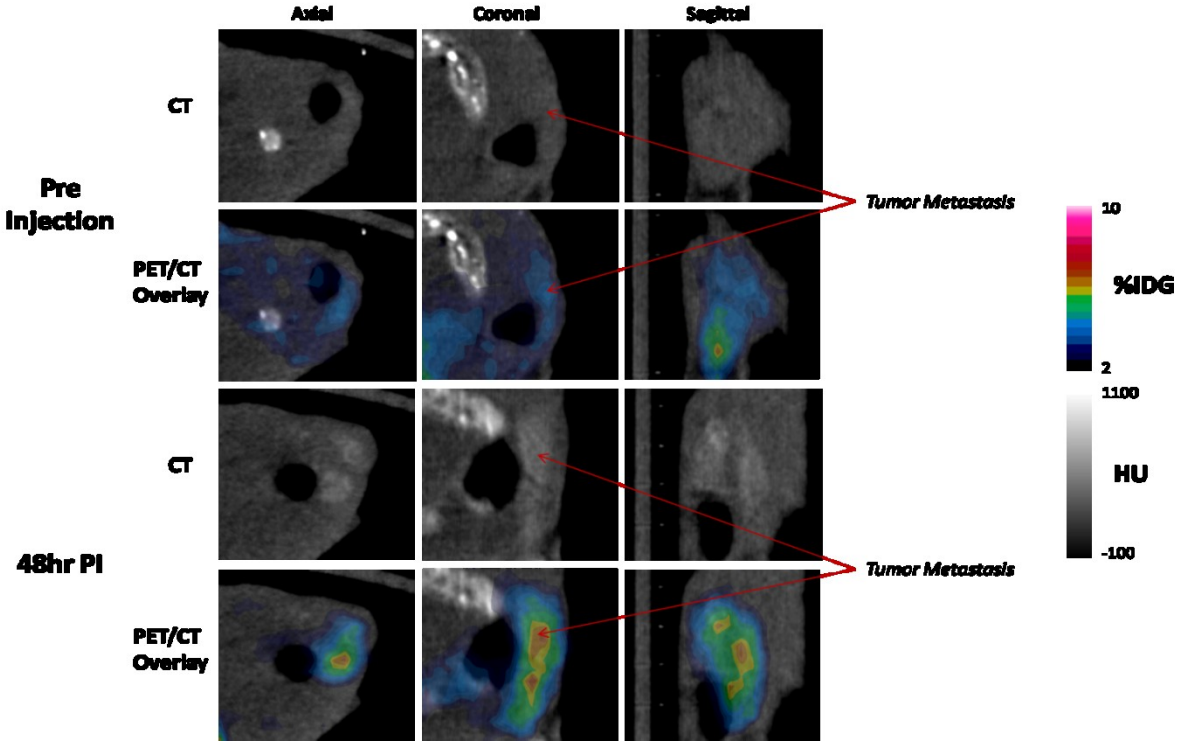

Figure 6-5 Axial, coronal and sagittal positron emission tomography images (PET) and computed tomography (CT) of prostate tumor metastasis is a nude mouse. Images were taken pre and 48h post injection with 100µl of 12.5mg/ml ~43 nm DTTC encoded SERS nanoprobes. PET contrast was achieved using 18FDG. CT units are expressed in Hounsfield Units (HU) and PET units are expressed in %ID/g. Tumor metastasis sites are indicated using the red arrows in the coronal view of the images. Control images taken pre injection reveal PET contrast at the tumor metastasis site but CT contrast greater than the prostate background is not visible. 48 h post injection PET/CT images reveal CT contrast at the tumor metastasis site that corresponds to the location of PET contrast indicating uptake of the SERS nanoprobes by the tumor.

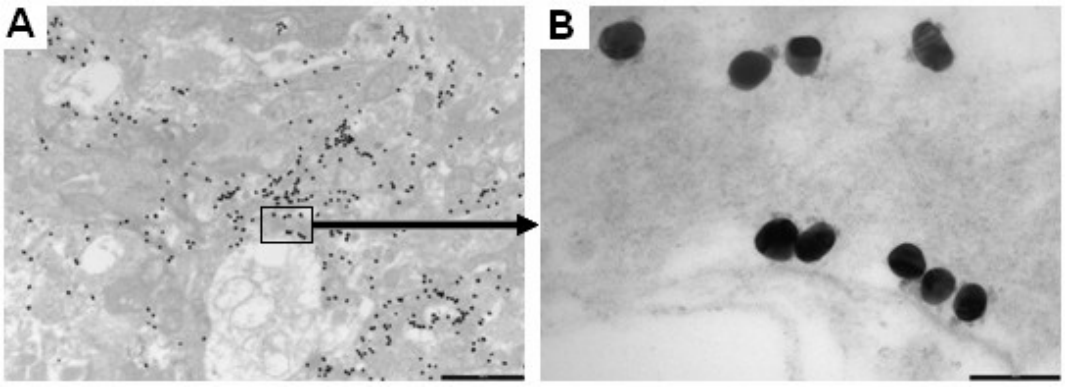

Figure 6-6 TEM images of *ex vivo* prostate tissue from tumor bearing mice. The scale bar in (A) and (B) are 1000nm and 100 nm respectively. Presence of SERS nanoprobes in the tumor tissue indicate that they are uptaken by the tumor. SERS nanoprobes were monodispersed indicating *in vivo* colloidal stability.

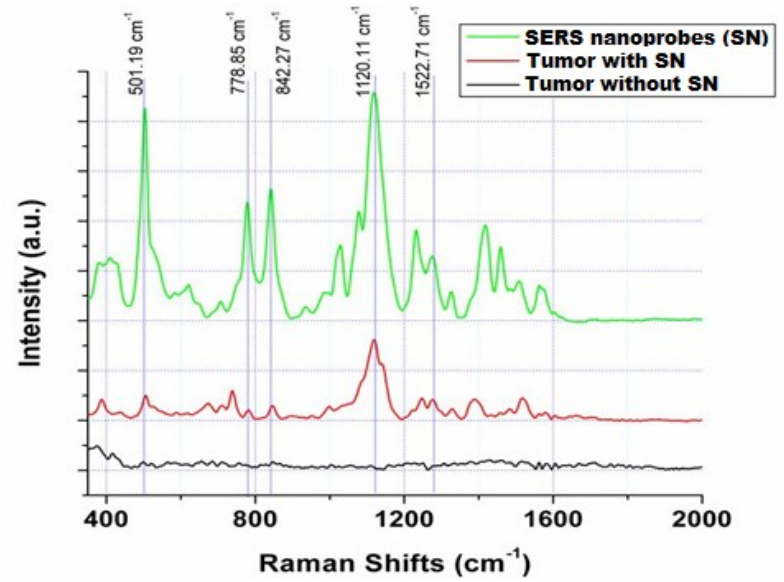

Figure 6-7 Raman spectra of DTTC encoded SERS nanoprobes (green), *ex vivo* prostate tissue of tumor bearing mouse injected with SERS nanoprobes (red) and *ex vivo* prostate tissue of tumor for tumor bearing with which was not injected with tissue (black). Raman spectra are plotted with an offset along the y-axis to depict the signals. More than five Raman peaks of the red colored spectrum match peaks from the SERS nanoprobes indicating presence of the SERS nanoprobes in the tumor tissue.

Conclusion

Dual contrast of SERS nanoprobes for SERS detection and CT imaging was demonstrated. 65.6±6.4 nm and 43.9±3.8 nm that have been shown to display large SERS enhancement also was demonstrated to display clinically sensitive CT contrast by comparing their X-ray attenuation to clinical used iodine based CT contrast agent. However the magnitude of dual contrast depends also on the amount of SERS nanoprobes that accumulate at the site of interest. Specific detection of lesions can be accomplished using immune-targeted gold nanoprobes [94, 95] and better biodistribution properties are usually associated with smaller gold nanoparticles. However, SERS enhancement factor also decreases with size of the gold nanoparticle. Therefore a further study into these particles would involve more fundamental studies of the mechanism of SERS to allow for increasing the SERS signal even as size of nanoprobe is reduced.

Transdermal uptake of SERS nanoprobes

Introduction

Several studies have shown of rigid nanoparticles has been reported [100-103]. Nanoparticles are applicable non-invasively as gels or in emulsions. In addition they possess large surface areas allowing for targeting and therapeutic agents to be attached to them. Nanoparticles have also displayed better pharmacokinetic properties compared to traditional diagnostic and therapeutic agents. SERS nanoprobes occupy a uniquely advantageous position with regards to transdermal delivery. The core of the nanoprobes possess unique electromagnetic qualities give them the potential to be used as therauptic agents in addition to the diagnostic potential results from their ability to enhance Raman signal.

The capacity of SERS nanoprobes transdermal delivery was investigated. Longitudinal studies were carried out in mice in which prostate cancer tumors had been implanted subcutaneously. The mice were treated using a targeted SERS nanoprobes conjugated with RGDγK peptide and pegyated SERS nanoprobes. Daily Raman spectroscopy monitoring

indicated accumulation of the SERS nanoprobes at the tumor site. SERS signal intensity indicated penetration of the SERS nanoprobes. Percutaneous penetration of the SERS nanoprobes was confirmed using ICP-MS measurements. ~0.39% and ~0.23% applied dose of nanoprobe per gram of tissue of targeted SERS nanoprobes and peglyated SERS nanoprobes respectively were detected. Further, specificity and clearance were studied using the same mouse tumor model in 6 new nude mice. The new set of mice were divided into two groups (test group and control group). The groups were treated with SERS nanoprobes conjugated with RGDγK peptide (targeted SERS nanoprobes) and SERS nanoprobes conjugated with anti-rabbit IgG (non-targeted SERS nanoprobes) respectively. Accumulation and clearance of SERS nanoprobes monitored using Raman spectroscopy was observed only in the test group suggesting preferential uptake of the targeted SERS nanoprobes.

SERS Nanoprobes for in vivo study

Targeted and non-targeted SERS nanoprobes were synthesized using 65.6±6.4 nm gold nanoparticles and encoded using HITC iodide. Targeted nanoprobes were conjugated with commercially obtained HS-PEG-cyclic(RGDγK) peptide. The RGDγK peptide has a thiol group allowing for thiol gold chemistry to be used in the conjugation. Briefly, after encoding with HITC iodide, 100µl of 100µg/ml of RGDγK peptide was added to rapidly stirring gold nanoparticles (~1.1 x 10^{10}/ml) for 1h at room temperature followed by peglyation. SERS nanoprobes were then purified by centrifugation and concentrated to form a pellet. 1.32 x 10^{11} SERS nanoprobes prepared in this way were then resuspended in 5mg of IcyHot™ gel. Therefore the 5 mg SERS nanoprobe gel was composed of 0.167ug of SERS nanoprobes (1.32 x 1011 nanoprobes) and 4.833 mg of Icy-Hot™ gel. PEGlyated SERS nanoprobes with no ligand but prepared in similar proportions to the targeted SERS nanoprobes were used as control. A second control was plain IcyHot™ gel.

In vivo Xenograph Model

PC-3 cells were cultured in T-media supplemented with 5% fetal bovine serum (FBS) and 1x Penicillin/Streptomycin. RGDγK peptide conjugated to the targeted SERS nanoprobes are specific to $\alpha_V\beta_3$ integrins expressed by PC-3 cells[104]. Cultured cells were harvested using PBS and trypsin/EDTA and suspended in T-media before mixing with Matrigel^{TM}. Three 6-8 week old nude mice were injected with the cell suspension (100ul of 2.5 x 10^6 cells per injection) on each shoulder. After cell injection the mice were monitored every second day. The tumor was allowed to grow for three weeks until palpable (3 – 5 mm) before imaging study was began. Figure 6.8 A and B is a picture and an axial CT image of the mouse after tumor had grown. A tumor is observed on both the shoulders of the mouse in both images.

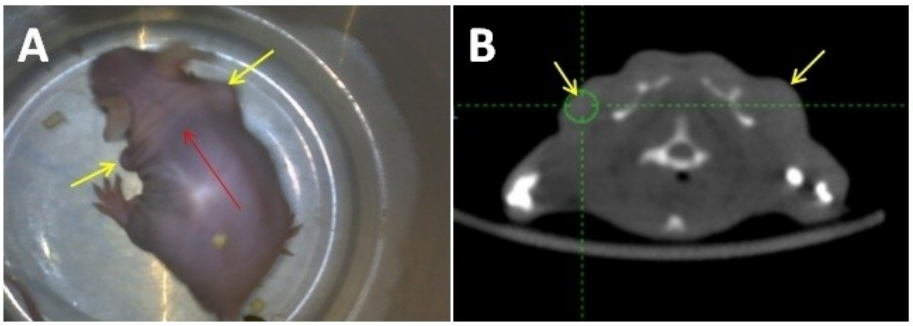

Figure 6-8(A) Picture of pre-injection Xenograph tumor model mouse and (B) axial view of the mouse showing locations in which subcuteneous tumors were induced. Yellow arrows indicate the tumor locations and the red arrow indicates possible tumor injection site. Tumor were induced by injecting 2.5x10^6 PC-3 prostate cancer cell lines subcuteneous each shoulder of eight mice

Topical application and SERS signal monitoring

The mice were anestherized using 3% isofluorene at room temperature. Once sedated the tumor sites of each mouse was washed gently but thoroughly using a mild surfactant solution and rinsed with water. Raman spectroscopy was used to monitor the surface and subcutaneous region of each tumor. Monitoring was done using 785 nm Raman module with a 10x 0.25NA objective with a resolution of ~1.5 μm and spot size of ~ 3.6 μm. While still

sedated each mouse was treated with 5 mg of SERS nanoprobe gel applied by gentle over a ~1 cm^2 area at each tumor site providing a final dose of ~5mg/cm^2 per tumor site. The application was dried to minimize smearing before mice were allowed to wake up. The three different applications of SERS nanoprobe gels were applied to the three different mice respectively. Application was done daily over a 7 day period after which the mice were sacrificed and tissue removed for evaluation using ICP-MS.

Figure 6.9 shows the Raman spectra for days 1, 2, 4 and 6 acquired from the tumor site of the mouse on which targeted SERS nanoprobes. The signal labeled control was acquired from mouse on which only gel was applied. Raman spectra for day 1 and 2 are similar to the control signal however at day 4 the DTTC iodide Raman signature was detected and the signal continued to be detected until day 7. Detection of the DTTC iodide spectrum suggested accumulation of SERS nanoprobes at the tumor site. However, because of the thorough cleaning and the absence of such a signal in the mouse with untargeted SERS nanoprobes the SERS spectrum was attributed to accumulation of the SERS nanoprobes in layer of the skin just under the surface or deeper. Suggesting penetration of the stratum corneum.

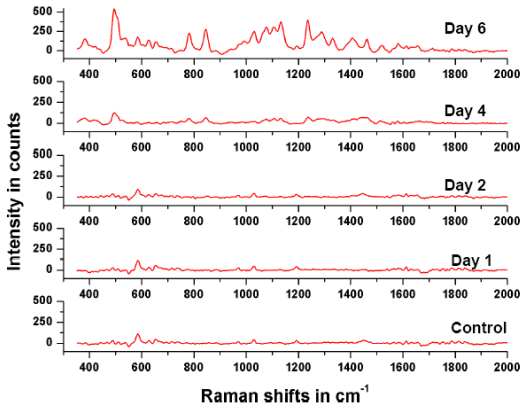

Figure 6-9 Raman spectra for DTTC signal obtained from tumor on which targeted SERS nanoprobes were applied. Raman spectroscopy measurements are taken 24h post application for seven days after thorough wash of the application area. DTTC signal was clearly detectable on day four and continues to be observed up to day 6.

Samples of the liver, spleen, tumor and skin were extracted from each of the mice. The extracted tissues were weight and dissolved in aqua regia before being measured using ICP-MS for amount of SERS nanoprobes. The mass of applied SERS nanoprobes was also verified using ICP-MS and percentage applied dose of nanoprobe per gram of tissue calculated using equation 6.1.

$$\%\ Applied\ dose\ of nanoprobe/g = \frac{mass\ of\ nanoprobes\ \ measured\ /mass\ of\ tissue}{mass\ of\ applied\ \ nanoprobes} \times 100\% \text{.....6.1}$$

The largest amounts of nanoprobes are collected in the skin (~0.42%) compared to the spleen (~0.13%) and tumor (0.06%) (Fig. 6.10). However, since the surface of the skin was washed thoroughly, the SERS nanoprobes were likely trapped in the layers of the epidermis of the mouse skin. This result was similar to a number of studies into percutenous penetration of nanoparticles into skin. A significant amount of the SERS nanoprobes are however detected in the spleen and in the tumor suggesting that some of the nanoparticles penetrated into the systemic regions of the body. Preference for targered nanoprobe over the non-targered nanoprobe was also noted.

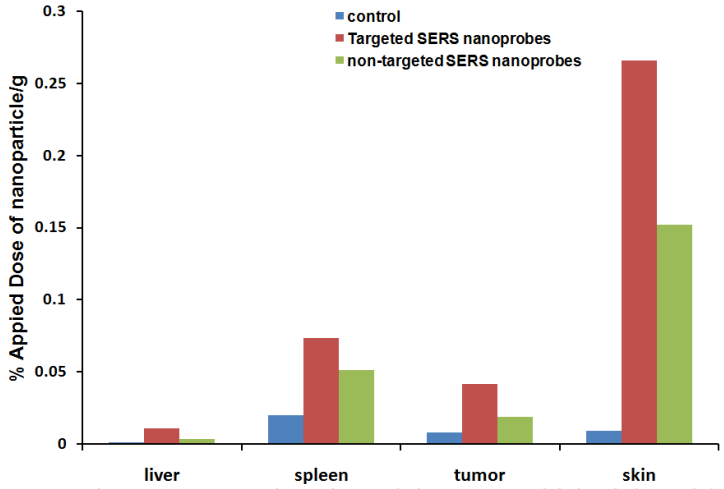

Figure 6-10 Percentage dose per organ in selected tissue on which plain gel (control), targeted nanoprobes and non targeted nanoprobes are applied. The nanoprobes were all dispersed in gel prior to application. The largest amount of dose was detected on the skin indicating that most of the nanoprobes remained trapped in the layers of the skin. Amount detected in spleen

and tumor suggests transdermal delivery of nanoprobes. Preference for targeted delivery is noted by the slightly greater dose of targeted nanoprobes in the organs investigated.

The Raman spectroscopy result as well as the ICP-MS result suggested that the SERS nanoprobes accumulate at the tissue over time. Once the concentration of SERS nanoprobes were within the dynamic range the signal were detectable. A dynamic process of accumulation further suggests that clearance might occur. Knowledge about the dynamics of clearance is important in designing application frequency]. Therefore, a further study was conducted to determine whether the nanoprobes were usable in detecting clearance in live animals.

Accumulation and Clearance of SERS nanoprobes during Transdermal delivery

A new batch of targeted and non-targeted SERS nanoprobes were synthesized using 65.6±6.4 nm gold nanoparticles and encoded using HITC iodide. 5 mg Targeted SERS nanoprobe gel composed of 0.167ug of SERS nanoprobes (1.32×10^{11} nanoprobes) and 4.833 mg of Icy-Hot^{TM} gel was prepared. Non-targeted SERS nanoprobe gel was also similarly prepared with the exception that anti-IgG antibody (Sigma-aldrich, R113) conjugated to a linker molecule (Hydrazide-PEG-dithiol) was used to functionalize the SERS nanoprobes in place of the RGDγK peptide. Introduction of a non-specific ligand on the non-targeted SERS nanoprobes was introduced to mimic the case where several nanoprobes with different SERS nanoprobes may be used to detect different targets.

Six 6-8 week old nude mice were injected with the cell suspension (100ul of 2.5×10^6 cells per injection) on each shoulder. After cell injection the mice were monitored every second day. The tumor was allowed to grow for three weeks until palpable (3 – 5 mm) before imaging study was began. The mice were divided into two groups of three mice each: test group and control group. Targeted SERS nanoprobes were applied to the test group mice while the non-targeted SERS nanoprobes were applied to the control group mice. Application of SERS nanoprobes was done daily on sedated mice at room temperature. Monitoring of the SERS

signal using Raman spectroscopy was also done 24h post application after gentle but thorough washing of the skin surface at the tumor site.

Figure 6.11 shows a series of SERS signals tracking accumulation of the applied SERS nanoprobes over 7 days. The SERS signals were representative signals obtained from the tumor site of a randomly selected mouse in the test group (Fig. 6.11 A) and the control group (Fig. 6.11 B). Accumulation over seven day for the 6 mice was tracked by plotting the intensity of 554.58 cm^{-1} vibrational mode from HITC iodide encoded SERS nanoprobes. The SERS intensity of the test group show an increase in intensity starting from the fourth day while the SERS intensity of the control group remains constant through the seven days (Fig. 6.12). This suggests accumulation of the SERS nanoprobes over time. The wide signal variation of the SERS nanoprobes was due to the uniform accumulation from mouse to mouse as well as from point to point in the area interrogated and not as a result of signal variation from the SERS nanoprobes themselves.

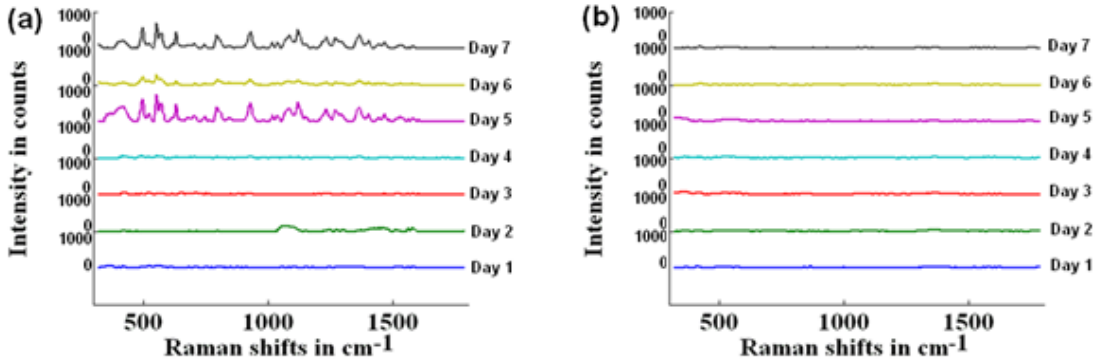

Figure 6-11 Raman spectroscopy measurements obtained from mouse tumor in the (A) test group and the (B)control group. The signals are obtained a randomly chosen mouse in each of the groups and have been processed post acquisition to remove the background in order to allow for peak intensity comparison. The signal of HITC iodide which was the encoding Raman reporter, began to be visible at day 4 – 5 of monitoring in test mice and remained detectable through day 10. The results show the first seven days.

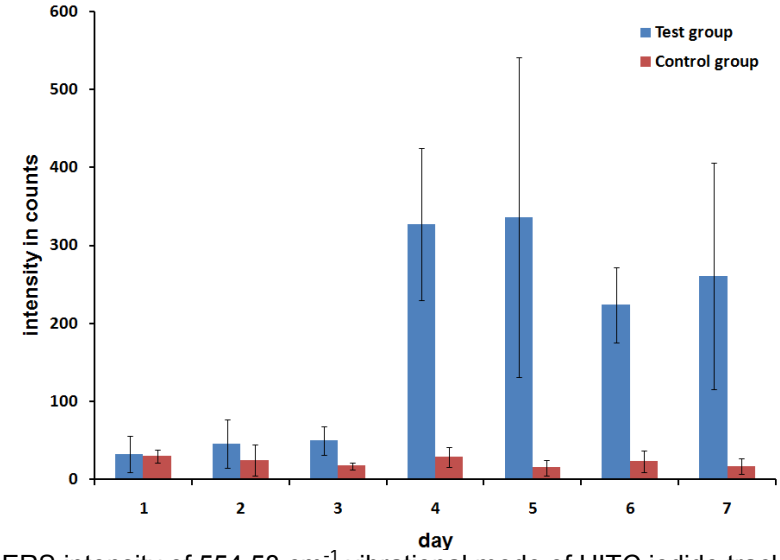

Figure 6-12 SERS intensity of 554.58 cm^{-1} vibrational mode of HITC iodide tracked over seven days for test and control group mice (n=6 for each group). SERS intensity was measured everyday 24h post application of SERS nanoprobe gel and after washing with mild surfactant. SERS signal was detected after day 3. Large variation in signal intensity was likely due to non-uniform accumulation of SERS nanoprobes over the area of application.

Treatment of the mice with SERS nanoprobe gel was continued to day 10 during which the last treatment was applied. SERS intensity was then monitored 24h and 48h post application (Fig.6.13 and Fig 6.14). SERS signal in the test group was detectable 24h post application (day 11) but at the 48h time point (day 12) the signal intensity dropped to background levels of the system. However, in the control group no significant signal was observed all time points. The drop of signal in the test group suggests clearance of the SERS nanoprobes from the tumor site. It is noteworthy that the drop of the signal between day 11 and day 12 was sudden mirroring the sudden jump of the signal between day 3 and 4 of SERS nanoprobe accumulation.

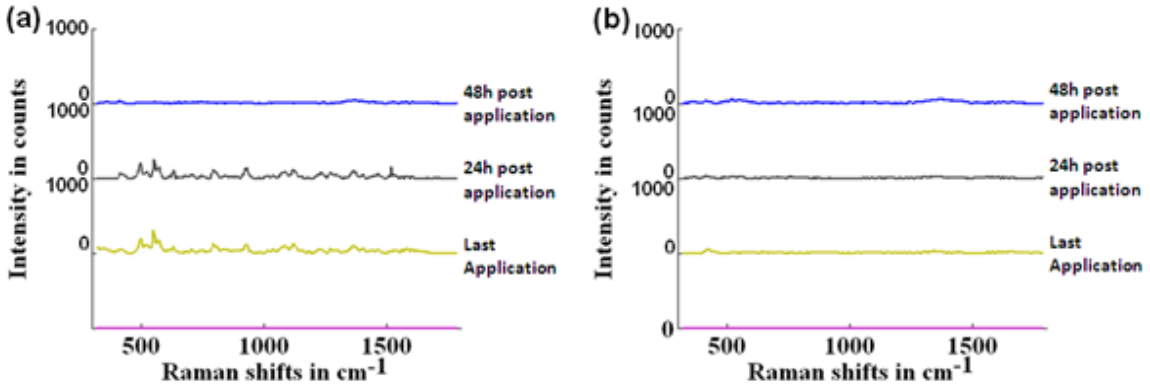

Figure 6-13. Raman spectroscopy measurements obtained from mouse tumor in the test group (A) and the control group (B) to determine clearance of the nanoprobes. Signals are obtained for the last day of application, 24h and 48h post application. The signal of HITC iodide was visible 24h post application but was not detectable 48h post application.

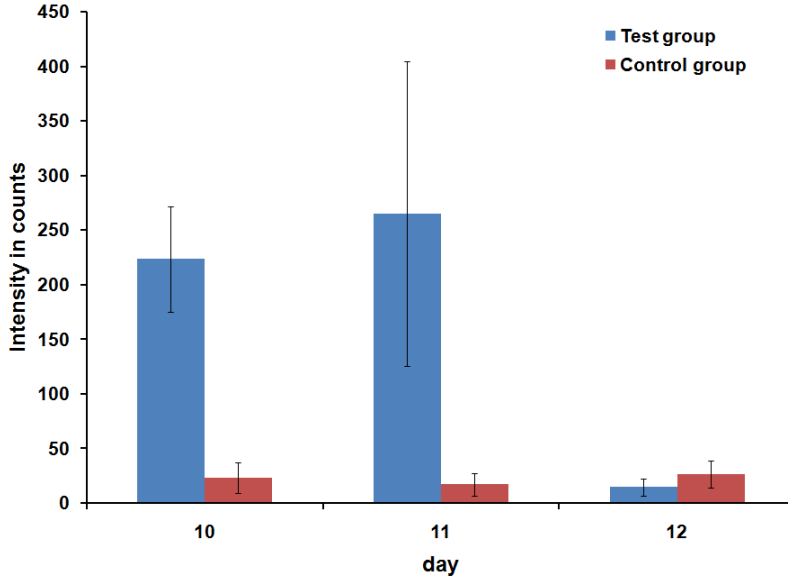

Figure 6-14

Figure 6. 1 SERS intensity of 554.58 cm^{-1} vibrational mode of HITC iodide tracked over three days for test and control group mice (n=6 for each group). Day 10 was the final day of application for SERS nanoprobes. Intensity of SERS nanoprobes was observable 24h post application but diminishes to background levels 48h post application.

Conclusion

Selective accumulation of targeted transdermally delivered SERS nanoprobes in subcutaneous tumors was demonstrated in two longitudinal studies. In the first study, accumulation of SERS nanoprobes in the tumor is monitored using Raman spectroscopy and confirmed using ICP-MS. While in the second study, the SERS nanoprobes accumulation and clearance of SERS nanoprobes was monitoring. Targeted SERS nanoprobes were observed to selectively accumulate at the tumor sites. The results further indicated that ~0.4% of the applied dose penetrated the outer layers of the skin after 7 days of application. 75% of these SERS nanoprobes remain in the skin while the rest were systemically delivered. The process of delivery was shown to be dynamic simultaneously involving accumulation and clearance at the tumor site.

Summary

In this chapter (i) multimodality SERS/CT cancer detection using SERS nanoprobes and (ii) subcutaneous cancer detection via transdermally delivered SERS nanoprobes are demonstrated. Multimodality SERS/CT nanoprobes were demonstrated in orthotropic prostate tumor mouse model. Regions of tumor metastasis delineated using PET imaging also displayed greater CT contrast and SERS spectroscopy of excised tissue confirmed presence of SERS nanoprobes. Further developments of SERS nanoprobes specifically reducing the size of the nanoparticle while maintaining or increasing the SERS signal would improve SERS nanoprobes pharmacokinetic properties. Detection of subcutaneous cancer via transdermal delivery was demonstrated in nude mice using prostate tumor model. The targeted SERS nanoprobes displayed selective attachment to the tumor site. Experiment provided evidence that attachment of SERS nanoprobes was a dynamic process involving accumulation and clearance. Further studies into the dynamics of attachment would improve the dose and frequency required for optimal detection. Additionally, delivery of the SERS nanoprobes can be improved by investigation into the effect of the delivery vehicle.

Chapter 7

Conclusion

The main objective of this research was the development of multiple-color dual modality SERS/CT nanoprobes for cancer diagnosis. The motivation for the research was the opportunity presented by the increase in discovery and elucidation of cancer biomarkers whose detection has the potential of improving cancer diagnosis, treatment and monitoring. In chapter one the opportunities presented this progress in biomarker discovery was discussed and the potential of SERS nanoprobes to significantly impact cancer diagnosis is introduced.

In chapter 2 the use of SERS nanoprobes as contrast agents for biomedical applications was briefly reviewed. The advantage presented by SERS nanoprobes for multiplexing was discussed as well as their potential as contrast agents for CT. Focus was placed on the Raman scattering and SERS mechanism in order to understand the design of both the Raman instrumentation and SERS nanoprobes. The Raman modular instrument, which was design and fabricated to allow for in vivo and in vitro measurement was then described.

In chapter three, SERS nanoprobes were described. The SERS nanoprobes consist of gold nanoparticle core, encoded using a Raman reporter and coated with methyl capped thiol-terminated polyethylene glycol for steric stability. The design combines two aspects of SERS nanoprobes design: the encoding of nanoparticles using Raman active molecules and directional conjugation of ligands to nanoparticles to functionalized SERS nanoprobes. Eleven colors of SERS nanoprobes with a gold nanoparticle core size of 65.6 ± 6.4 nm were synthesized. Five of the eleven were selected based on their intensities for *in vitro* and *in vivo* evaluation.

The method developed for quantitative analysis of multiplexed SERS nanoprobes colors was described in chapter four. The method named Eigenspectra algorithm is based on principle component analysis and does not rely on source spectra but calibration is

accomplished using actual mixture signals and therefore in not affected by potential non-linear relationship between intensity and concentration. The algorithm was tested using two-plex mixture of two SERS nanoprobes and its capacity to determine the individual colors mixed and their concentration was demonstrated.

In chapter four, SERS nanoprobes evaluated for *in vitro* applications. Using two separate cell lines specific targeting of cell surface expression using SERS nanoprobes was demonstrated. Prostate specific membrane antigen was detected using Anti-PSMA antibody functionalized SERS nanoprobes in C4-2 cell lines, while epidermal growth factor receptors (EGFr) was detected using anti-EGFr targeted SERS nanoprobes in U87-MG cell lines. Simultaneous detection of four colors of SERS nanoprobes was demonstrated in glioblastoma multiforme (U87 MG) cell lines targeted with four-plex mixture SERS nanoprobes. The *in vitro* cells studies not only evaluated the SERs nanoprobes for *in vitro* applications but were also an important step in determining if the SERS nanoprobes could be tested in a mouse model.

Evaluation of SERS nanoprobes was then demonstrated for two *in vivo* applications (i) multimodality SERS/CT cancer detection using SERS nanoprobes and (ii) subcutaneous cancer detection via transdermally delivered SERS nanoprobes. Multimodality SERS/CT nanoprobes were demonstrated in orthotropic prostate tumor mouse model. Regions of tumor metastasis delineated using PET imaging also displayed greater CT contrast and SERS spectroscopy of excised tissue confirmed presence of SERS nanoprobes. Detection of subcutaneous cancer via transdermal delivery was demonstrated in nude mice using prostate tumor model. Targeted SERs nanoprobes selectively attach to the tumor site over a period of time suggesting the importance of dose as well as frequency of application. When treatment was stopped the SERs signal decays over time.

References

1. P. Maruvada, W. Wang, P. D. Wagner, and S. Srivastava, "Biomarkers in molecular medicine: cancer detection and diagnosis," Biotechniques **Suppl**, 9-15 (2005).
2. K. M. W. S. E. P. Partin Aw, and et al., "Combination of prostate-specific antigen, clinical stage, and gleason score to predict pathological stage of localized prostate cancer: A multi-institutional update," JAMA: The Journal of the American Medical Association **277**, 1445-1451 (1997).
3. T. A. Stamey, N. Yang, A. R. Hay, J. E. McNeal, F. S. Freiha, and E. Redwine, "Prostate-Specific Antigen as a Serum Marker for Adenocarcinoma of the Prostate," New England Journal of Medicine **317**, 909-916 (1987).
4. F. Nomura, K. Ohnishi, and Y. Tanabe, "Clinical features and prognosis of hepatocellular carcinoma with reference to serum alpha-fetoprotein levels. Analysis of 606 patients," Cancer **64**, 1700-1707 (1989).
5. T. Komeda, Y. Fukuda, T. Sando, R. Kita, M. Furukawa, N. Nishida, M. Amenomori, and A. K. Nakao, "Sensitive detection of circulating hepatocellular carcinoma cells in peripheral venous blood," Cancer **75**, 2214-2219 (1995).
6. H. Halila, U.-H. Stenman, and M. Seppälä, "Ovarian cancer antigen CA 125 levels in pelvic inflammatory disease and pregnancy," Cancer **57**, 1327-1329 (1986).
7. A. N. Bhatt, R. Mathur, A. Farooque, A. Verma, and B. S. Dwarakanath, "Cancer biomarkers - current perspectives," Indian J Med Res **132**, 129-149 (2010).
8. M. Polanski, and N. L. Anderson, "A List of Candidate Cancer Biomarkers for Targeted Proteomics," Biomarker Insights **2**, 1-48 (2006).
9. N. Rifai, M. A. Gillette, and S. A. Carr, "Protein biomarker discovery and validation: the long and uncertain path to clinical utility," Nat Biotech **24**, 971-983 (2006).
10. T. Vo-Dinh, F. Yan, and M. B. Wabuyele, "Surface-enhanced Raman scattering for medical diagnostics and biological imaging," Journal of Raman Spectroscopy **36**, 640-647 (2005).
11. X. Michalet, F. F. Pinaud, L. A. Bentolila, J. M. Tsay, S. Doose, J. J. Li, G. Sundaresan, A. M. Wu, S. S. Gambhir, and S. Weiss, "Quantum Dots for Live Cells, in Vivo Imaging, and Diagnostics," Science **307**, 538-544 (2005).
12. S. Abalde-Cela, P. Aldeanueva-Potel, C. Mateo-Mateo, L. Rodríguez-Lorenzo, R. A. Alvarez-Puebla, and L. M. Liz-Marzán, "Surface-enhanced Raman scattering biomedical applications of plasmonic colloidal particles," Journal of The Royal Society Interface **7**, S435-S450 (2011).
13. Y. C. Cao, R. Jin, and C. A. Mirkin, "Nanoparticles with Raman Spectroscopic Fingerprints for DNA and RNA Detection," Science **297**, 1536-1540 (2002).
14. M. Culha, D. Stokes, L. R. Allain, and T. Vo-Dinh, "Surface-Enhanced Raman Scattering Substrate Based on a Self-Assembled Monolayer for Use in Gene Diagnostics," Analytical Chemistry **75**, 6196-6201 (2003).

15. K. Faulds, W. E. Smith, and D. Graham, "Evaluation of Surface-Enhanced Resonance Raman Scattering for Quantitative DNA Analysis," Analytical Chemistry **76**, 412-417 (2003).
16. K. Katrin, and et al., "Surface-enhanced Raman scattering and biophysics," Journal of Physics: Condensed Matter **14**, R597 (2002).
17. K. A. Willets, "Surface-enhanced Raman scattering (SERS) for probing internal cellular structure and dynamics," Analytical and Bioanalytical Chemistry **394**, 9 (2009).
18. S. Keren, C. Zavaleta, Z. Cheng, A. de la Zerda, O. Gheysens, and S. S. Gambhir, "Noninvasive molecular imaging of small living subjects using Raman spectroscopy," Proceedings of the National Academy of Sciences **105**, 5844-5849 (2008).
19. X. M. Qian, and S. M. Nie, "Single-molecule and single-nanoparticle SERS: from fundamental mechanisms to biomedical applications," Chemical Society reviews **37**, 912-920 (2008).
20. M. Xiao, J. Nyagilo, V. Arora, P. Kulkarni, D. Xu, X. Sun, and D. P. Dave, "Gold nanotags for combined multi-colored Raman spectroscopy and x-ray computed tomography," Nanotechnology **21**, 035101 (2009).
21. S. Sebastian, "SERS Microscopy: Nanoparticle Probes and Biomedical Applications," ChemPhysChem **10**, 1344-1354 (2009).
22. E. C. L. Ru, and P. G. Etchegoin, *Principles of Surface-Enhanced Spectroscopy and related plasmonic effects* (Elsevier, Amsterdam, 2009).
23. K. C. Bantz, A. F. Meyer, N. J. Wittenberg, H. Im, O. Kurtulus, S. H. Lee, N. C. Lindquist, S.-H. Oh, and C. L. Haynes, "Recent progress in SERS biosensing," Physical Chemistry Chemical Physics **13**, 11551-11567 (2011).
24. E. Boisselier, and D. Astruc, "Gold nanoparticles in nanomedicine: preparations, imaging, diagnostics, therapies and toxicity," Chemical Society reviews **38**, 1759-1782 (2009).
25. W. Page Faulk, and G. Malcolm Taylor, "Communication to the editors: An immunocolloid method for the electron microscope," Immunochemistry **8**, 1081-1083 (1971).
26. C. V. Raman, and K. S. Krishnan, "A New Type of Secondary Radiation," Nature **121**, 501-502 (1928).
27. S.-L. Zhang, "Raman Spectroscopy and its Application in Nanostructures," J. W. S. Ltd, ed. (2012).
28. P. Kambhampati, M. C. Foster, and A. Campion, "Two-dimensional localization of adsorbate/substrate charge-transfer excited states of molecules adsorbed on metal surfaces," The Journal of Chemical Physics **110**, 551-558 (1999).
29. G. C. Schatz, and R. P. Van Duyne, "Electromagnetic Mechanism of Surface-Enhanced Spectroscopy," in *Handbook of Vibrational Spectroscopy*(John Wiley & Sons, Ltd, 2006).
30. P. L. Stiles, J. A. Dieringer, N. C. Shah, and R. P. Van Duyne, "Surface-Enhanced Raman Spectroscopy," Annual Review of Analytical Chemistry **1**, 601-626 (2008).

31. L. L. Zhao, L. Jensen, and G. C. Schatz, "Surface-Enhanced Raman Scattering of Pyrazine at the Junction between Two Ag20 Nanoclusters," Nano Letters **6**, 1229-1234 (2006).
32. W. E. Doering, M. E. Piotti, M. J. Natan, and R. G. Freeman, "SERS as a Foundation for Nanoscale, Optically Detected Biological Labels," Advanced Materials **19**, 3100-3108 (2007).
33. R. A. Alvarez-Puebla, and L. M. Liz-Marzán, "SERS-Based Diagnosis and Biodetection," Small **6**, 604-610 (2010).
34. R. F. Aroca, R. A. Alvarez-Puebla, N. Pieczonka, S. Sanchez-Cortez, and J. V. Garcia-Ramos, "Surface-enhanced Raman scattering on colloidal nanostructures," Advances in Colloid and Interface Science **116**, 45-61 (2005).
35. E. Pavel I Fau - McCarney, A. McCarney E Fau - Elkhaled, A. Elkhaled A Fau - Morrill, K. Morrill A Fau - Plaxco, M. Plaxco K Fau - Moskovits, and M. Moskovits, "Label-Free SERS Detection of Small Proteins Modified to Act as Bifunctional Linkers," (2008).
36. L. Guerrini, I. Izquierdo-Lorenzo, J. V. Garcia-Ramos, C. Domingo, and S. Sanchez-Cortes, "Self-assembly of [small alpha],[small omega]-aliphatic diamines on Ag nanoparticles as an effective localized surface plasmon nanosensor based in interparticle hot spots," Physical Chemistry Chemical Physics **11**, 7363-7371 (2009).
37. B. D. Moore, L. Stevenson, A. Watt, S. Flitsch, N. J. Turner, C. Cassidy, and D. Graham, "Rapid and ultra-sensitive determination of enzyme activities using surface-enhanced resonance Raman scattering," Nat Biotech **22**, 1133-1138 (2004).
38. G. Lajos, D. Jancura, P. Miskovsky, J. V. GarciÌ□a-Ramos, and S. Sanchez-Cortes, "Surface-Enhanced Fluorescence and Raman Scattering Study of Antitumoral Drug Hypericin: An Effect of Aggregation and Self-Spacing Depending on pH," The Journal of Physical Chemistry C **112**, 12974-12980 (2008).
39. B. Lutz, C. Dentinger, L. Sun, L. Nguyen, J. Zhang, A. J. Chmura, A. Allen, S. Chan, and B. Knudsen, "Raman Nanoparticle Probes for Antibody-based Protein Detection in Tissues," J. Histochem. Cytochem. **56**, 371-379 (2008).
40. J. P. Nolan, E. Duggan, E. Liu, D. Condello, I. Dave, and S. A. Stoner, "Single Cell Analysis Using Surface Enhanced Raman Scattering (SERS) Tags," Methods (2012).
41. X. Qian, X. H. Peng, D. O. Ansari, Q. Yin-Goen, G. Z. Chen, D. M. Shin, L. Yang, A. N. Young, M. D. Wang, and S. Nie, "In vivo tumor targeting and spectroscopic detection with surface-enhanced Raman nanoparticle tags," Nature biotechnology **26**, 83-90 (2008).
42. X. Qian, X. Zhou, and S. Nie, "Surface-Enhanced Raman Nanoparticle Beacons Based on Bioconjugated Gold Nanocrystals and Long Range Plasmonic Coupling," Journal of the American Chemical Society **130**, 14934-14935 (2008).
43. R. G. Freeman, W. E. Doering, I. D. Walton, S. G. Penn, G. Davis, F. Wong, and M. J. Natan, "Detection of biomolecules using nanoparticle surface enhanced Raman scattering tags," 114-122 (2005).

44. A. Guerrero-Martínez, J. Pérez-Juste, and L. M. Liz-Marzán, "Recent Progress on Silica Coating of Nanoparticles and Related Nanomaterials," Advanced Materials **22**, 1182-1195 (2010).
45. J. Ni, R. J. Lipert, G. B. Dawson, and M. D. Porter, "Immunoassay Readout Method Using Extrinsic Raman Labels Adsorbed on Immunogold Colloids," Analytical Chemistry **71**, 4903-4908 (1999).
46. T. Rohr Te Fau - Cotton, N. Cotton T Fau - Fan, P. J. Fan N Fau - Tarcha, and P. J. Tarcha, "Immunoassay employing surface-enhanced Raman spectroscopy," (1989).
47. S. Kumar, J. Aaron, and K. Sokolov, "Directional conjugation of antibodies to nanoparticles for synthesis of multiplexed optical contrast agents with both delivery and targeting moieties," Nat. Protocols **3**, 314-320 (2008).
48. G. Frens, "Controlled nucleation for the regulation of the particle size in monodisperse gold suspensions," Nature (London), Physical Science **241**, 3 (1973).
49. J. Turkevich, "Colloidal gold. Part I," Gold Bulletin **18**, 86-91 (1985).
50. L. Jiali Niu and Tao Zhu and Zhongfan, "One-step seed-mediated growth of 30â€“150Â nm quasispherical gold nanoparticles with 2-mercaptosuccinic acid as a new reducing agent," Nanotechnology **18**, 325607 (2007).
51. E. C. Le Ru, E. Blackie, M. Meyer, and P. G. Etchegoin, "Surface Enhanced Raman Scattering Enhancement Factors: A Comprehensive Study," The Journal of Physical Chemistry C **111**, 13794-13803 (2007).
52. B. R. Lutz, C. E. Dentinger, L. N. Nguyen, L. Sun, J. Zhang, A. N. Allen, S. Chan, and B. S. Knudsen, "Spectral Analysis of Multiplex Raman Probe Signatures," ACS nano **2**, 2306-2314 (2008).
53. J. Nyagilo, M. Xiao, X. Sun, and D. P. Dave, "Multi-color raman nanotags for tumor cell biomarker detection," Conf Proc IEEE Eng Med Biol Soc **1**, 6314-6317 (2009).
54. L. Sun, K.-B. Sung, C. Dentinger, B. Lutz, L. Nguyen, J. Zhang, H. Qin, M. Yamakawa, M. Cao, Y. Lu, A. J. Chmura, J. Zhu, X. Su, A. A. Berlin, S. Chan, and B. Knudsen, "Composite Organic-Inorganic Nanoparticles as Raman Labels for Tissue Analysis," Nano Letters **7**, 351-356 (2007).
55. X. Huang, and M. A. El-Sayed, "Gold nanoparticles: Optical properties and implementations in cancer diagnosis and photothermal therapy," Journal of Advanced Research **1**, 13-28 (2010).
56. C. M. Galloway, E. C. Le Ru, and P. G. Etchegoin, "An Iterative Algorithm for Background Removal in Spectroscopy by Wavelet Transforms," Applied Spectroscopy **63**, 1370-1376 (2009).
57. R.-Q. Liang, C.-Y. Tan, and K.-C. Ruan, "Colorimetric detection of protein microarrays based on nanogold probe coupled with silver enhancement," Journal of Immunological Methods **285**, 157-163 (2004).
58. W. F. Patton, "Detection technologies in proteome analysis," Journal of Chromatography B **771**, 3-31 (2002).
59. I. Notingher, G. Jell, P. L. Notingher, I. Bisson, O. Tsigkou, J. M. Polak, M. M. Stevens, and L. L. Hench, "Multivariate analysis of Raman spectra for in vitro non-

invasive studies of living cells," Journal of Molecular Structure **744-747**, 179-185 (2005).
60. C. L. Zavaleta, B. R. Smith, I. Walton, W. Doering, G. Davis, B. Shojaei, M. J. Natan, and S. S. Gambhir, "Multiplexed imaging of surface enhanced Raman scattering nanotags in living mice using noninvasive Raman spectroscopy," Proceedings of the National Academy of Sciences **106**, 13511-13516 (2009).
61. L. Shuo, G. Jean, J. O. Nyagilo, and D. P. Dave, "Eigenspectra, a robust regression method for multiplexed Raman spectra analysis," in *Bioinformatics and Biomedicine (BIBM), 2010 IEEE International Conference on*(2010), pp. 525-530.
62. M. C. Haffner, J. Laimer, A. Chaux, G. Schafer, P. Obrist, A. Brunner, I. E. Kronberger, K. Laimer, B. Gurel, J.-B. Koller, C. Seifarth, B. Zelger, H. Klocker, M. Rasse, W. Doppler, and N. H. Bander, "High expression of prostate-specific membrane antigen in the tumor-associated neo-vasculature is associated with worse prognosis in squamous cell carcinoma of the oral cavity," Mod Pathol **25**, 1079-1085 (2012).
63. A. R. F. R E Carter, and J T Coyle, "Prostate-specific membrane antigen is a hydrolase with substrate and pharmacologic characteristics of a neuropeptidase.," Proc Natl Acad Sci U S A **93**, 749–753 (1996).
64. H. Liu, A. K. Rajasekaran, P. Moy, Y. Xia, S. Kim, V. Navarro, R. Rahmati, and N. H. Bander, "Constitutive and Antibody-induced Internalization of Prostate-specific Membrane Antigen," Cancer Research **58**, 4055-4060 (1998).
65. N. Schülke, O. A. Varlamova, G. P. Donovan, D. Ma, J. P. Gardner, D. M. Morrissey, R. R. Arrigale, C. Zhan, A. J. Chodera, K. G. Surowitz, P. J. Maddon, W. D. W. Heston, and W. C. Olson, "The homodimer of prostate-specific membrane antigen is a functional target for cancer therapy," Proceedings of the National Academy of Sciences **100**, 12590-12595 (2003).
66. P. Wolf, K. Alt, D. Wetterauer, P. Buhler, D. Gierschner, A. Katzenwadel, U. Wetterauer, and U. Elsasser-Beile, "Preclinical evaluation of a recombinant anti-prostate specific membrane antigen single-chain immunotoxin against prostate cancer," J Immunother **33**, 262-271 (2010).
67. X. Gao, Y. Cui, R. M. Levenson, L. W. K. Chung, and S. Nie, "In vivo cancer targeting and imaging with semiconductor quantum dots," Nat Biotech **22**, 969-976 (2004).
68. Robert M. Taylor, Virginia Severns, David C. Brown, Marco Bisoffi, and a. L. O. Sillerud, "Prostate CancerTargeting Motifs: Expression of anb3, Neurotensin Receptor1,Prostate Specific Membrane Antigen, and Prostate Stem Cell Antigen in Human Prostate Cancer Cell Lines and Xenografts," Wiley Online Library (2011).
69. M. K. Nicholas, R. V. Lukas, N. F. Jafri, L. Faoro, and R. Salgia, "Epidermal Growth Factor Receptor-Mediated Signal Transduction in the Development and Therapy of Gliomas," Clinical Cancer Research **12**, 7261-7270 (2006).
70. A. B. Heimberger, R. Hlatky, D. Suki, D. Yang, J. Weinberg, M. Gilbert, R. Sawaya, and K. Aldape, "Prognostic Effect of Epidermal Growth Factor Receptor and EGFRvIII in Glioblastoma Multiforme Patients," Clinical Cancer Research **11**, 1462-1466 (2005).

71. A. Lal, C. A. Glazer, H. M. Martinson, H. S. Friedman, G. E. Archer, J. H. Sampson, and G. J. Riggins, "Mutant Epidermal Growth Factor Receptor Up-Regulates Molecular Effectors of Tumor Invasion," Cancer Research **62**, 3335-3339 (2002).
72. N. Shinojima, K. Tada, S. Shiraishi, T. Kamiryo, M. Kochi, H. Nakamura, K. Makino, H. Saya, H. Hirano, J.-i. Kuratsu, K. Oka, Y. Ishimaru, and Y. Ushio, "Prognostic Value of Epidermal Growth Factor Receptor in Patients with Glioblastoma Multiforme," Cancer Research **63**, 6962-6970 (2003).
73. J. Berlanga-Acosta, Jorge Gavilondo-Cowley, D. C. d. Barco-Herrera, J. Martin-Machado, and G. Cuillen-Nieto, "Epidermal Growth Factor (EGF) and Platelet-Derived Growth Factor (PDGF) as Tissue Healing Agents: Clarifying Concerns about their Possible Role in Malignant Transformation and Tumor Progression," J Carcinogene Mutagene **2**, 14 (2011).
74. R. S. Herbst, and D. M. Shin, "Monoclonal antibodies to target epidermal growth factor receptor–positive tumors," Cancer **94**, 1593-1611 (2002).
75. A. Louie, "Multimodality Imaging Probes: Design and Challenges," Chemical Reviews **110**, 3146-3195 (2010).
76. Y. Huang, F. Yu, Y.-S. Park, J. Wang, M.-C. Shin, H. S. Chung, and V. C. Yang, "Co-administration of protein drugs with gold nanoparticles to enable percutaneous delivery," Biomaterials **31**, 9086-9091 (2005).
77. J. Birchall, "Interview: Mini Focus: Interview with Dr James Birchall," Therapeutic Delivery **3**, 311-313 (2012).
78. G. Cevc, and U. Vierl, "Nanotechnology and the transdermal route: A state of the art review and critical appraisal," Journal of Controlled Release **141**, 277-299 (2010).
79. S. Bhaskar, F. Tian, T. Stoeger, W. Kreyling, J. de la Fuente, V. Grazu, P. Borm, G. Estrada, V. Ntziachristos, and D. Razansky, "Multifunctional Nanocarriers for diagnostics, drug delivery and targeted treatment across blood-brain barrier: perspectives on tracking and neuroimaging," Particle and Fibre Toxicology **7**, 3 (2010).
80. M. S. Bhojani, M. Van Dort, A. Rehemtulla, and B. D. Ross, "Targeted Imaging and Therapy of Brain Cancer Using Theranostic Nanoparticles," Molecular Pharmaceutics **7**, 1921-1929 (2010).
81. X. He, J. Gao, S. S. Gambhir, and Z. Cheng, "Near-infrared fluorescent nanoprobes for cancer molecular imaging: status and challenges," Trends in Molecular Medicine **16**, 574-583 (2010).
82. C. G. Hadjipanayis, M. J. Bonder, S. Balakrishnan, X. Wang, H. Mao, and G. C. Hadjipanayis, "Metallic Iron Nanoparticles for MRI Contrast Enhancement and Local Hyperthermia," Small **4**, 1925-1929 (2008).
83. M. G. Harisinghani, J. Barentsz, P. F. Hahn, W. M. Deserno, S. Tabatabaei, C. H. van de Kaa, J. de la Rosette, and R. Weissleder, "Noninvasive Detection of Clinically Occult Lymph-Node Metastases in Prostate Cancer," New England Journal of Medicine **348**, 2491-2499 (2003).
84. Y.-M. Huh, Y.-w. Jun, H.-T. Song, S. Kim, J.-s. Choi, J.-H. Lee, S. Yoon, K.-S. Kim, J.-S. Shin, J.-S. Suh, and J. Cheon, "In Vivo Magnetic Resonance Detection of

Cancer by Using Multifunctional Magnetic Nanocrystals," Journal of the American Chemical Society **127**, 12387-12391 (2005).
85. M. Lewin, N. Carlesso, C.-H. Tung, X.-W. Tang, D. Cory, D. T. Scadden, and R. Weissleder, "Tat peptide-derivatized magnetic nanoparticles allow in vivo tracking and recovery of progenitor cells," Nat Biotech **18**, 410-414 (2000).
86. W. Cai, G. Niu, and X. Chen, "Imaging of Integrins as Biomarkers for Tumor Angiogenesis," Current Pharmaceutical Design **14**, 2943-2973 (2008).
87. J. F. Hainfeld, D. N. Slatkin, T. M. Focella, and H. M. Smilowitz, "Gold nanoparticles: a new X-ray contrast agent," British Journal of Radiology **79**, 248-253 (2006).
88. J.-H. Kim, J.-S. Kim, H. Choi, S.-M. Lee, B.-H. Jun, K.-N. Yu, E. Kuk, Y.-K. Kim, D. H. Jeong, M.-H. Cho, and Y.-S. Lee, "Nanoparticle Probes with Surface Enhanced Raman Spectroscopic Tags for Cellular Cancer Targeting," Analytical Chemistry **78**, 6967-6973 (2006).
89. R. Popovtzer, A. Agrawal, N. A. Kotov, A. Popovtzer, J. Balter, T. E. Carey, and R. Kopelman, "Targeted Gold Nanoparticles Enable Molecular CT Imaging of Cancer," Nano Letters **8**, 4593-4596 (2008).
90. K. K. Maiti, U. S. Dinish, A. Samanta, M. Vendrell, K.-S. Soh, S.-J. Park, M. Olivo, and Y.-T. Chang, "Multiplex targeted in vivo cancer detection using sensitive near-infrared SERS nanotags," Nano Today **7**, 85-93 (2012).
91. J. Rao, A. Dragulescu-Andrasi, and H. Yao, "Fluorescence imaging in vivo: recent advances," Current Opinion in Biotechnology **18**, 17-25 (2007).
92. M. Shilo, T. Reuveni, M. Motiei, and R. Popovtzer, "Nanoparticles as computed tomography contrast agents: current status and future perspectives," Nanomedicine **7**, 257-269 (2012).
93. G. H. Woehrle, L. O. Brown, and J. E. Hutchison, "Thiol-Functionalized, 1.5-nm Gold Nanoparticles through Ligand Exchange Reactions: Scope and Mechanism of Ligand Exchange," Journal of the American Chemical Society **127**, 2172-2183 (2005).
94. H. Chen, M. M. Rogalski, and J. N. Anker, "Advances in functional X-ray imaging techniques and contrast agents," Physical Chemistry Chemical Physics **14**, 13469-13486 (2012).
95. M. M. Reuveni T, Romman Z, Popovtzer A, Popovtzer R "Targeted gold nanoparticles enable molecular CT imaging of cancer: an in vivo study " International journal of nanomedicine **6**, 2859-2864 (2011).
96. C. Xu, G. A. Tung, and S. Sun, "Size and Concentration Effect of Gold Nanoparticles on X-ray Attenuation As Measured on Computed Tomography," Chemistry of Materials **20**, 4167-4169 (2008).
97. P. Nativo, I. A. Prior, and M. Brust, "Uptake and Intracellular Fate of Surface-Modified Gold Nanoparticles," ACS nano **2**, 1639-1644 (2008).
98. J. Fang, H. Nakamura, and H. Maeda, "The EPR effect: Unique features of tumor blood vessels for drug delivery, factors involved, and limitations and augmentation of the effect," Advanced Drug Delivery Reviews **63**, 136-151 (2011).

99. A. K. Iyer, G. Khaled, J. Fang, and H. Maeda, "Exploiting the enhanced permeability and retention effect for tumor targeting," Drug Discovery Today **11**, 812-818 (2006).
100. F. L. Filon, M. Boeniger, G. Maina, G. Adami, P. Spinelli, and A. Damian, "Skin Absorption of Inorganic Lead (PbO) and the Effect of Skin Cleansers," Journal of Occupational and Environmental Medicine **48**, 692-699 610.1097/1001.jom.0000214474.0000261563.0000214471c (2006).
101. N. V. Gopee, D. W. Roberts, P. Webb, C. R. Cozart, P. H. Siitonen, J. R. Latendresse, A. R. Warbitton, W. W. Yu, V. L. Colvin, N. J. Walker, and P. C. Howard, "Quantitative Determination of Skin Penetration of PEG-Coated CdSe Quantum Dots in Dermabraded but not Intact SKH-1 Hairless Mouse Skin," Toxicological Sciences **111**, 37-48 (2009).
102. T. G. M. Smijs, and J. A. Bouwstra, "Focus on Skin as a Possible Port of Entry for Solid Nanoparticles and the Toxicological Impact," Journal of Biomedical Nanotechnology **6**, 469-484 (2010).
103. G. Sonavane, K. Tomoda, A. Sano, H. Ohshima, H. Terada, and K. Makino, "In vitro permeation of gold nanoparticles through rat skin and rat intestine: Effect of particle size," Colloids and Surfaces B: Biointerfaces **65**, 1-10 (2008).
104. F. Alimirah, J. Chen, Z. Basrawala, H. Xin, and D. Choubey, "DU-145 and PC-3 human prostate cancer cell lines express androgen receptor: Implications for the androgen receptor functions and regulation," FEBS Letters **580**, 2294-2300 (2006).

Biographical Information

James Otieno Nyagilo was born in January 24th, 1980 at Uasin Gishu in Kenya. He is the son of Charles Nyagilo an Electrical Engineer and Dorcas Nyagilo a Psychologist and Primary School teacher (English and Science). James interest in science began in primary school inspired by his parents. He received a bachelor of science in Physics in 2005 from the Jomo Kenyatta University of Agriculture and Technology, Juja, Kenya. Upon completion of his undergraduate studies, James had a brief stint at the National Radiation Protection Laboratories in Kenya. The experience convinced him to pursue graduate training in biomedical engineering. Such an opportunity arose from the University of Texas at Arlington.